Characterization of Disordered Biomolecular Systems with Scattering Techniques: A Flexible Protein Complex and Solid-Supported Lipid Bilayers

---

Dennis J. Michalak

Thesis Committee
Mathias Lösche
Frank Heinrich
Carol L. Williams
David P. Hoogerheide

Submitted in partial fulfillment of the
requirements for the degree of
Doctor of Philosophy
at
Carnegie Mellon University
Department of Physics
Pittsburgh, Pennsylvania

December 2021

Abstract

Disorder serves a functional role in cellular membranes and flexible protein domains. An in-plane fluid mixture of phospholipids, carbohydrates, membrane proteins, and more constitute the plasma membrane. Disordered regions of proteins leverage a wide conformational space to facilitate complexation, signaling, and regulatory interactions. Experimental approaches which quantify structural information of these systems ideally facilitate biomimetic sample environments. Scattering techniques provide a minimally restrictive platform for characterizing macromolecular systems including lipid bilayers and intrinsically disordered proteins. This thesis contains studies of these systems which utilize X-ray and neutron scattering methods complemented by computational and theoretical structural predictions.

The small GTPase KRas acts as a binary switch at the plasma membrane, anchored by a flexible domain, participating in signaling pathways vital for cellular survival and proliferation. Its localization to the plasma membrane is dependent on chaperone proteins, such as SmgGDS, which bind and traffic it through the cytosol. Two isoforms of SmgGDS regulate the prenylation and localization of small GTPases: SmgGDS-607 binds unprenylated small GTPases while SmgGDS-558 associates and houses the lipid anchor of prenylated small GTPases in a hydrophobic pocket. Structural and thermodynamic details of KRas complexation with SmgGDS are critical for understanding Ras biology and for identifying potential targets for chemical inhibition of oncogenic KRas signaling. We show that SmgGDS-558 readily solubilizes KRas bound to anionic membranes with a binding affinity larger than that of KRas associating with the membrane. Using a combination of solution scattering and molecular dynamics simulations, a configurational ensemble of a flexible SmgGDS-558/KRas complex was determined in which specific interactions were found to be limited to the C-terminal end of the hypervariable region. Informed by mutational studies which identify a collection of SmgGDS residues as important for binding KRas, we observe a set of anionic residues near the hydrophobic pocket of SmgGDS-558 directly associating KRas within the determined flexible ensemble.

Structural studies of membrane proteins frequently utilize model membranes supported by solid-state surfaces. Understanding fundamental interactions between lipid membranes and such surfaces is crucial, not only for the development of novel architectures for characterizing membrane proteins, but also for conceptualization of biosensors which detect and transduce stimuli at the bilayer-substrate interface. We have developed an experimental and theoretical framework for tuning the association of zwitterionic lipid bilayers with solid substrates. In this effort, we performed systematic neutron

reflectometry studies which identify the formation mechanism of a novel, facile technique for synthesizing solid-supported membranes. We observed headgroups of a lipid monolayer associating with the surface in hydrophobic solvent, which form a template for subsequent self-assembly of the lipid bilayer on exchange with aqueous solvent. We fabricated complete membranes at surface chemistries unamenable to conventional bilayer formation methods such as vesicle fusion. A mean-field approach to modeling the free energy of bilayer-substrate interactions as a superposition of electrostatic, van der Waals, steric, and short-range hydration components was assessed with the modeled interfacial structure derived from neutron reflectometry data. The resulting free energy model of this experimental system quantitatively predicts the dependence of the lipid membrane separation distance on the substrate surface charge. By altering substrate surface chemistry and aqueous buffer composition, the range and magnitude of electrostatic forces can be finely tuned relative to the van der Waals, confinement, and hydration forces which are invariant to these electrochemical properties. In this way, the morphology of a "floating" bilayer was finely controlled at the nanoscale-level out to a separation distance of 40 Å where out-of-plane bilayer undulations are weakly suppressed.

Acknowledgments

I would first like to thank my advisor and mentor Dr. Mathias Lösche for the opportunities, support, and guidance he has provided me throughout the years. I also thank Dr. Frank Heinrich for his mentorship, generosity, and for what I came to learn was his sense of humor. I thank Dr. Carol Williams for her encouraging words and infectious enthusiasm. I would like to thank Dr. David Hoogerheide for the opportunity to work on such a fascinating project and for the guidance along the way.

I thank my collaborators who each provided invaluable expertise and support throughout our work together. Thank you to Ellen Lorimer and Bethany Unger for your work on the SmgGDS project. I am also very grateful to have worked with and learned so much from Dr. Alex Grishaev.

The friendship I found in my cohort, specifically Ruairí Brett, Greg Houchins, Chris Kervick, and Brad Parks, was crucial throughout my graduate career but especially so in those first few years. I would like to thank fellow group members Rebecca Eells and Bradley Treece for showing me the ins and outs in the lab and for our conversations in and out of the office. Thank you to Brian Josey for your kindness and for helping me socialize with the friendly folks at the NCNR. I would like to thank Amy Stetten and Krista Freeman for their friendship along the way. I thank all of my teammates in *Manfred United* over the years who helped me learn how much fun soccer can be, win or lose (mostly lose).

Thank you to my family and friends who have given me so much and without whom I would not be who I am today. Charly, thank you so much for your love, silliness, and for helping me stay sane during this journey.

List of Publications

D. J. Michalak, M. Lösche, D. P. Hoogerheide (2021) "Charge Effects Provide Ångström-Level Control of Lipid Bilayer Morphology on Titanium Dioxide Surfaces" *Langmuir* 37(13):3970-3981.

D. J. Michalak, E. Lorimer, B. Unger, A. Grishaev, C. L. Williams, F. Heinrich, M. Lösche. "Fully Processed KRas Binds SmgGDS-558 Via the Hypervariable Region" *Manuscript in preparation.*

Contents

List of Tables

List of Figures

Chapter 1

Introduction

The plasma membrane is a dynamic, fluid structure that defines the boundary of cells while simultaneously mediating molecular transport and intercellular signaling [14]. Additionally, many internal organelles of eukaryotic cells are either composed of or compartmentalized by membranes [15,16]. Native membranes are nearly two-dimensional sheets (approximately 5 nm thick) of two lipid leaflets forming a phospholipid bilayer. Hundreds of lipid species are heterogeneously distributed in cellular lipid membranes and are dynamically arranged due to in-plane fluidity [17]. This diverse environment also includes a plentiful assortment of carbohydrates and proteins [15]. Encoded by more than 30% of mammalian genes, membrane proteins participate in a vast array of processes such as intracellular trafficking [18], signal transduction and processing [19], and cell proliferation [20]. The native state of cellular lipid membranes resembles that of a two-dimensional heterogeneous mixture (an illustration of the binding of insulin to membrane-bound receptors is shown in 1.1), a result of the great variety of biomolecular structures embedded within it that diffuse laterally throughout its planar geometry.

Within this dynamic space, a large fraction of membrane proteins exist which contain regions with intrinsic disorder. These regions have physiological structure that exists as a configurational ensemble. At least 35% of all proteins contain intrinsically disordered domains and are functionally important for many cellular processes [21,22]. These regions can serve as a flexible linker between folded protein domains [23], regulate the rate of ionic transport across membranes [24], and facilitate the anchoring of membrane proteins to the lipid bilayer [25].

Small GTPases are a class of approximately 20-30 kDa proteins that actively mediate signaling at cellular membranes in critical pathways such as cell migration, survival, and differentiation [26]. Composed of a folded GTPase domain and an intrinsically disordered hypervariable region, newly synthesized small GTPases are modified at multiple locations in cells before localizing at the plasma membrane [27,28]. KRas is a prominent example of a small GTPase that has been extensively studied both for its importance in

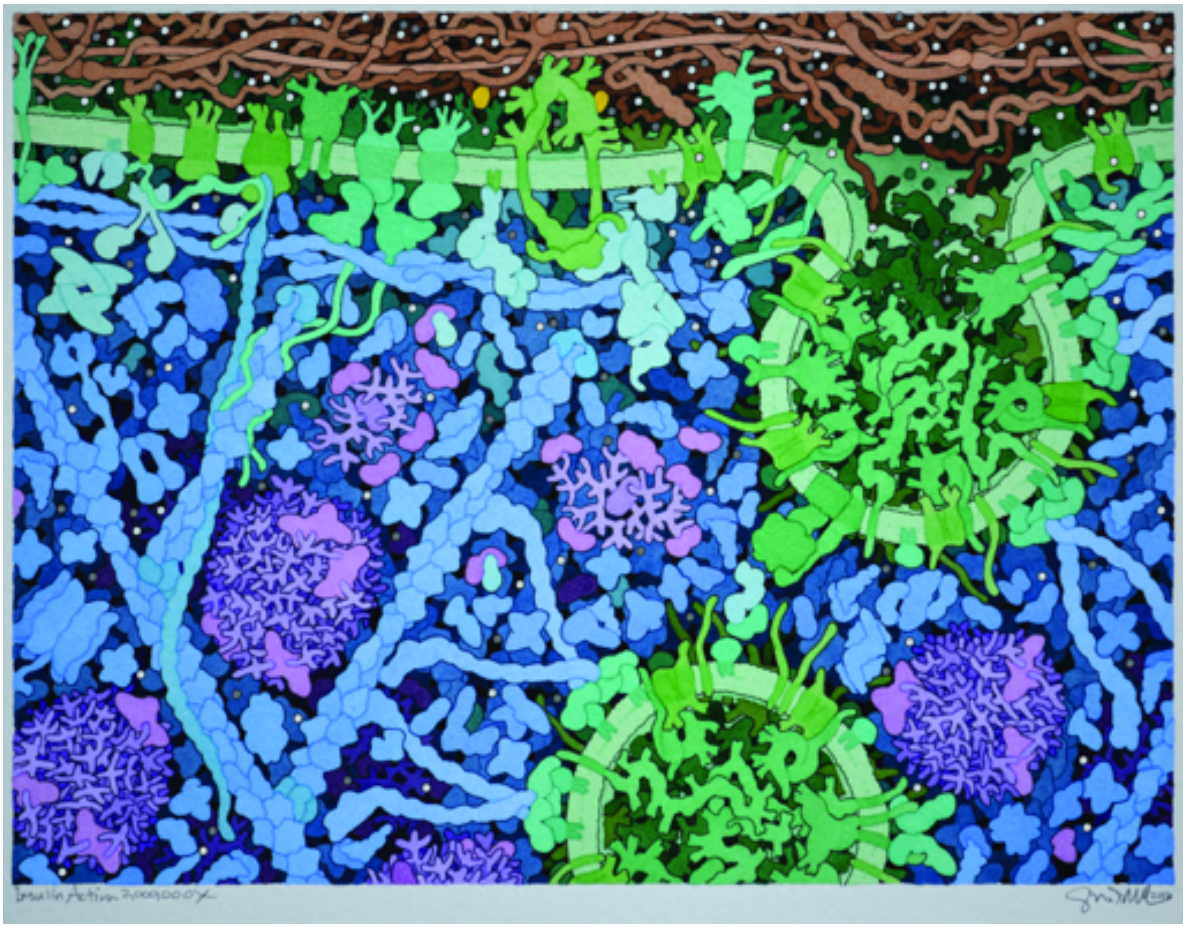

Figure 1.1: Insulin binding to membrane receptor proteins. In an illustration by David S. Goodsell, RCSB Protein Data Bank [2], insulin receptor proteins bind insulin (top, yellow) and activate a signal cascade wherein enzymes build glucose-storing glycogen (purple). Lipid bilayers and membrane proteins (green) are dynamically arranged in natural contexts. The plasma membrane is deformed (right) during endocytosis to import extracellular material into the cytosol encapsulated in endocytic vacuoles (bottom, green) [3].

cellular function and for its substantive role in cancer [29–31]. Substantial effort has been put into structural characterization of KRas both at the membrane and in complex with cytosolic chaperones such as PDEδ [32,33]. Additionally, studies of KRas at model membranes describe how the flexible hypervariable region could serve functional roles in binding to effector proteins [34].

This relationship between molecular structure and biological function motivates a large part of the biophysical study of proteins and lipid membranes. Many techniques have been utilized for describing structural aspects of biological systems including X-ray diffraction from crystallized protein, nuclear magnetic resonance (NMR), electron microscopy, and X-ray neutron scattering. Each have differing constraints on the sample environment for study and directly impact their ability to model physiological contexts. X-ray crystallography is capable of atomic resolution (on the order of 1-2 Å) structural determination of biological macromolecules [35,36]. The diffraction pattern is analyzed to describe the identity and positions of atoms constituting the crystallized sample via electron density mapping [37]. Diffraction measurements require highly ordered samples which necessitate placing the macromolecule in an environment wholly alien in comparison to its native context. NMR is capable of describing high resolution, 3D structures of proteins with disordered regions including those solubilized in lipid nanodiscs [38]. A typical experiment characterizing protein-ligand interactions monitors the chemical shift of labeled atomic nuclei in the protein while the unlabeled ligand is titrated. Upon binding, a shift in the resonant frequency of labeled nuclei in response to a magnetic field is observed. High concentrations are required to obtain sufficient signal which is proportional to the number of binding events the measurement period. As a result, weak binding interactions are generally preferred as the rates of association and dissociation rates facilitate higher counts of binding events, resulting in higher signal-to-noise levels [39]. Developments in cryo-electron microscopy (cryo-EM) have yielded increasingly high resolution descriptions of single-particle samples of large macromolecules typically on the order of megaDaltons (MDa) [40]. The sample environment requires the macromolecular structure to be fixed, typically achieved through vitrification by plunge freezing, and provides information on the static conformations adopted by macromolecular constructs [41]. X-ray and neutron scattering require minimal constraints on sample preparations allowing near-physiological sample environments and are capable of providing sub-nm resolution structural information [42,43]. Small-angle X-ray scattering (SAXS) is a low-resolution technique and has been used to characterize a wide range of biological samples with and without intrinsic disorder [44,45]. This versatility is one of the key strengths of scattering techniques. Neutron reflectometry (NR) is a characterization technique for planar sample geometries (e.g. supported lipid membranes) and is sensitive to the molecular structures at interfaces. By averaging in-plane structure, one-dimensional distributions of sub-molecular components along the

surface normal are obtained [46,47]. The use of NR for describing peripheral membrane proteins at model membranes is well documented and has been used to describe the structural dynamics of disordered systems [34,48–51]. Background information of these techniques are discussed in more detail in Chapter 2.

This work focuses on scattering studies of biological systems exhibiting intrinsic disorder. In chapter 3, solution SAXS was used to characterize samples of the chaperone protein SmgGDS and fully processed KRas. Aided by Monte Carlo and molecular dynamics simulations, an ensemble of a SmgGDS-558 and KRas complex was determined which describes the scattering data. Binding interactions between SmgGDS-558 and KRas were defined by the C-terminal polybasic region and lipidation of KRas associating SmgGDS-558 at the hydrophobic pocket. Thermodynamic information of SmgGDS and KRas binding from surface plasmon resonance studies was used in comparisons to the well-characterized complex of PDEδ and KRas to discuss the functional role of SmgGDS in membrane localization of KRas. Additional NR studies of immobilized SmgGDS at supported lipid bilayers are discussed.

Described in chapter 4, zwitterionic lipid bilayers, with in-plane fluid disorder, were fabricated on solid-state surfaces using a novel method previously described in [52] and were characterized with NR. The formation mechanism of complete DOPC bilayers by the solvent-assisted lipid bilayer method is described in which incomplete lipid monolayers make a template for bilayer assembly during solvent exchange. Composition space modeling of NR data was used to characterize bilayer-substrate separation distances and root-mean-square bilayer corrugations at titanium dioxide (TiO_2), silicon dioxide (SiO_2), bare gold, and β-mercaptoethanol functionalized gold surface chemistries. Changes in bilayer morphology at TiO_2 and SiO_2 were quantified in response to systematic variations in ionic strength and pH of the buffering aqueous solvent. Underlying assumptions and limitations in the quantitative free energy model used to describe the observed phenomena [1] are discussed.

Chapter 2

Experimental Methods

Studies with biomimetic membranes were performed using the sparsely-tether bilayer lipid membrane (stBLM) system. stBLMs are nearly defect-free planar bilayers and were used in characterizing protein binding at the membrane. Their formation and properties are discussed followed by descriptions of characterization techniques used for stBLM systems: electrochemical impedance spectroscopy (EIS) to measure the quality of formed stBLMs, surface plasmon resonance (SPR) to quantify membrane binding of protein, and neutron reflectometry (NR) to characterize the structure of bilayers and membrane-bound protein. In addition to lipid bilayer systems, significant work was performed with protein samples in solution. The final section discusses small-angle X-ray scattering (SAXS), a low-resolution structural characterization technique, and its use to characterize protein structures and interactions in solution.

2.1 stBLM

2.1.1 Introduction

The stBLM (Figure 2.1) is a biomimetic membrane wherein a phospholipid planar bilayer is supported by a submembrane layer of synthetic lipids and spacer molecules on an atomically flat gold substrate [4, 53–55]. The submembrane self-assembled monolayer (SAM) is composed of a mixture of synthetic tether HC-18 (see Materials section for details) and β-mercaptoethanol which passivates the remaining exposed Au surface. Both components covalently bond gold through terminal thiol or thiol acetate groups. The tether molecule contains a polyethylene chain which terminates with two unsaturated C-18 hydrocarbon tails which serve as a scaffold for bilayer formation. Using vesicle fusion, the phospholipid bilayer is fabricated with negligible defects atop the tether layer [4]. The submembrane layer remains hydrated through use of spacer molecules. Hydration in the submembrane space (approximately 10-15 Å thick) and unsaturated

hydrocarbon tails of the tether is sufficient to maintain comparable in-plane fluidity between inner and outer leaflets of the supported bilayer [4]. stBLMs are long-term stable and are amenable to a variety of lipid compositions. Their planar geometry, low surface roughness, and facile preparation make them particularly suited for NR studies.

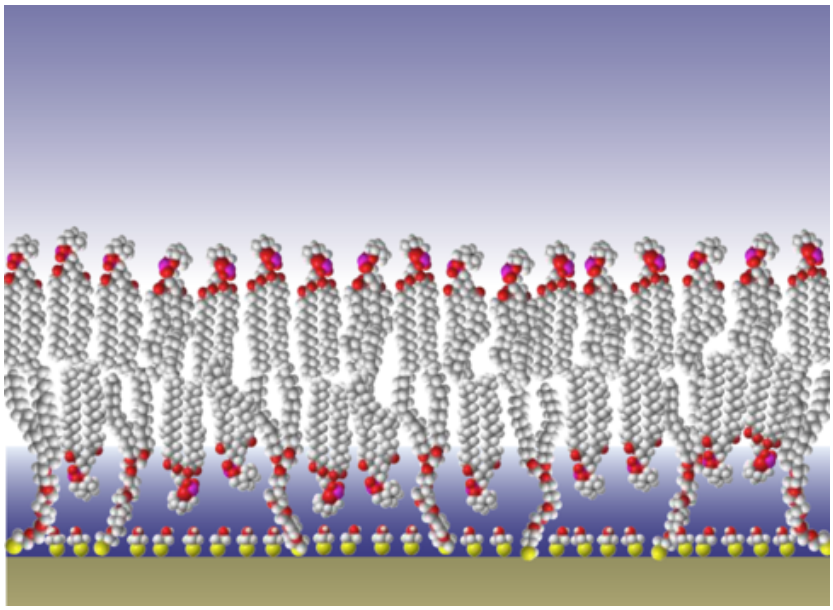

Figure 2.1: Sparsely-tethered bilayer lipid membrane. The lipid bilayer constituting the stBLM retains in-plane fluidity within the inner and outer leaflets [4]. The SAM is formed by co-adsorption of tether molecules to support the lipid bilayer and β-mercaptoethanol which functionalizes and passivates the remaining exposed surface. stBLMs are conducive to studying a variety of membrane binding proteins including transmembrane proteins as the hydrated submembrane space inhibits interactions between a transmembrane protein domain and the substrate surface.

2.1.2 Formation

Self-assembled monolayer

Glass microscopy slides (Thermo Fisher Scientific, Waltham, MA) were cleaned with a Hellmanex solution (Hellma Analytics, Müllheim, Germany) at 5 vol% and rinsed with ultrapure water followed by pure ethanol. A nitrogen gas stream was used to dry slides before placing them a sulfuric acid bath with dissolved Nochromix (Godax Laboratories, Cabin John, MD) for 15 minutes. Glass slides were then rinsed with copious amounts of ultrapure water (EMD Millipore, Billerica, MA) and pure ethanol before drying by a nitrogen gas stream. In SPR and EIS experiments, chromium and gold layers were sputtered (ATC Orion; AJA International, Scituate, MA) at approximately 20 Å and

450 Å thicknesses respectively. Gold film thicknesses were approximately 150 Å for NR studies. Coated slides were incubated in an ethanol solution of 0.2 mM HC-18 and βMe in a 3:7 molar ratio overnight. Immediately prior to bilayer formation, the incubated coated slides were rinsed with pure ethanol, dried by a nitrogen gas stream, and loaded into the sample environment.

Supported lipid bilayer

Stock chloroform solutions of lipids were mixed according to the desired lipid composition. Prepared solutions were placed under vacuum overnight to evaporate organic solvent. The samples were hydrated to yield a lipid concentration of 5.0 mg/mL in an aqueous buffer containing 2 M NaCl, 20 mM $NaPO_4$ at pH 7.4. Sonication was performed for vesicle formation for 1 hour followed by visual inspection for sample clarity. The vesicle solution was loaded into sample cells containing a prepared self-assembled monolayer and incubated for 1 hour. The samples were then flushed with aqueous buffer (50 mM NaCl, 10 mM $NaPO_4$ at pH 7.4) to induce osmotic shock of vesicles. SPR was used in parallel with the bilayer formation process to monitor response changes due to buffer exchange. Rinsing of the sample was performed to remove overlayers and until the response returned to its previous level indicating complete exchange of buffer. EIS measurements were taken to quantify bilayer capacitance and resistance due to defects to ascertain bilayer quality.

2.1.3 Materials

Lipids used in this work were purchased from Avanti Polar Lipids, Inc. (Alabaster, AL). These include 1,2-dioleoyl-sn-glyero-3-phosphocholine (DOPC), 1-palmitoyl-2-oleoyl-sn-glycero-3-phosphocholine (POPC), 1-palmitoyl-2-oleoyl-sn-glycero-3-phospho-L-serine (POPS), and 1,2-dioleoyl-sn-glycero-3-[(N-(5-amino-1-carboxypentyl) iminodiacetic acid) succinyl] (nickel salt) (DGS-NTA(Ni)). The synthetic tether Z20-(Z-octadec-9-enyloxy)-3,6,9,12,15,18,22-heptaoxatetracont-31-ene-1-thio-acetate (HC-18) was synthesized as described in previous work [55] by David Vanderah (Institute for Bioscience and Biotechnology Research; IBBR). β-mercaptoethanol (βMe) was purchased from Sigma-Aldrich (St. Louis, Mo). Gold (99.99% purity) and chromium sputtering wafers were purchased from AJA International (Scituate, MA).

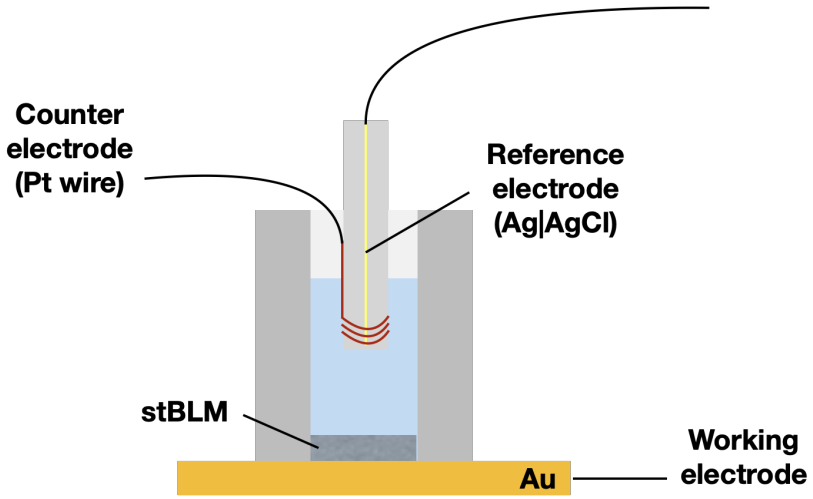

Figure 2.2: Three-electrode configuration for stBLM system. An AC signal is applied across the stBLM where the Au film and (Ag—AgCl) electrode serve as the working and reference electrodes, respectively. The Pt wire counter electrode completes a circuit through the cell with the working electrode. The reference electrode is situated 2 to 3 mm from the working electrode. Within the cell, 0.33 cm^2 of the working electrode surface is exposed.

2.2 Electrochemical Impedance Spectroscopy

2.2.1 Introduction

Electrochemical impedance spectroscopy (EIS) is a characterization technique which quantifies electrochemical properties of a system. By applying an AC signal across an stBLM sample, the amplitude and phase of the current response can be recorded over a range of frequencies to measure the resistance and capacitance of the lipid bilayer. EIS spectrograms were taken of SAMs and stBLMs (described in the previous section) in preparation for SPR experiments. The electrochemical response of these systems is indicative of completeness and thickness of bilayer formation. A three-electrode configuration (see Figure 2.2) was utilized consisting of working electrode (gold film surface), reference electrode (saturated silver-silver chloride microelectrode), and counter electrode (0.25 diameter PT wire). Typically, EIS spectrograms were collected before and after protein binding experiments.

2.2.2 Theory

In general, electrochemical cells exhibit non-linear response to frequency dependent applied voltages. By restricting voltages to small values, the response becomes approximately linear. Under this condition, when a frequency dependent voltage is applied to a

circuit, the current response is delayed by a frequency dependent phase shift $\phi(\omega)$. This phase shift can be described in the context of the complex impedance of the circuit, $\hat{Z}(\omega)$, which is defined by the equation

$$\hat{V}(\omega) = \hat{I}(\omega)\hat{Z}(\omega) \tag{2.1}$$

with $\hat{V}$ and $\hat{I}$ defined as the associated voltage and current respectively. These quantities can be written using Euler notation as

$$\hat{V}(\omega) = V_0 e^{i\omega t} \tag{2.2}$$

$$\hat{I}(\omega) = I_0 e^{i(\omega t - \phi(\omega))} \tag{2.3}$$

$$\hat{Z}(\omega) = Z_0 e^{i\phi(\omega)} \tag{2.4}$$

where $Z_0 = V_0/I_0$. Any circuit element can be described in terms of the complex impedance. For example, an ideal resistor has an impedance which is entirely real and takes on the value of resistance R.

$$\hat{Z}(\omega) = \mathrm{Re}(\hat{Z}(\omega)) = R$$

An ideal capacitor has an impedance of

$$\hat{Z}(\omega) = \frac{1}{i\omega\hat{C}(\omega)}.$$

It is often convenient to express the complex capacitance explicitly in terms of the real and imaginary terms of $\hat{Z}$.

$$\hat{C}(\omega) = \mathrm{Re}(\hat{C}(\omega)) + i\,\mathrm{Im}(\hat{C}(\omega)) = -\frac{\mathrm{Im}(\hat{Z}(\omega))}{\omega\left|\hat{Z}(\omega)\right|^2} - i\frac{\mathrm{Re}(\hat{Z}(\omega)}{\omega\left|\hat{Z}(\omega)\right|^2} \tag{2.5}$$

In electrochemical studies, it is common to model an electric double layer as an imperfect capacitor or constant phase element (CPE). The impedance of a constant phase element is described in terms of the admittance $\hat{Y}$.[1] The constant phase element

$$\hat{Z}_{\mathrm{CPE}}(\omega) = \frac{1}{\hat{Y}_{\mathrm{CPE}}(i\omega)^\alpha} \tag{2.6}$$

where the parameter α takes values between 0 (ideal resistor) and 1 (ideal capacitor). A more detailed discussion of the CPE and the application of EIS to tethered bilayer

[1] For an ideal circuit element, the admittance is simply the inverse of its impedance.

systems is found in [56].

2.2.3 Instrumentation

An AC voltage was applied to the sample cells at an amplitude of 10 mV (satisfying the linear response condition). The gold substrate served as the working electrode, the reference electrode was a saturated silver-silver chloride (Ag—AgCl—NaCl(aq, sat)) microelectrode (Microelectrode M-401F, Bedford, NC), and wrapped around the reference electrode was a 0.25 mm diameter Pt wire (99.9% purity, Aldritch) serving as the counter electrode. The end of the reference electrode was immersed in the sample cell solution at a distance of 2 to 3 mm from the working electrode surface. A Solartron (Farnborough, UK) 1287A potentiostat maintained a constant potential across the working and reference electrodes by supplying current through the counter electrode. A Solartron 1260 frequency analyzer applied an AC potential to the cell to measure the current response through a range of frequencies (from 1 Hz to 100 kHz), at room temperature, and at 0V bias with respect to the reference electrode. The software Zplot and Zview (Scribner Associates, Southern Pine, NC) were used for data acquisition and modeling respectively. An electrochemical cell was fabricated out of Teflon consisting of two slabs with one containing six holes. A gold-coated microscopy slide is sandwiched between the slabs with a Viton O-ring between the well and gold film. Up to six preparations can be measured which each holding 400 μL with a cross-sectional area of 0.33 Å^2.

2.2.4 Data Analysis

Data was collected and displayed in Cole-Cole plots ($-\operatorname{Im}(\hat{C}(\omega))$ *vs.* $\operatorname{Re}(\hat{C}(\omega))$) for SAMs of tether molecules and β-mercaptoethanol and for stBLMs. Equivalent circuit models were utilized to interpret spectroscopic data in terms of physical parameters of each system. Resistive model elements included R_{sol}, the resistance due to bulk solvent between working and reference electrodes, and R_{def}, resistance due to defects in the SAM and stBLM. SAM models (depicted in Figure 2.3) included an entirely capacitive element, C_{stray}, and a constant phase element CPE_{SAM}. C_{stray} describes the capacitive properties associated with the sample cell and electrode wiring. Figure 2.4 shows the equivalent circuit model used for stBLM systems. Here, a constant phase element CPE_{stBLM} describes the non-ideal capacitance of the support bilayer, R_{def} represents the resistance of membrane defects, and C_{def} is the capacitance of membrane defects. After data acquisition, ZView was used to fit the equivalent circuit model to recorded spectroscopic data with parameters determined from a Levenburg-Marquardt algorithm.

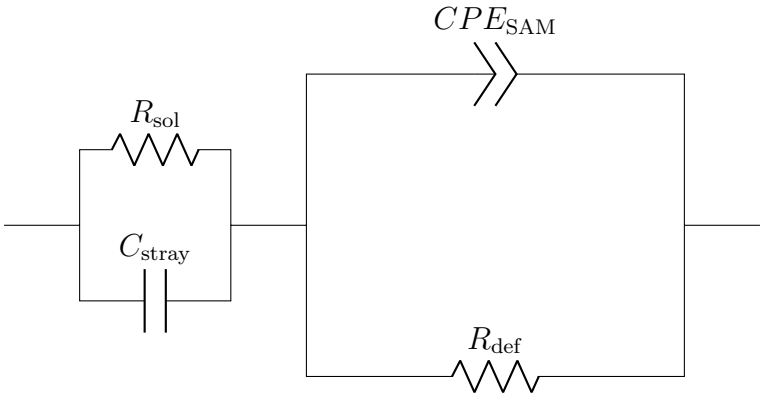

Figure 2.3: Equivalent circuit model of a SAM.

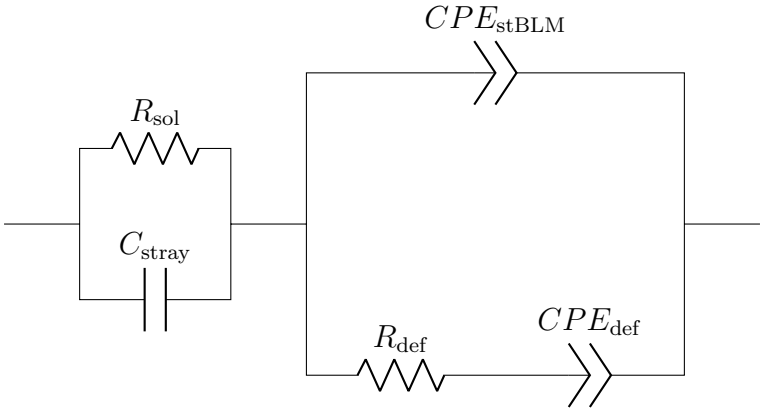

Figure 2.4: Equivalent circuit model of a stBLM.

For typical stBLMs, the Cole-Cole plot provides a convenient means for visual assessment of bilayer quality. The data appears as a semicircle (as shown in Figure 2.5) when the modeled stBLM capacitance is close to the perfect capacitor value, $\alpha = 1.0$. Measurements of prepared stBLMs typically yield values greater than 0.98 indicating nearly ideal capacitive response. The intersection of the semicircle with the x-axis, the real component of the total circuit capacitance, is the capacitance of the modeled SAM or stBLM system. The capacitance of a standard prepared stBLM is less than that of a SAM. A low-frequency tail in the Cole-Cole plot represents the level of defects in the bilayer.

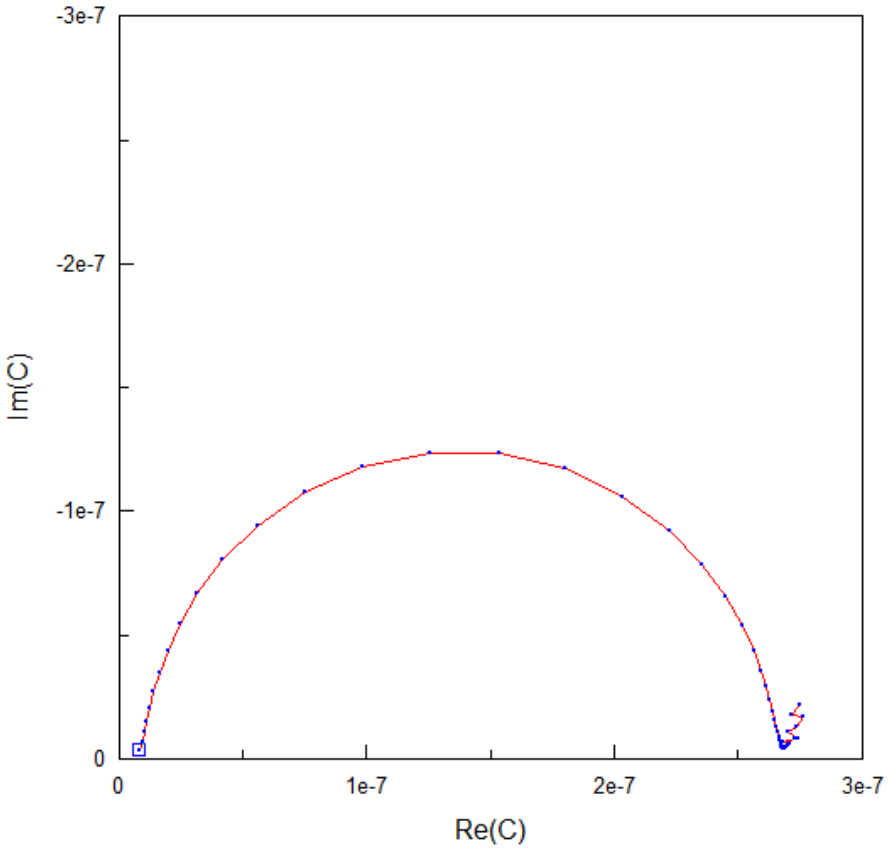

Figure 2.5: Exemplary Cole-Cole plot of a DOPC stBLM with 7:3 βMe:HC18 tether layer. The y-axis shows the imaginary component of total capacitance of the equivalent circuit model and the real component is displayed on the x-axis. EIS data was measured in a frequency range of 1 Hz to 100 kHz. The plot is taken directly from ZPlot where the capacitance in units of Farads. The capacitance of a stBLM is typically reported after normalizing by the area of the sample cell, $A = 0.33$ cm^2. Typical normalized values for fit parameters describing Cole-Cole plots of stBLMs: $R_{\text{sol}} = 200\ \Omega$, $C_{\text{stray}} = 0.015\ \mu$F/cm^2, $R_{\text{def}} = 0.1$ to $1.0\ \text{M}\Omega$, $\text{CPE}_{\text{stBLM}} = 0.8\ \mu$F/cm^2, $\alpha_{\text{stBLM}} = 0.99$, $\text{CPE}_{\text{def}} = 7.8\ \mu$F/cm^2, and $\alpha_{\text{def}} = 0.63$.

2.3 Surface Plasmon Resonance

2.3.1 Introduction

Surface plasmon resonance (SPR) is a surface characterization technique used to study biomolecular interactions near a metal surface. SPR is sensitive to changes in the dielectric constant near a thin metal film and aqueous interface enabling direct detection of ligand-receptor interactions [57]. Typical SPR instrument environments include a

sample chip with a gold film optically coupled to a prism. Polarized light incident on the gold film is reflected and measured with a detector. Surface plasmons are bound electronic waves within a conductive film (e.g. gold) which absorb impinging radiation with matching momentum. At a certain incident angle, the reflected intensity is minimized due to excitation of surface plasmons in the film. This angle is monitored throughout a protein binding experiment to track changes in the resonance angle as a result of protein adsorption events [58]. The detection range is limited to the evanescent field of reflected light at the interface which has a typical penetration depth of hundreds of nanometers. In this work, SPR was used to quantify protein interactions with supported lipid bilayers on gold films.

2.3.2 Theory

A more thorough coverage of the theory underpinning surface plasmons and the technique of surface plasmon resonance is available through a variety of textbooks and published literature (e.g., [57]). Fresnel's equations provide a means of calculating the reflection coefficient describing the reflection of incident p-polarized light at an interface between two media. The reflection coefficient for p-polarized radiation r_p (the ratio of incident and reflected electric fields, E_i and E_r) can be written as

$$r_\mathrm{p} = \frac{E_\mathrm{r}}{E_1} = \frac{\tan(\theta_1 - \theta_2)}{\tan(\theta_1 + \theta_2)} \tag{2.7}$$

where θ_1 and θ_2 are the angles of incidence and transmission, respectively, as measured from the normal of the interface. If the radiation is incident from medium 1 with index of refraction n_1 and is transmitted into medium 2 with index of refraction n_2, the angles can be related through Snell's law. Two special cases occur in Equation 2.7: when $\theta_1 + \theta_2 = \pi/2$, the reflection coefficient vanishes. When $\theta_\mathrm{i} - \theta_\mathrm{t} = \pi/2$, a resonance condition is met where the reflection coefficient approaches infinity or, in other words, there is finite reflected electric field for a very small incident field. If $\theta_1 - \theta_2 = \pi/2$, then Snell's law can be used with $\cos\theta_1 = -\sin\theta_2$ and $k_1/k_2 = \tan\theta_1$ to find

$$\frac{k_1}{k_2} = \frac{-n_2}{n_1} \tag{2.8}$$

where k_1 and k_2 are the wave vectors in media 1 and 2. The wave vector can be broken down into x and z components describing directions parallel to the interface and normal

to the interface, respectively. With $k_{1,x} = k_{2,x} = k_x$ and Equation 2.8, we can write

$$k_1^2 = k_x^2 + k_{1,z}^2 k_1^2 = k_x^2 + k_x^2 \frac{n_1^2}{n_2^2} \tag{2.9}$$

The dispersion relation can be obtained with the dielectric constant (defined as $\epsilon = n^2$).

$$k_x(\omega) = \frac{\omega}{c}\sqrt{\frac{\epsilon_1\epsilon_2}{\epsilon_1+\epsilon_2}} \qquad k_{z,i}(\omega) = \frac{\omega}{c}\sqrt{\frac{\epsilon_i^2}{\epsilon_1+\epsilon_2}} \tag{2.10}$$

When medium 2 is a metal, there are an abundance of free electrons. The corresponding plasma frequency is defined as

$$\omega_\mathrm{p} = \sqrt{4\pi n_\mathrm{e} \mathrm{e}^2/m_\mathrm{e}} \tag{2.11}$$

where n_e is the density of free electrons, e is the charge of an electron, and m_e is the electron mass. With large n_e, the angular frequency of radiation ω will be less than the plasma frequency. ϵ_2 will therefore be negative:

$$\epsilon_2 = 1 - \frac{\omega_\mathrm{p}^2}{\omega^2} \tag{2.12}$$

When the medium's dielectric constant is negative, the incident wave vector in the direction normal to the interface becomes imaginary and the wave vector parallel to the interface remains real. In other words, an electromagnetic wave travels along the interface with exponentially decaying evanescent fields perpendicular to the interface.

For the SPR system used in this work, thin layers in an aqueous environment are deposited onto a gold film. This multilayered systems can be described by an effective dielectric constant ϵ_eff as

$$\epsilon_\mathrm{eff} = \frac{2}{l}\int_0^\infty \epsilon(z) e^{-2z/l}\,\mathrm{d}z \tag{2.13}$$

where l is the decay length of the evanescent field. From Equation 2.13 and the dispersion relations derived from the resonance condition, Equation 2.10, the sensitivity of SPR to the material proximal to the interface is evident. Adsorption events alter the dielectric constant profile normal to the interface $\epsilon(z)$ and, subsequently, the effective dielectric constant of the system. The corresponding change in resonance angle is tracked in real-time to quantify association and disassociation events.

2.3.3 Instrumentation

Measurements were performed with a custom-built instrument (SPR Biosystems, Germantown, MD) in a single-batch set up and held at 25 °C by a temperature controller (Wavelength Electronics LFI-3751, Bozeman, MT). Glass slides were coated with an approximately 45 nm thick gold film and set up in the Kretschmann configuration with an index-matched prism optically coupled with index matching oil, n = 1.52 ± 0.0002 (Cargile, Cedar Grove, NJ). A fan of monochromatic light (λ = 763.8 nm) generated by a superluminescent LED (EXS7510 Exalos AG, Switzerland) impinges the thin film at a range of incident angles. A 2D-CCD detector (Hamamatsu C10990, Hamamatsu City, Japan) records reflected intensities as a function of the angle of incidence with 250 lines of 1024 pixels. All lines are binned into one line of 1024 pixels and the pixel position of the reflectance minimum is tracked as a function of time. The SPARia (SPR Biosystems) software was used to collect and view data. The sample cell is custom-designed consisting of a Teflon cylinder capable of holding a volume of 600 μL solution with a Viton O-ring between the cell and gold substrate leaving an exposed area of approximately 0.33 cm^2. An optical stand was used to hold and adjust the Teflon cell relative to the substrate to ensure contact.

2.3.4 Data Analysis

Throughout an experiment, the minimum reflectance pixel position is tracked as a function of time to quantify binding events at stBLMs. A response, R, is measured relative to a baseline reading which is typically the response value for an equilibrated freshly formed stBLM. Data was then analyzed to determine the dissociation constant, K_d, between protein and binding substrate at equilibrium. An exemplary sensorgram is shown in Figure 2.6. The Langmuir model describes ideal 1:1 binding interactions without cooperativity between two species A and B. Two binding parameters describe the dynamic equilibrium between the bound and unbound states: the association rate constant k_on and the dissociation rate constant k_off. The rate at which A and B bind to form AB can then be written as

$$\frac{\mathrm{d}}{\mathrm{d}t}[AB] = k_\mathrm{on}[A][B] - k_\mathrm{off}[AB] \tag{2.14}$$

where brackets denote species concentration. In dynamic equilibrium, the rates of association and dissociation match such that Equation 2.14 is zero. K_d can then be defined as

$$K_\mathrm{d} = \frac{k_\mathrm{off}}{k_\mathrm{on}} = \frac{[A][B]}{[AB]} \tag{2.15}$$

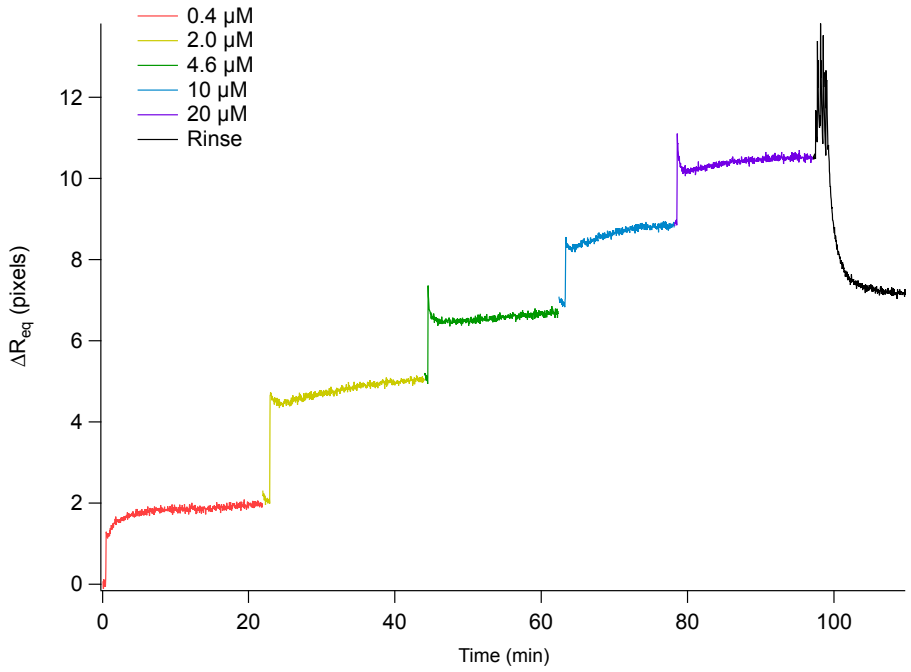

Figure 2.6: Exemplary SPR sensorgram from a binding analyte titration. An increasing concentration of binding analyte is introduced to an stBLM system and the response (change in signal compared to a baseline) is quantified. The response values after equilibration of the signal are recorded and a Langmuir binding model is fit to the data.

The analogous association constant, $K_\mathrm{a} = 1/K_\mathrm{d}$, can be similarly defined. Experiments can be designed to estimate K_d by measuring the concentration of bound species $[AB]$ at varying concentrations of a single species [A]. If a saturation concentration is $[AB]_\mathrm{max}$ then

$$[B] = [AB]_\mathrm{max} - [AB] \tag{2.16}$$

and equation 2.15 can be rearranged to yield the Langmuir isotherm

$$[AB] = \frac{[AB]_\mathrm{max}[A]}{K_\mathrm{d} + [A]} \tag{2.17}$$

In typical SPR binding experiments, if species B represents binding sites for the analyte A, and $[AB]$ is proportional to the SPR response R, then $R = R_\mathrm{eq}$ and $[AB]_\mathrm{max} = R_\infty$

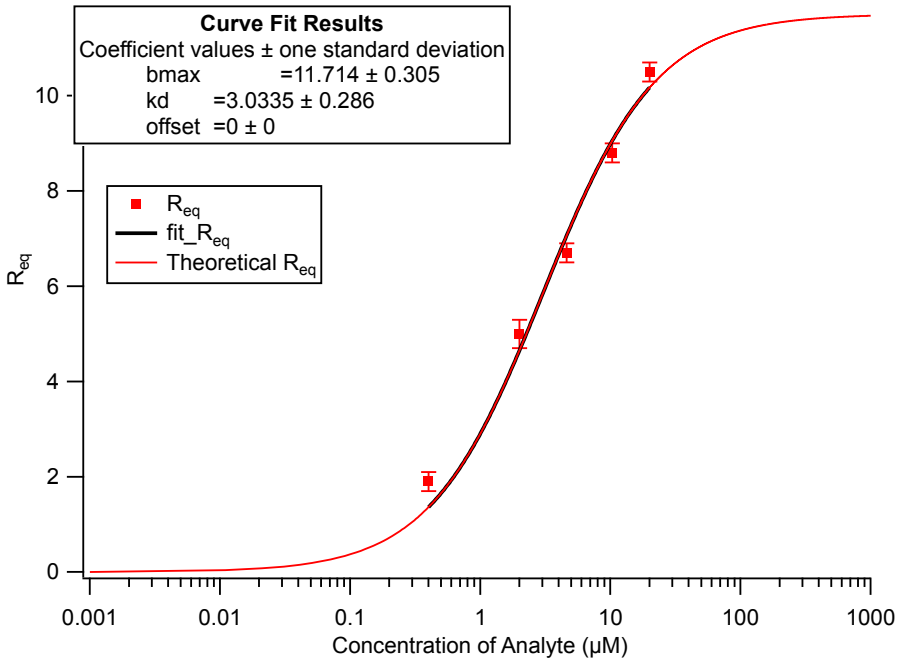

Figure 2.7: Langmuir model fit to equilibrium SPR response values. Two fit parameters are determined from Langmuir binding models: the response at saturation R_∞ and the dissociation constant K_d where K_d is the concentration at which half of the binding sites are occupied.

at equilibrium:

$$R_\mathrm{eq} = \frac{R_\infty [A]}{K_\mathrm{d} + [A]} \tag{2.18}$$

Data containing R_eq values at varying analyte concentrations $[A]$ can be fit with Equation 2.18 to estimate K_d as depicted in Figure 2.7.

In chapter 3, an experimental system was analyzed including one receptor protein, $[A]$, and a ligand existing in either unbound or membrane-bound states, denoted as $[B]$ or $[C]$, respectively. The amount of membrane-bound ligand, $[C]$, depends on the concentration of free ligand $[B]$ as in Equation 2.17:

$$[C] = \frac{[C]_\mathrm{max}[B]}{K_\mathrm{d,C} + [B]} \tag{2.19}$$

where $K_\mathrm{d,C}$ is the dissociation constant describing $[B]$ binding the membrane and forming $[C]$. The dissociation constant describing the binding of free ligand $[B]$ to the receptor $[A]$ is denoted as $K_\mathrm{d,AB}$ and is defined in Equation 2.15. To estimate $K_\mathrm{d,AB}$, the free concentration of ligand was estimated from the Langmuir binding model, Equation 2.19,

by first incubating a ligand concentration of $[B]_1$ which is depleted by an amount $[C]_1$ to $[B]_1^*$ at equilibrium. In SPR experiments, the concentration of membrane-bound ligand is much less than the concentration of free ligand. Therefore, the free ligand concentration at equilibrium, $[B]_1^* \approx [B]_1$. A receptor protein at concentration $[A]$ is subsequently introduced which depletes the concentration of free ligand by $\Delta[B] = [B]_1 - [B]_2$ and results in a loss of membrane-bound ligand $[C]_1$ to $[C]_2$. The receptor concentration also drops to a value of $[A] - \Delta[B]$. As a result, the SPR response, which quantifies $[C]$ in terms of $[B]$, can be used to estimate the amount of free ligand in the system before and after the receptor protein is introduced. The dissociation constant between the receptor $[A]$ and ligand $[B]$ is then estimated as

$$K_{\mathrm{d,AB}} = \frac{([A] - \Delta[B])(\Delta[B])}{[AB]} \tag{2.20}$$

The Gibbs free energy of binding can be readily calculated from K_{d} as

$$\Delta G^{\mathrm{o}} = RT \ln(K_{\mathrm{d}}/c_{\mathrm{ref}}) \tag{2.21}$$

where R is the universal gas constant, T is temperature in Kelvin, and c_{ref} is a reference concentration which is taken to be the number of moles of liquid water per liter, 55.5 mol/L [59].

2.4 Specular Neutron Reflectometry

2.4.1 Introduction

Neutron reflectometry (NR) is a powerful and versatile structural characterization technique for multi-layered biological systems of planar geometry. In the timescale of a typical experiment, NR is non-destructive, which allows the user to measure a given sample in a variety of conditions. The supported lipid bilayer is a common system in NR studies which can be probed to a spatial resolution of 5 Å [60]. Neutron scattering events are principally due to interactions with nuclei constituting the sample environment; isotopic labeling of a protein in a biomolecular complex allows for a significant increase in the information content of the scattering length density profile. The use of deuterated water as a bulk solvent provides additional means of distinguishing scattering contributions of the sample of interest and solvent [61].

2.4.2 Theory

Experiments which utilize NR yield one-dimensional reflectivity data describing the in-plane averaged structure of layered systems. The discussion here will be limited to specular scattering of neutrons in which the angle of incidence and reflection with respect to the normal vector are equivalent, and equal to θ, while the directions of incident radiation, reflected radiation, and normal vector lie within the same plane (see Figure 2.8). The theoretical description of neutron reflection here assumes neutron wave fronts can be approximated as plane waves over the sample area. A necessary condition for this assumption is that the area illuminated by the neutron beam is sufficiently large to average over any in-plane inhomogeneities at interfaces. The size limit on interfacial inhomogeneities is described in terms of an instrument-dependent transverse coherence length. For NR studies of lipid bilayer systems, this length can be approximated using the width of the wavelength-distribution of incident neutrons, $\Delta\lambda$, and is typically is on the order of microns. A thorough discussion of the transverse coherence length and a means of determining it can be found in [62].

Structural information from neutron reflectometry is described in terms of a one-dimensional neutron scattering length density profile $\rho(z)$ in the direction perpendicular to the sample plane. The scattering length density profile is derived from measured reflectivity of the sample with respect to the momentum transfer vector q_z defined by equation 2.22 and is depicted in Figure 2.8.

$$\begin{aligned} \vec{q_z} &= \vec{k_r} - \vec{k_i} \\ q_z &= k_{r,z} - k_{i,z} = 2|k_i| \sin\theta \\ q_z &= \frac{4\pi}{\lambda} \sin\theta \end{aligned} \tag{2.22}$$

where k is the neutron wave vector with wavelength λ. Subscripts r and i indicate reflected and incident waves, respectively. To arrive at a definition for reflectivity R, it is useful to describe interactions of neutrons and sample materials in terms of an index of refraction. Neutron reflectometry is sensitive to the index of refraction profile of multi-layered materials in the normal direction. For a given material, the neutron index of refraction is

$$n = 1 - \frac{\lambda^2 N_\mathrm{d} b}{2\pi} + \frac{i\lambda N_\mathrm{d} \sigma_\mathrm{d}}{4\pi} \tag{2.23}$$

where N_d is the atomic number density, b is the coherent scattering length for neutrons, and σ_d is the adsorption cross-section. For materials utilized in this work, the adsorption cross-section is essentially zero and with the neutron scattering length density (nSLD),

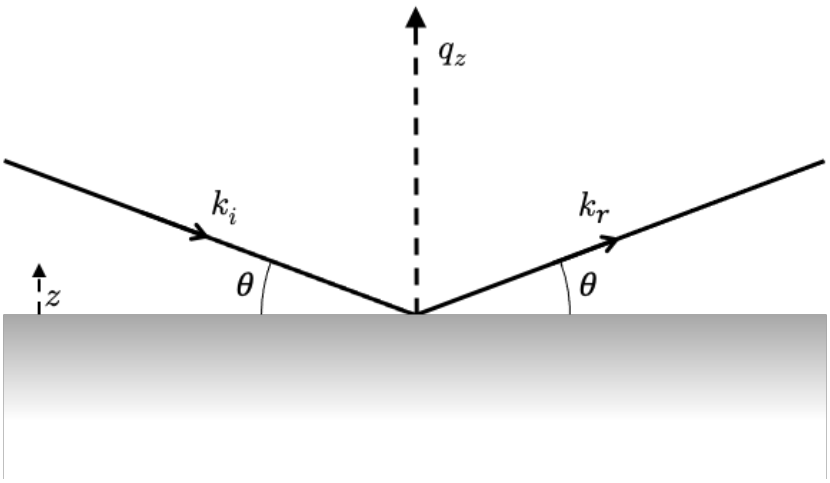

Figure 2.8: Depiction of the momentum transfer in NR. The incident wave vector k_i and reflected wave vector k_r make an angle θ relative to the interface. The change in momentum of the reflected radiation relative to the incident radiation lies entirely in the direction normal to the surface.

$\rho = N_\mathrm{d} b$, the neutron refractive index can be approximated as

$$n \approx 1 - \frac{\lambda^2}{2\pi}\rho \tag{2.24}$$

With the neutron refractive index, Snell's law can be used to obtain the total reflection condition expressed in terms of indices of refraction of neighboring mediums 1 and 2. The critical angle for total reflection is given by

$$\cos\theta_\mathrm{c} = \frac{n_2}{n_1} \tag{2.25}$$

With neutrons incident from air, this can be expressed entirely in terms of medium 2 ($n_2 = 2$).

$$\cos\theta_\mathrm{c} = n \tag{2.26}$$

For sufficiently small θ_c, a Taylor expansion can be performed and combined with Equation 2.24 yielding

$$n = 1 - \frac{\theta_\mathrm{c}^2}{2} \tag{2.27}$$

where

$$\theta_c = \lambda\sqrt{\frac{\rho}{\pi}} \tag{2.28}$$

The critical momentum transfer wave vector q_c is then

$$q_c = \frac{4\pi}{\lambda}\sin\theta_c = 4\sqrt{\pi\rho} \tag{2.29}$$

NR studies for describing interfacial structures are performed at angles exceeding the critical angle for reflection to measure sample reflectivity as a function of momentum transfer. The reflectivity is the squared modulus of the complex reflection coefficient, the ratio between the reflected and incident amplitudes of neutron plane waves.

In the case of reflection from multiple layers, the interference of reflections from all m (smooth) layers between the i^{th} and j^{th} layers can be quantified in terms of the reflection coefficient as

$$r'_{i,j} = \frac{r_{i,j} + r_{j,j+1}e^{2i\beta_j}}{1 + r_{i,j}r_{j,j+1}e^{2i\beta_j}} \tag{2.30}$$

with

$$\beta_j = \frac{2\pi}{\lambda}n_j d_j \sin\theta \tag{2.31}$$

$$r_{i,j} = \frac{n_i\sin\theta_i - n_j\sin\theta_j}{n_i\sin\theta_i + n_j\sin\theta_j} \tag{2.32}$$

where n_j and d_j are the thickness and refractive index of the j^{th} layer. This calculation can then be performed recursively until $r_{0,1}$ is calculated yielding the measured reflectivity of the sample, $R = |r^2|$. The squared modulus of the reflection coefficient results in the loss of so-called "phase-information" in the reflected wave. Methods have been developed using reference layers to measure the phase of the complex reflection coefficient but are not discussed in this work [63, 64].

Surface undulations, or roughness, at interfaces lead to attenuation of the measured reflectivity profile. Broadly, interfaces with higher roughness yield lower reflectivity as q_z increases. Roughness can be modeled, using the Nevot-Croce approximation, as a Gaussian parameter, σ [65] such that the reflectivity, R, is attenuated as:

$$R' = Re^{-{q_z}^2\sigma^2} \tag{2.33}$$

To effectively characterize structures in NR studies, substrate roughnesses are ideally between 3 and 5 Å.

2.4.3 Instrumentation

The NGD-Magik reflectometer at the NIST Center for Neutron Research (NCNR) in Gaithersburg, MD was used for data collection from samples discussed in this work. The neutron beam was of wavelength $\lambda = 5$ Å and the angle of incidence of varied to obtain a range in q_z of 0.008 to 0.250 Å^{-1}. The NR fluid cell was constructed such that the neutron beam is incident from the substrate side of the sample before impinging on the fluid reservoir. A Denton Vacuum Discovery 550 Sputtering System deposited films of approximate 3 nm chromium and 15 nm gold onto a silicon wafer. SAMs and stBLMs were formed as described in previous sections. All experiments were performed in ambient temperature, 22 ± 1°C.

2.4.4 Data Acquisition

For membrane protein studies, newly prepared stBLMs were first measured in D_2O and H_2O isotopic contrasts. Buffer exchange was performed via syringe pump by flushing 10 mL buffer through the fluid cell (approximately 1.3 mL volume) to ensure complete transfer. After initial NR collection, a protein solution (approximately 1.5 mL) is manually injected into the cell and allowed to incubate for 1 hr followed by a buffer rinse. Following the buffer rinse, NR measurements are performed to characterize any tightly bound protein at the stBLM. Each measurement is performed for 5-7 hours to obtain reasonable counting statistics across the momentum transfer range. This process was repeated in both isotopic contrasts.

2.4.5 Data Analysis

NR data was analyzed with the garefl and Refl1D software packages [64] to obtain a neutron scattering length density (nSLD) profile in the direction normal to the surface which accounts for all structural components of the sample. In general, it is difficult to determine a unique solution to scattering problems due to the loss of phase information. Various strategies can be applied to ameliorate this issue using additional information such as known structural parameters of components (lipid lengths, etc.), two solvent contrasts, and simultaneous fitting of multiple datasets [47, 64]. For a given experiment, a single substrate is measured under all experimental conditions to ensure consistency and confidence across modeled compositional profiles with shared fit parameters describing the substrate. The nSLD profile normal to the substrate is determined using a combination of modeling techniques. A slab model is used to

describe substrate layers [66], a compositional space model for supported bilayers [46], and a Hermite spline model for model-free protein densities [47].

The slab model characterizing the solid substrate defines multiple layers (typically silicon, silicon oxide, chromium, and gold) where the nSLD and thicknesses are treated as fit parameters. Only the bulk silicon layer nSLD was fixed at a known value. The interface between two layers are modeled with error functions defined with a roughness parameter. Silicon oxide and the amorphously sputtered layers of chromium and gold do not have well-defined nSLD values and are therefore treated as fit parameters.

A continuous distribution model was used to determine nSLD profiles constrained within a compositional space [46]. Additional information can be incorporated to reduce the number of fit parameters and constrain fit ranges thereby increasing the precision in localization of molecular components. For example, the volume of lipid components are known from auxiliary methods such as X-ray diffraction [67] and couples headgroup and hydrocarbon thickness parameters. To model the spatial distribution of individual components, two error functions are summed. To properly model the structural complexity, the individual distributions are allowed to overlap, and any remaining volume occupancy is filled with solvent. Components for stBLMs include βMe, HC18 glycerol, HC18 polyethylene glycol chains, lipid headgroups (inner and outer leaflet), lipid methylene chains (inner and outer leaflets), and terminal methyl groups for lipid and tether. SLB components varied depending on the sample to include a single leaflet for characterizing a lipid monolayer at the interface or two leaflets for fully formed bilayers. Fit parameters included βMe surface density, tether density, tether thickness, inner and outer hydrocarbon thicknesses, and bilayer completeness for stBLMs. SLB studies included inner and outer hydrocarbon thicknesses for bilayers (a single leaflet for monolayers) and an additional thickness for a hydrated sub-membrane layer. Headgroup dimensions are too small to be determined with NR and are fixed at values obtained from molecular dynamics simulation.

Protein density was modeled with a free-form Hermite spline starting from the substrate surface along the normal direction [47]. A user specified number of control points was used to construct the spline profile which were distributed along the surface normal at regular intervals of 15 Å. Each control point had an associated volume occupancy and was allowed to deviate from its position. The nSLD of the profile is fixed at the average value for protein while taking into account proton exchange with the solvent. A control fit is typically performed for two identical data sets from neat bilayers. One data set is modeled in a composition space without protein density and the other data set is modeled with a composition space including a protein density. By fitting identical data sets in this manner, systematic errors are manifest as erroneous protein density.

Uncertainty determination

A robust method for quantifying uncertainties is critical in modeling NR data while avoiding over-parameterization. The Monte Carlo Markov-Chain simulation algorithm, DREAM [68], was used to estimate parameter uncertainties. DREAM explores parameter space around minima via a Metropolis algorithm to yield pair-wise correlations of fit parameters and optimize a negative log likelihood of seeing the data given the model. Properly implemented, the number of times a particular set of parameter values is visited is directly proportional to the likelihood function at those parameter values. This method also allows uncertainties on combinations of parameters to be determined such as calculating the area per lipid.

Rigid Body Modeling

Although NR yields a one-dimensional profile describing the three-dimensional molecular structure, complementary structural characterization techniques can be used to determine three-dimensional information consistent with NR data. NMR and crystallographic structures are regularly incorporated in analysis of NR experiments [47,49,53]. Atomistic protein structures can be integrated by slicing the structure into slabs along the membrane normal and assigning each slab a corresponding cross-sectional area and neutron scattering length. The free-form Hermite spline nSLD can be directly compared to this atomistically derived profile to determine whether the protein density can be described as a monolayer, if the protein reorganizes at the membrane, and the degree of membrane penetration.

Rigid body modeling of the protein structure can be incorporated to determine an orientation with respect to the membrane. Two Euler angles are used to describe the orientation β and γ. NR is insensitive to rotations about the z-axis, the membrane normal direction. As a result, the α Euler angle does not contribute to the nSLD. The space of all orientations is explored by first rotating by γ about the membrane normal followed by β about the x-axis in the plane of the membrane. nSLD profiles are calculated as previously described and uncertainty analysis is performed to determine probabilities associated with each orientation.

2.5 Small-angle X-ray Scattering

2.5.1 Introduction

Structural determination of biological macromolecules in relevant contexts remains a key challenge in the field of biophysics. Small-angle X-ray scattering (SAXS) studies provide low-resolution structural information of biomolecules under physiological conditions.

Modern innovations in coupling molecular dynamics simulation and machine learning methods into SAXS analysis continues to improve the speed and accuracy of data interpretation [69–72]. SAXS is applicable to a comparatively large range of macromolecular size and shape (domain sizes are within 1 to 100 nm) relative to methods which provide higher resolution structural information under highly specific sample conditions such as X-ray crystallography and NMR. Typical restrictions include a sufficiently dilute sample to ensure monodispersity and non-interacting particles. In solution SAXS, a collimated X-ray beam irradiates a sample yielding a two-dimensional scattering pattern. This pattern is typically radially averaged and converted to a one-dimensional scattering intensity profile. Physical parameters describing average particle size and shape are directly calculable from the collected scattering profile such as the radius of gyration, molecular weight, and the maximum spatial dimension.

2.5.2 Theory

Presented here is a brief overview of the connection between the measured intensity in SAXS experiments and the underlying structure of particles in solution. When a plane wave of wave vector $\vec{k}$ is incident on an object, the atoms within the object become sources of spherical waves. Under the Born approximation, the scattered spherical waves are considered to be due to only the incident radiation. Detectors in SAXS experiments are at a sufficiently large distance to model the total interference of the scattered waves as a plane wave with wave vector $\vec{k'}$. In elastic scattering, the magnitude of the incident wave vector is equal to the scattered wave vector $\left|\vec{k}\right| = \left|\vec{k'}\right| = k$. The momentum transfer vector is defined as

$$\vec{q} = \vec{k'} - \vec{k} \tag{2.34}$$

A simplified schematic of a typical small-angle scattering experiment is shown in Figure 2.9. A radiative source emits particles at a known wavelength λ. The sample is placed in the path of collimated radiation. Further along the beam path, a two-dimensional detector is held at a known distance which counts the scattered radiation. After radially averaging the scattering radiation across the detector, one can define an angle 2θ to describe the angle a scattered particle diverges from the incident beam path. The magnitude of the momentum transfer vector is then

$$|\vec{q}| = q = \frac{4\pi}{\lambda} \sin 2\theta \tag{2.35}$$

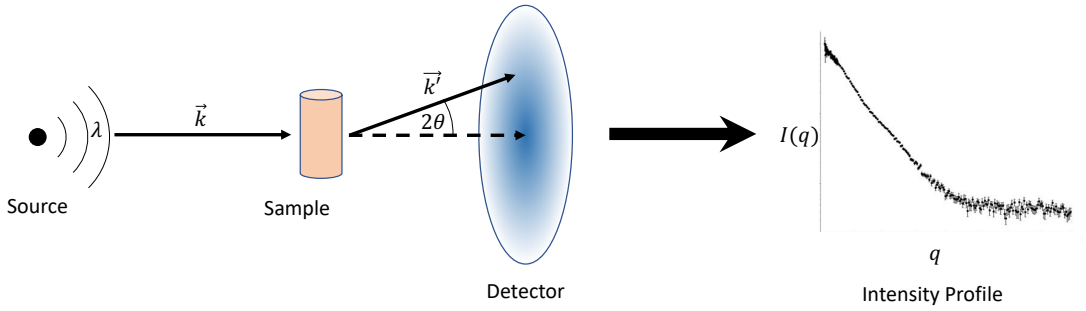

Figure 2.9: A typical SAXS experiment. A radiated plane wave of wavelength λ, described by wave vector $\vec{k} = 2\pi/\lambda$, is incident on a sample which elastically scatters photons at a wave vector $\vec{k'}$ with angle 2θ. Scattered photons are detected in a 2-D plane which is averaged during the data reduction procedure (described in a subsequent section) to yield a 1-D scattered intensity profile.

The scattered intensity measured by a detector is directly proportional to the differential cross-section for scattering which is ratio of scattered power radiated into a unit solid angle to the incident power per unit area. The differential cross-section can be described in terms of a scattering amplitude $A(q)$ such that

$$I(q) \sim \frac{\mathrm{d}\sigma}{\mathrm{d}\Omega} = |A(q)|^2 \tag{2.36}$$

An X-ray beam will interact with the electrons of a particle described by a scattering length density $\rho(\vec{r})$. This density describes the strength of interaction within the sample at each point in three-dimensional space. The particles in solution are present in every orientation relative to the beam path. Therefore, given a monodisperse sample, $I(q)$ will be proportional to the intensity profile of a single particle averaged over all possible orientations. $I(q)$ contains one-dimensional information about the three-dimensional particle scattering length density $\rho(\vec{r})$. The scattering amplitude $A(q)$ of a single particle

can be expressed in terms of $\rho(\vec{r})$ via Fourier transformation:

$$A(\vec{q}) = \mathcal{F}[\rho(\vec{r})] = \int_V \rho(\vec{r}) e^{i\vec{q}\cdot\vec{r}}\, \mathrm{d}\vec{r} \tag{2.37}$$

where integration is performed over the scattering volume. The measured intensity profile $I(q)$ is therefore proportional to the squared modulus of the spherically averaged particle electron density, $\rho(\vec{r})$ in Fourier space.

$$I(q) \sim \left\langle \left| \int_V \rho(\vec{r}) e^{i\vec{q}\cdot\vec{r}}\, \mathrm{d}\vec{r} \right|^2 \right\rangle_\Omega \tag{2.38}$$

2.5.3 Instrumentation

Solution X-ray scattering data was collected with the MOLMEX Ganesha instrument at the Institute for Bioscience and Biotechnology Research (IBBR, Rockville, MD). Incident copper Kα radiation with a wavelength of 1.542 Å was produced by a Rigaku MicroMax 007HF rotating anode generator and two sets of scatter-less slits monochromated and colliminated the beam. The Pilatus 300K detector registered scattered radiation and the directly transmitted intensity was monitored by a pin diode. Protein samples were loaded into a cylindrical capillary with 1.5 mm path length in the beam path and kept at 25 °C.

2.5.4 Data Acquisition

Samples were exposed to the incident X-ray radiation for the duration of 16 sequential 900 s frames. Pixel intensity outliers due to the background cosmic radiation were removed, and the 2D data were corrected for the detector sensitivity profile and the solid angle projection per pixel. The data were converted to one-dimensional scattering intensity curves, frame-averaged, and buffer-subtracted taking into account the concentration-dependent volume fraction of solute in the samples. Data sets acquired at sample-detector geometries of 1035 mm and 355 mm were merged to extend the angular resolution range. Scattering data from SmgGDS variants were acquired for 1.0 mg/mL and 0.5 mg/mL SmgGDS-558, and 2.0 mg/ml SmgGDS-607. Data from mixed samples of SmgGDS and KRas were collected at 1.4 mg/mL total concentrations including two-fold dilutions in 1:1 molar ratios.

2.5.5 Data Analysis

SAXS data was analyzed with programs from the ATSAS [73] suite. PRIMUS [11] was used merge low-angle data from two-fold diluted samples with high-angle data from stock concentrations in overlapping regions to minimize the scattering contribution of non-specific aggregation. PRIMUS additionally provides a graphical interface to perform Guinier analysis on low angle data to obtain estimates on the forward scattering $I(0)$ and radius of gyration R_{g}. Estimates of the radius of gyration and forward scattering from Guinier analysis can be compared to estimates calculated from the pair-distance distribution function $p(r)$. Modeling the pair-distance distribution function was performed the GNOM program [12]. DATMW was used to perform concentration-independent predictions of the molecular weights of the scattering particles within samples. Theoretical SAXS data was calculated from atomistic structures and fit to experimental data using CRYSOL3 [70] including a constant background term.

Guinier approximation

At low q-values, the scattering profile can be approximated [74] in the form

$$I(q) \approx I(0) e^{-\frac{R_{\mathrm{g}}^2}{3} q^2} \tag{2.39}$$

Taking the log of Equation 2.39 establishes a linear relation between the log of $I(q)$ and q^2 where the slope is only in terms of the apparent R_{g} as

$$\log I(q) \approx \log I(0) - \frac{R_{\mathrm{g}}^2}{3} q^2 \tag{2.40}$$

A linear fit of $\log(I(q))$ *vs.* q^2 can obtain the radius of gyration and forward scattering intensity from the slope and y-intercept, respectively. In general, the valid q-range is restricted to $qR_{\mathrm{g}} < 1.3$ for globular proteins and is smaller for extended molecules [75]. Guinier analysis also can be used to assess data quality based on signatures of sample aggregation, radiation damage, and interparticle interactions [76].

Pair-distance distribution

While Guinier analysis yields structural parameters using low-q information, the pair-distance distribution function $p(r)$ can be calculated utilizing the entire scattering profile.

$$p(r) = \frac{r^2}{2\pi^2} \int_0^\infty I(q) \frac{\sin qr}{qr} q^2 \, \mathrm{d}q \tag{2.41}$$

In practical terms, this calculation cannot be performed with real SAXS data sets and must be approximated. General assumptions are made such as vanishing density at $r = 0$ and at a maximum particle distance $D_{\max}$ which must be specified by the user. Determining the maximum particle distance to specify is not an exact science but can be estimated by examining the shape of the distance distribution for varying values of $D_{\max}$. Solutions which display oscillations or extended tails should generally be avoided. Agreement between R_{g} from Guinier analysis and as calculated from the distance distribution function is desired when finding a reasonable solution. The radius of gyration is the second moment of the pair-distance distribution:

$$R_{\mathrm{g}}^2 = \frac{\int_0^{D_{\max}} r^2 p(r)\,\mathrm{d}r}{\int_0^{D_{\max}} p(r)\,\mathrm{d}r} \tag{2.42}$$

The forward scattering intensity can be calculated with

$$I(0) = 4\pi \int_0^{D_{\max}} p(r)\,\mathrm{d}r \tag{2.43}$$

Molecular Weight Estimation

A Bayesian inference method was utilized to estimate molecular weight from SAXS data by inferring the probabilities of molecular weight values with molecular weight estimates from four concentration-independent methods [72]. Using the terminology in the referenced publication, potential values of molecular weight are treated as a hypothesis H and the estimates from concentration-independent methods are evidence E. The four methods which provide evidence are a calculations based on the Porod invariant Q_{P}, the volume of correlation, the *SAXSMoW* volume correction, and the *Size&Shape* method.

The Porod invariant [77], Q_{P} can be calculated as

$$Q_{\mathrm{P}} = \int_0^{\infty} I(q) q^2\,\mathrm{d}q \tag{2.44}$$

where $I(q)$ is the measured SAXS intensity. This method of estimating molecular weight assumes the scattering particles have constant scattering length density throughout their volume. The corresponding Porod volume V_{P} is calculated as

$$V_{\mathrm{P}} = \frac{2\pi^2 I(0)}{Q_{\mathrm{P}}} \tag{2.45}$$

The lower integration limit for calculating the Porod invariant can be obtained from Guinier approximation of the forward scattering intensity $I(0)$ while the upper limit

is evaluated up to $qR_g = 8$ and extrapolated to infinity. The volume of correlation V_c was defined based on another scattering invariant involving an integral of the scattering intensities. A ratio of the volume squared to the radius of gyration was found to be proportional to the molecular weight of the proteins used to assess the model.*SAXSMoW* uses the Porod invariant but with a different range of integration [78]. Additionally, the calculated volume contains correction factors which were obtained from theoretical scattering profiles of atomistic structures from the Protein Data Bank. This method multiplies the volume by the average mass of protein, 830 kDa/Å^3. Finally, *Size&Shape* [79] uses size and shape estimates from 165,982 protein structures from the Protein Data Bank to compare the experimental data to. The size and shape from the measured intensity profile is calculated and a weighted average of the molecular weights of five nearest neighbors in a four-dimensional "size-and-shape" space is calculated.

Bayesian inference takes the molecular weight estimates from the previous methods as evidence E to infer probabilities of hypothetical molecular weights, H, for a given SAXS data set. Bayes theorem is applied to produce an expression for the probability of a hypothetical molecular weight H given evidence from each method, $E_{\mathrm{MW}_{Q_\mathrm{P}}}$, E_{V_c}, E_{MoW}, and $E_{\mathrm{Size\&Shape}}$:

$$P(H|E) = \frac{P(E_{\mathrm{MW}_{Q_\mathrm{P}}}|H)P(E_{\mathrm{MoW}}|H)P(E_{\mathrm{Size\&Shape}}|H)P(H)}{P(E)} \tag{2.46}$$

A bank of 223,045 atomistic structures from the Protein Data Bank was used to test and train the Bayesian model. This method of molecular weight estimation was reported to have higher accuracy compared to any single determination method regardless of signal-to-noise level and particle shape [72].

CRYSOL3

Various methods for calculating theoretical SAXS profiles from atomistic structures of macromolecules exist in the literature [45, 69, 80–82]. Among the most popular methods is CRYSOL [70, 81] which uses a multipole expansion of the scattering amplitudes of models to calculate a spherically averaged scattering intensity profile. Modeling the hydration layer of macromolecules is of critical importance to accurately describe SAXS data [83]. The contrasts of bulk solvent and the hydration layer can differ significantly and greatly affect the calculated scattering profile [81, 84, 85]. Two versions of CRYSOL are available that differ in their methods of modeling the hydration layer: CRYSOL, originally developed in 1995, models the hydration layer as an enveloped function with constant contrast, and includes additional parameters such as atomic radii and background scattering; CRYSOL3 generates dummy water beads on the surface of the atomistic model [70, 81]. CRYSOL has changed significantly since its publication in

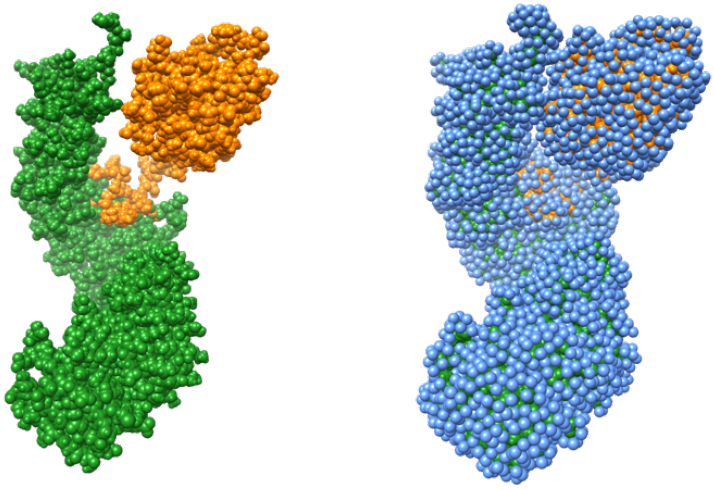

Figure 2.10: Visualization of hydration layer modeling by CRYSOL3. A sample atomistic structure of SmgGDS-558 (green) bound to KRas-FMe-GDP (orange) is shown and was generated with Chimera [5]. CRYSOL3 predicted the SAXS intensity pattern of the complex and fit the profile to experimental data. The hydration layer at the surface of the molecular structure is modeled with dummy water beads (blue) located at: concave surfaces, convex surfaces, or at inner cavities. The scattering contrast of each bead type was varied in fitting to measured SAXS data.

1995 [86]. Among the changes is an additional fit parameter to describe the excluded volume. The water beads generated by CRYSOL3 are classified as being situated at an outer convex surface, concave surface, or inner cavity. The contrasts of each bead classification are varied from 2 to -10 times the bulk solvent contrast. Negative contrasts correspond to solvent-inaccessible regions. CRYSOL3 is reported to be more suitable for structures of non-globular shape or those which contain inner cavities [70]. A PDB file is generated when fitting a structure that contains atomic positions of the dummy water beads (an example is depicted in Figure 2.10).

Although CRYSOL3 was chosen to model SAXS intensity profiles in this work, there are non-trivial difficulties in its use. The ability to troubleshoot issues in fitting profiles to experimental data is significantly hindered due to a lack of detailed documentation. Further, only pre-compiled CRYSOL and CRYSOL3 is available to the public (as of this writing) that prevents any assessment of congruence between published articles describing the model's implementation and source code defining the computation of scattering intensities.

Hybrid modeling with SAXS

Modern structural characterization of biomolecules with SAXS frequently is supplemented by known high-resolution information [83]. Rigid-body and flexible docking simulations can be performed on atomistic models to aid in describing the structure of a multimeric complex [87,88]. A variety of software has been developed to adapt molecular dynamics and Monte-Carlo simulations to the analysis of SAXS data [69,89].

In this work, SAXS analysis was supplemented with molecular dynamics and Monte-Carlo simulations. GROMACS [90] was used to model equilibrium dynamics in solvent using input files generated from CHARMM-GUI [91,92]. Three phases of MD simulation were performed: energy minimization of the molecular structure, equilibration with solvent, and production. Protein atoms in each production frame were input into CRYSOL3 to predict scattering profiles and compared to measured data. A reduced chi-squared quality of fit, χ^2_{red}, was calculated for each frame defined as:

$$\chi^2_{\text{red}} = \frac{1}{1-N} \sum_{i=1}^{N} \frac{(I_{\text{exp}}(q_i) - I_{\text{model}}(q_i))^2}{\sigma^2_{\text{exp}}(q_i)}$$

where i iterates through each of the N data points in the scattering profile, $I_{\text{exp}}(q_i)$ is the measured intensity for the ith data point, $I_{\text{model}}(q_i)$ is the predicted intensity, and σ_{exp} is the error.

Monte-Carlo simulations were performed using the SASSIE-WEB service [69]. Structures are simulated at 300 K by varying the torsion angles within a specified backbone region and samples are recorded if they are consistent with energetically allowable values. The angle was accepted if the associated Boltzmann factor is positive. Rejected structures are occasionally accepted at random. User-specified restraints can confine sampling to conformations of interest based on separation distances between atom groups. SAXS intensities were computed for every accepted sample with CRYSOL3 and the reduced chi-squared was calculated while fitting the experimental data. The simulated population of structures can then be pruned based on the quality of fit and visualized with Gaussian cube density files from the Density Plot module.

Chapter 3

Interactions of SmgGDS isoforms with fully processed KRas: membrane and solution studies

3.1 Introduction

The Ras family of small GTPases participate in signal transduction in a diverse set of cellular pathways including proliferation, survival, and migration [20,93,94]. The human RAS gene encodes four isoforms: HRas, NRas, KRas4A, and KRas4B. KRas4B (hereafter referred to as KRas) is the most frequently mutated isoform of the Ras family found in human cancers [95]. Small GTPase proteins typically have a low molecular weight (20 to 30 kDa) and commonly share a G-domain which serves as the site for hydrolysis of guanosine-triphosphate (GTP), converting it into guanosine-diphosphate (GDP) [30]. Activation of small GTPases is regulated by guanine nucleotide exchange-factors (GEFs) which promote the release of GDP to bind GTP, after which the small GTPases enters the active state. GTPase-activating proteins (GAPs) subsequently catalyze the hydrolysis of bound GTP to form GDP, defining the inactive state [96].

Ras proteins participate in signaling cascades at the plasma membrane (PM) where they are anchored by insertion of a C-terminal hydrophobic prenyl group, a result of post-translational modification [29]. Newly synthesized Ras GTPases undergo prenylation followed by several additional post-translational modifications before localizing at the PM [30]. A flexible C-terminal hyper-variable region (HVR) that extends from the G-domain differs significantly between Ras members. The HVR contains a poly-basic region (PBR) which is known to serve roles in their membrane localization and cytosolic trafficking [27,28]. A C-terminal cysteine residue in a CaaX motif (a is any aliphatic residue and X is any residue) undergoes post-translational modification by

farnesyltransferases which attach a hydrophobic farnesyl tail followed by cleaving of the aaX sequences by Ras-converting enzyme 1 (Rce1) at the endoplasmic reticulum (ER) [97]. A subset of Ras proteins contain an additional cysteine residue and undergo additional palmitoylation [28,98]. This process is terminated by carboxymethylation of the farnesylated cysteine by isoprenylcysteine carboxyl methyltransferase (Icmt) [27]. After prenylation and post-prenylation processing are completed, chaperone proteins, such as PDEδ, bind and solubilize fully processed Ras proteins to redistribute them throughout the cell [31,99,100]. KRas has been shown to bind PDEδ through interactions with residues downstream from the PBR. Additionally, the farnesyl was found to insert into a hydrophobic pocket in PDEδ [33]. Release factors Arl2 and Arl3 then regulate membrane localization of KRas by binding PDEδ, facilitating the release of KRas in the membrane-localization pathway [101,102].

KRas (Figure 3.1)localizes at the PM using both electrostatic and hydrophobic interactions. The C-terminal farnesyl chain inserts into the lipid membrane while the six lysine PBR associates anionic lipid components. Once bound, KRas diffuses into distinct nucleotide-dependant nanodomains [103]. Phosphatidylserine (PS) is specifically targeted by KRas and accumulates at KRas nanoclusters [104]. Recent structural studies show the G-domain of membrane localized KRas commonly adopting a membrane-distal state which could be important for binding downstream effectors [34].

SmgGDS (pronounced "smidge-GDS") is a major regulatory protein involved in the prenylation (a term describing the attachment of lipidic tails to small GTPases) and trafficking of many Ras and Rho proteins [8,105–107]. Two splice variants, named for the number of amino acids, are known: SmgGDS-607 which binds GTPases before they enter the prenylation pathway, and SmgGDS-558 which specifically binds prenylated small GTPases and regulates their membrane localization to the ER and PM [6,105,106]. Structurally, SmgGDS is composed of Armadillo Repeat Motif (ARM) domains labeled A-M where the shorter isoform, SmgGDS-558, lacks ARM C [105,108]. Association of the small GTPase RhoA with SmgGDS-558 has been well characterized and several binding regions of SmgGDS were identified. Mutational studies of SmgGDS and RhoA indicate an electronegative patch located on the concave surface of SmgGDS binds the PBR of RhoA and a highly conserved binding groove in SmgGDS binds the G-domain [8]. An X-ray diffraction derived crystal structure of a truncated SmgGDS-558 construct (containing amino acids 77-558) bound to farnesylated RhoA was determined revealing the location of a hydrophobic pocket in SmgGDS-558 between ARMs B and D (depicted in Figure 1) [7]. The pocket houses the prenyl group of RhoA in an analogous way to PDEδ binds the farnesyl tail of KRas [33]. SmgGDS-607 lacks this hydrophobic pocket due to the presence of ARM C. Although release factors, with functions similar to Arl2 and Arl3 for PDEδ, have not been identified, release factors may bind SmgGDS to eject the farnesyl of KRas, triggering its release [6]. A proof-of-principle was found in some

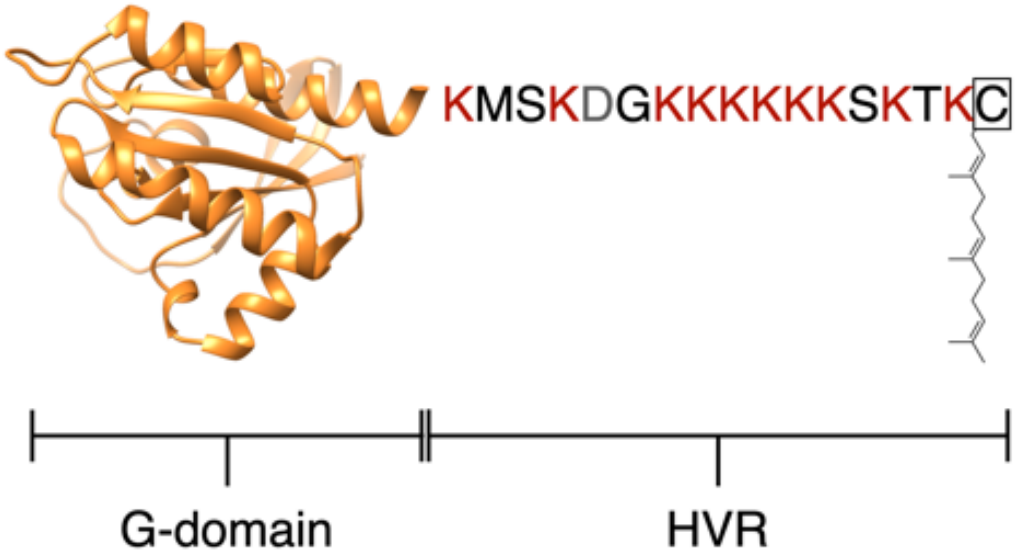

Figure 3.1: Illustration of KRas-GDP domains. The G-domain of KRas-GDP (PDB:4OBE) contains the site of nucleotide binding and hydrolysis. After being fully processed, the intrinsically disordered hypervariable region (HVR) consists of 19 residues (cationic residues in red, anionic in gray), a six lysine polybasic region (PBR), and C-terminal cysteine which undergoes farnesylation and carboxymethylation.

cancer cells where abnormal RabL3(1-36) forms a trimeric complex with SmgGDS and KRas accelerating the farnesylation and membrane localization of KRas [109].

Mutations of the small GTPase KRas are known to have significant oncogenic roles in human cancer [29,95,110,111]. Although co-expression of SmgGDS-558 and KRas has been shown to promote tumorigenesis in NIH3T3 cells [112], structural details of their association are not well understood. Additional information on their interaction is critical to further the understanding of their roles in both healthy and oncogenic cellular environments. Inhibiting KRas-PDEδ interactions with targeted chemical inhibitors were found to reduce signaling from oncogenic KRas. Because SmgGDS-558 shares function with PDEδ, a similarly developed chemical inhibitor that disrupts SmgGDS and KRas interactions could provide therapeutic benefits to cells with oncogenic KRas or SmgGDS [113,114]. Although both chaperone proteins participate in small GTPase trafficking, it is currently not know whether they exist in independent pathways. More information is needed to determine whether inhibiting KRas binding to one chaperone affects the activity of the other. In treated cells targeting PDEδ, SmgGDS could enable a redundant chaperoning pathway for KRas that remains active. A factor which could further complicate therapeutic targeting of KRas interactions with SmgGDS and PDEδ is that both chaperones have been shown to be important for the membrane localization and trafficking of several other small GTPases in the Rho and Rap families [99,115,116]. Therefore, developing a method which specifically targets

To better understand the binding of SmgGDS and fully processed KRas, I utilized in vitro characterization techniques at model membranes and in solution for the GDP-bound form. I additionally draw comparisons and analogies to a well-characterized complex of PDEδ and KRas [33]. To elucidate how the SmgGDS variants interact with membrane-bound KRas, the sparsely-tethered bilayer lipid membrane (stBLM) is utilized as a biomimetic substrate in surface plasmon resonance (SPR) studies [55]. The stBLM is composed of a nearly defect-free planar lipid bilayer supported by synthetic tether lipids bound to an atomically flat gold surface via thiol chemistry. The tether lipids are spaced on the surface through the co-adsorption of β-mercaptoethanol (βMe) to ensure a sufficiently hydrated submembrane environment and to retain the in-plane fluidity of the supported bilayer. SPR coupled with the stBLM platform is a highly sensitive technique to characterize the membrane-localization of protein [50,55].

Small-angle x-ray scattering (SAXS) is a structural characterization technique commonly used to describe biomolecular constructs in solution. Restrictions on the sample environment are minimal compared to higher resolution techniques such as NMR and X-ray crystallography while information on size, shape, and flexibility is readily attainable [117]. When combined with molecular dynamics simulation (MD), SAXS can provide significant insight for defining the structure of macromolecules with intrinsically disordered regions such as the HVR of Ras proteins [34,87,118].

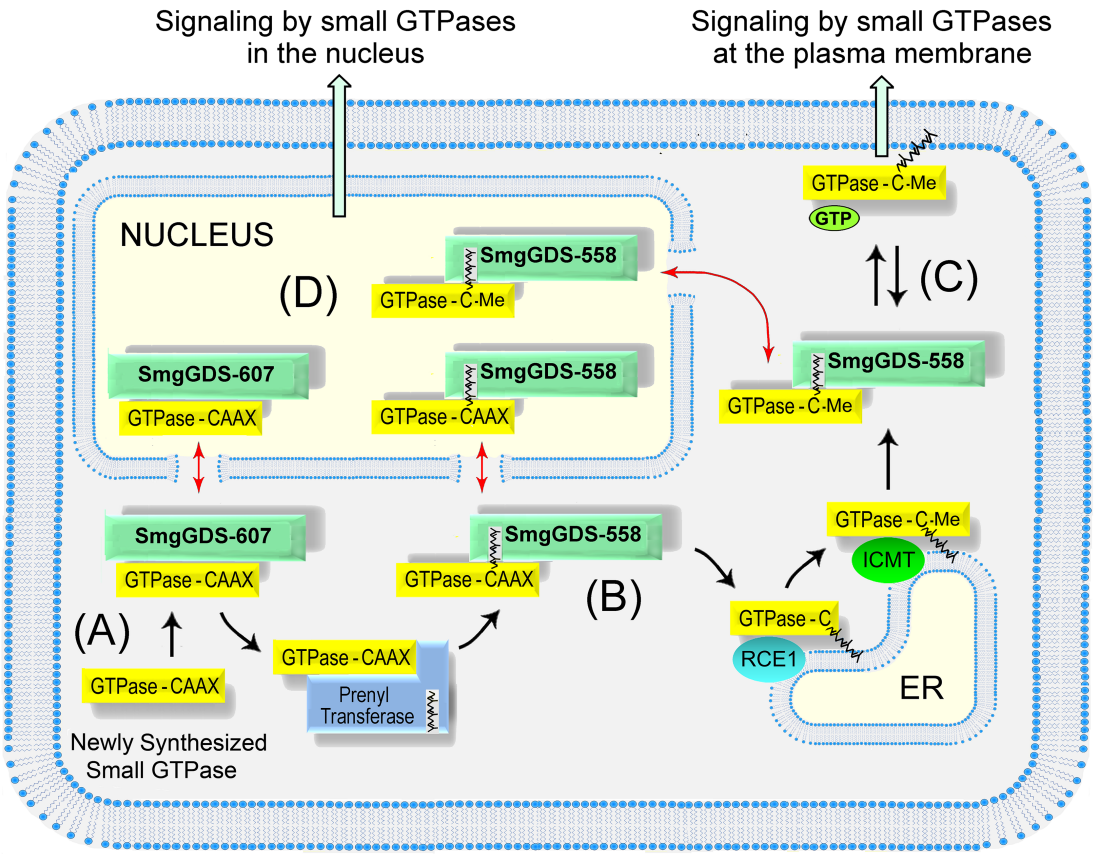

Figure 3.2: Model of the role of SmgGDS in regulating prenylation and membrane localization of small GTPases. *A:* Newly synthesized small GTPases bind SmgGDS-607 which moderates the attachment of a prenyl group by prenyl transferases. *B:* SmgGDS-558 solubilizes prenylated small GTPases and escorts them to ER membranes for further processing. *C:* Fully processed small GTPases are chaperoned by SmgGDS-558 from the ER to the PM to participate in signaling cascades. *D:* SmgGDS shuttles small GTPases to and from the nucleus. This work is primarily concerned with interactions of SmgGDS and fully processed KRas and evaluates the supposed role of SmgGDS-558 in escorting KRas-FMe through the cytosol from the ER. This figure is adapted from [6].

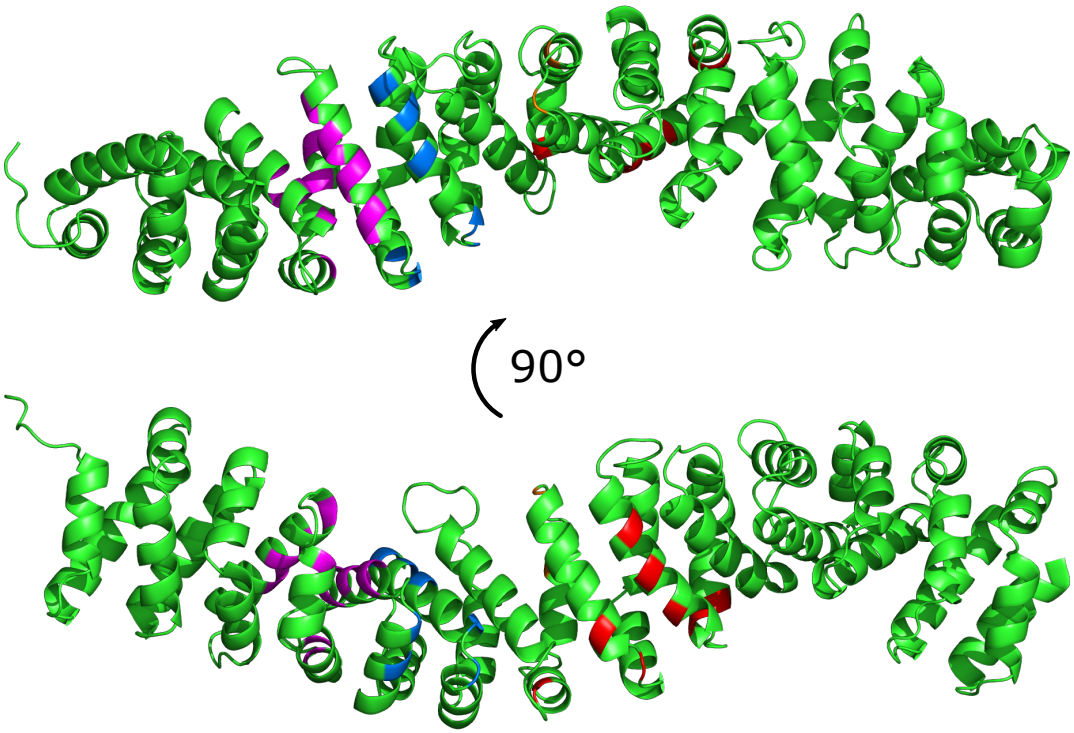

Figure 3.3: Structure of SmgGDS-558. A homology model of SmgGDS-558 is shown highlighting regions that have been identified as important for interacting with small GTPases containing PBRs. Residues constituting the hydrophobic pocket between ARMs B and D are shown in purple [7]. Residues subject to mutation in this study are also identified: anionic residues within the electronegative patch of SmgGDS are colored blue, residues within the conserved binding groove are colored red, and residues within the WIPSN sequence are orange [8, 9].

I present SPR membrane studies indicating that SmgGDS-558 readily solubilizes membrane-localized KRas to much greater extent than SmgGDS-607 does, and I provide an upper bound on the dissociation constant between SmgGDS-558 and fully processed KRas-GDP. Solution SAXS was used to characterize samples of SmgGDS isoforms and KRas-FMe-GDP. SmgGDS-558 and KRas were determined to form a 1:1 complex while SmgGDS-607 and KRas also associated but did not form a well-defined complex. Informed by SAXS data, I present an ensemble model of a KRas and SmgGDS-558 complex using molecular dynamics and Monte-Carlo simulations in which binding interactions are constrained by the C-terminus and PBR of KRas associating with the hydrophobic pocket of SmgGDS. No specific interactions between the G-domain of KRas and SmgGDS-558 were observed. This ensemble is interpreted using the in vivo mutational studies of SmgGDS-558 and fully processed KRas. Implications on the current understanding of their interactions are discussed.

3.1.1 Immunoprecipitation of SmgGDS-558 and fully processed KRas-GDP

HEK293T cells were co-transfected with a cDNA encoding HA-tagged wild-type or mutant SmgGDS-558, as well as a cDNA encoding myc-tagged KRas in either the wildtype (WT) form, the nucleotide-free form [KRas(T17N)], or the constitutively active (CA), GTP-bound form [KRas(G12V)]. After 24 hours, cell lysates were prepared and immunoprecipitated with HA antibody. The immunoprecipitates were immunoblotted using HA antibody (to detect HA-SmgGDS-558) and myc antibody (to detect co-precipitating myc-tagged KRas).

Essential residues on SmgGDS-558 that promote the stable interaction of fully processed KRas were identified via an immunoprecipitation assay (Figure 3.4). Mutant forms of SmgGDS tagged with hemagglutinin (HA) were allowed to form complexes with myc-KRas and analyzed by immunoprecitation as described in the Methods. Residues of SmgGDS were mutated based on previous studies implicating them in binding PBR-containing small GTPases (see Figure 3.3) [8]: A set of highly conserved residues within a binding groove of SmgGDS [8] which associate the G-domain of RhoA [7], a charge reversing set of mutations important for binding the PBR, and a third (W275A, N279A) testing the significance of the WIPSN sequence which was proposed to be essential for Rac1 binding [9]. I compared the interactions of the SmgGDS mutants with WT, NF, and CA forms of KRas which exhibited similar interactions with the SmgGDS mutants. This indicates that the nucleotide-state of KRas does not affect interactions with SmgGDS. The N338A mutation in SmgGDS-558 had the highest impact on the stability of a SmgGDS/KRas complex showing little detectable pull-down of KRas in HA immunoprecipitates. Of the acidic residue mutations, (D190K, E193K, E197K) and

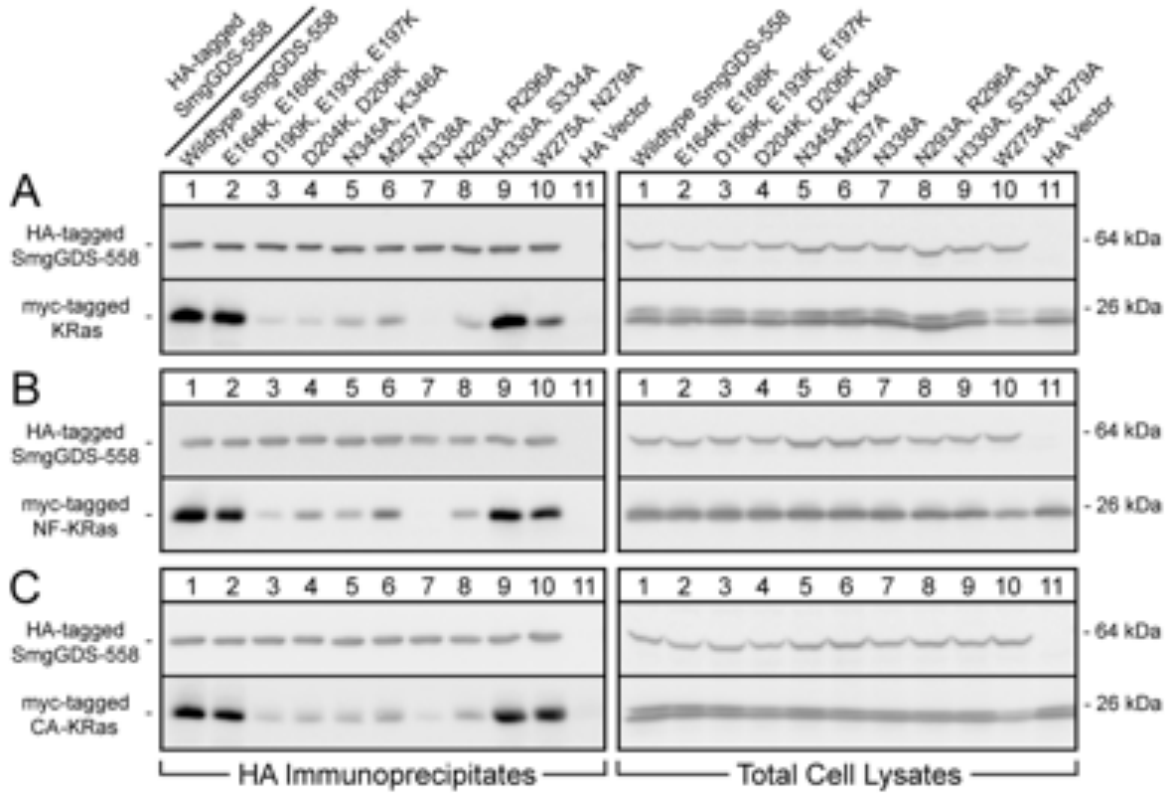

Figure 3.4: Disruption of KRas association by SmgGDS mutations. HA immunoprecipitates (*left*) of WT and mutant HA-tagged SmgGDS-558 show differential association of myc-tagged wildtype (*A*), nucleotide-free T17N mutant (*B*), and constitutively active G12V mutant (*C*) forms of KRas. Total cell lysates (*right*) show expressed SmgGDS-558 and KRas, which shows two bands corresponding to the unprenylated and prenylated forms, for each independent experiment. There is no significant loss of binding found in for mutations 2, 9 and 10. Mutations 3 through 8 show diminished binding to myc-tagged DN-KRas.

(D204K, D206K) were found to reduce binding of KRas whereas (E164K, E168K) had negligible effect. (N345A, K346A), (M247A), and (N293A, R296A) similarly reduced KRas co-precipitation. These results are leveraged in structural analyses of a SmgGDS-558 and KRas-FMe-GDP complex.

Protein production and purification

Purified SmgGDS isoforms were provided by the Carol L. Williams group (Medical College of Wisconsin; Milwaukee, WI). PET 28A-6X His-tagged SmgGDS-558 or SmgGDS-607 constructs were transformed into the BL21DE3 strain of *Escherichia coli*, and grown in the presence of kanamycin. Expression was induced after 2 hours using 1 mM IPTG and conducted for approximately 18 hours at 16 °C. Bacteria were collected by sedimentation and lysed in His-binding buffer with 5 mM imidazole (Qiagen). Lysates were passed through a French press (4 °C) 3 times and sedimented for 30 minutes at 20,000 g. The supernatant was passed through a 0.45-micron filter and purified on a nickel agarose column (Qiagen). The supernatant was allowed to bind with nickel agarose for 30 minutes at 4 °C with gentle agitation followed by centrifuging at 800 g, 4 °C. The column was washed with imidazole buffer at successive concentrations of 5 mM, 10 mM, and 20 mM before elution of His-tagged SmgGDS-558 or SmgGDS-607 by 250 mM imidazole buffer. Fractions were pooled and subjected to affinity chromatography using a liquid chromatography (FPLC) system to identify peak concentration elutions. Peak elutions were loaded onto an S-200 HR SEC in buffer (20 mM HEPES, 20 mM Tris, 100 mM NaCl, 5 mM $MgCl_2$, 1 μg/mL leupeptin, 1 μg/mL pepstatin, and 1 mM PMSF at pH 7.4), and collected in 200 drop fractions and assessed with Coomassie stain. Protein concentrations were determined by Bradford protein assays measuring absorbance of dye at 595 nm using a NanoDrop UV-Vis spectrophotometer (Thermo Fisher Scientific).

Purified fully processed KRas was provided by the Andrew Stephen group (Frederick National Lab for Cancer Research; Frederick, MD). A detailed description of the purification procedure for fully processed KRas is in [119].

3.1.2 Acknowledgments

Expression and purification of SmgGDS was performed by Ellen Lorimer and Bethany Unger from the Carol L. Williams group in the Pharmacology and Toxicology department at the Medical College of Wisconsin (Milwaukee, WI). Expression and purification of fully process KRas-GDP was provided by Andrew Stephen of the RAS Initiative at the Frederick National Laboratory for Cancer Research (Frederick, MA). Alex Grishaev

from the Institute for Bioscience and Biotechnology Research at University of Maryland (Rockville, MD) collected SAXS data and provided expertise on analysis.

3.2 Results and Discussion

SmgGDS-558 facilitates the transport of small GTPases to the plasma membrane [115]. Informed by detailed findings on the interaction of SmgGDS with RhoA [7, 8, 108], I focus here on the biophysical characterization of a KRas-FMe and SmgGDS complex and compare findings to known binding partners of SmgGDS and to interactions between KRas and PDEδ. Using SPR, the ability of SmgGDS isoforms to extract KRas-FMe-GDP from the plasma membrane was explored and the dissociation constant between SmgGDS isoforms and KRas-FMe-GDP was determined. Informed by these binding data and mutational studies, SAXS measurements were designed with samples of SmgGDS and KRas to characterize the stoichiometry and conformational ensembles of complexed SmgGDS-558 and KRas-FMe-GDP.

3.2.1 SmgGDS affects the membrane association of KRas-FMe-GDP

Membrane localization of KRas is crucial to its participation in signaling cascades. SPR experiments utilizing the stBLM system allow for a quantitative comparison of the ability of SmgGDS isoforms to affect membrane binding of KRas-FMe-GDP.

SPR was performed to characterize the equilibrium binding of KRas-FMe-GDP to anionic stBLMs of composition 7:3. Following bilayer formation, a baseline SPR response level was recorded and increasing concentrations of KRas-FMe-GDP were added to the system. Response levels at equilibrium were recorded. The SPR sensorgram is shown in Figure 3.5. The dissociation constant K_{d} was found to be $0.74 \pm 0.04 \mu$M, in agreement with previous measurements [34, 119–121].

To investigate the ability of SmgGDS isoforms to interact with membrane-bound KRas, 2 μM KRas-FMe-GDP was incubated on freshly prepared stBLMs with a lipid composition of 7:3 POPC:POPS. To ensure any observed binding events in SPR sensorgrams could only be due to KRas, experimental buffer conditions were determined in which SmgGDS isoforms did not associate model membranes (Figure 3.6). The equilibrium SPR response after incubation of KRas was reproduced for all experiments, varying by no more than 15% in a given experiment. This value was defined as R_o. For comparative purposes, SPR sensorgrams are normalized to R_o. The system was then subjected to one of three conditions: remove half of the sample volume and replace with buffer, remove half of the sample volume and replace with solution containing 2 μM SmgGDS-558, and similarly with 2 μM SmgGDS-607. In all cases, the free concentration

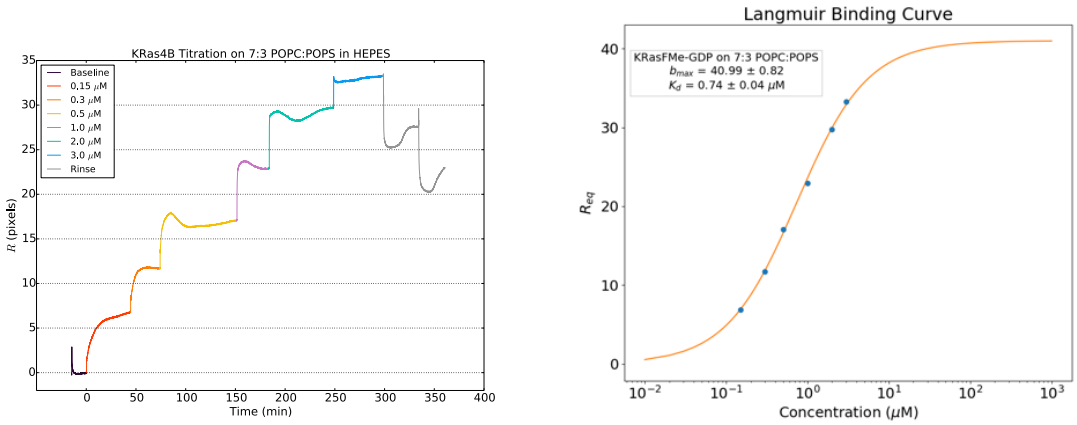

Figure 3.5: Langmuir binding of KRas-FMe-GDP to 7:3 POPC:POPS stBLMs. *Left*: Equilibrium binding of sequential additions of KRas to the stBLM system were measured. Data at each concentration were collected until the response reached an equilibrium value after which the next concentration was introduced. *Right*: A Langmuir binding isotherm was fit to six equilibrium response values at increasing concentrations.

of KRas in the sample is 1 μM after initial buffer removal. Therefore, any difference in response from introducing SmgGDS isoforms compared to a buffer rinse will be entirely due to SmgGDS. Buffer conditions were optimized to eliminate interactions between SmgGDS isoforms and neat stBLMs with a composition of 20 mM HEPES, 100 mM NaCl, 5 mM MgCl2, 1mM TCEP at pH 7.4.

Figure 3.7 shows sensorgrams of the normalized response for each of the three cases. A buffer rinse caused the response to fall to $(0.86 \pm 0.02)R_o$. Introducing 2 μM SmgGDS-558 yielded a substantial drop in signal to $(0.45 \pm 0.02)R_o$ while SmgGDS-607 decreased the signal to $(0.74 \pm 0.01)R_o$ immediately after the exchange. Both SmgGDS variants caused a larger signal drop than a buffer rinse indicating both SmgGDS-558 and SmgGDS-607 affect membrane localization of KRas. SmgGDS-558 causes a removal of a substantially larger fraction than SmgGDS-607 likely due to its preferential binding to prenylated small GTPases. It is important to note that this study cannot differentiate between direct removal of KRas by SmgGDS or removal due to depleting free KRas in solution. Comparing the response values to Figure 3.5, a buffer rinse drops the response level equivalent to 1.2 μM KRas. 2μM SmgGDS-558 and SmgGDS-607 lead to response levels equivalent to approximately 0.4 and 0.8 μM KRas respectively.

Although the fraction of KRas removed within the first seconds of SmgGDS-607 being added to the system was reliably reproduced in three independent experiments, the response of the system following this was difficult to reproduce. Bilayer quality likely plays a important role in this. Figure 3.8 shows two independent experiments with

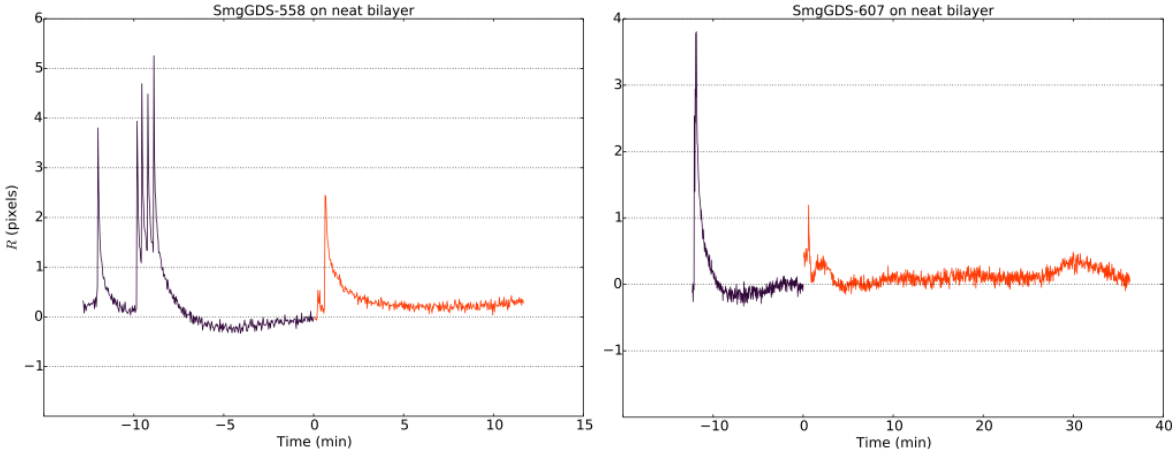

Figure 3.6: SmgGDS does not associate neat anionic stBLMs.

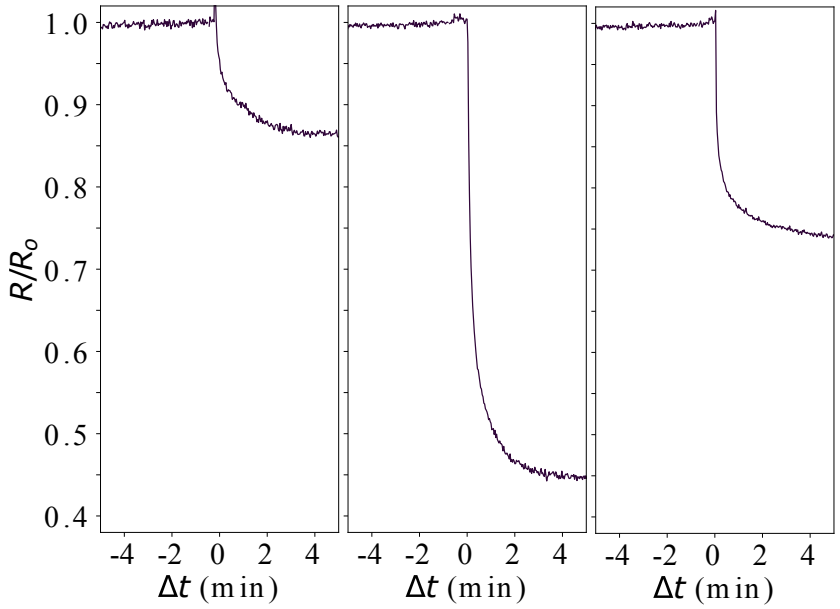

Figure 3.7: Differential membrane association loss of KRas-FMe-GDP. Three exemplary SPR sensorgrams are shown. R/R_o is the SPR response normalized to the equilibrium level of a solution concentration of 2 μM KRas. The x-axis is the time from when KRas was initially introduced to the stBLM. *Left:* the cell is rinsed with buffer a number of times. Only the first rinse following KRas incubation is used in subsequent discussions. *Middle:* 2 μM SmgGDS-558 is introduced to the system. *Right:* 2 μM SmgGDS-607 is added to the system.

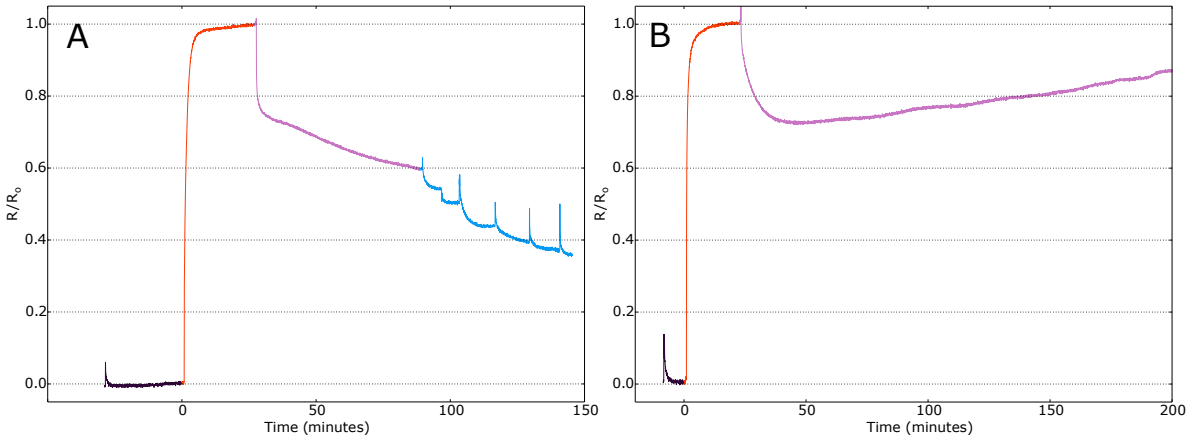

Figure 3.8: Independent SPR measurements of KRas membrane association with SmgGDS-607. SmgGDS-607 was introduced to stBLM samples incubated with KRas-FMe-GDP. Baseline data for a neat bilayer is in black. KRas incubation response is shown in red and the data in purple are after adding SmgGDS-607. The response decreased quickly upon introducing SmgGDS-607 for both experiments while differing over longer timescales. Blue data indicate buffer rinsing of the system.

differing long timescale response. Neat bilayer quality was assessed before recording SPR response and the measured R_{def} for the neat bilayer used in Figure 3.8A was approximately 0.8 MΩ while R_{def} for Figure 3.8B was an order of magnitude lower. Following a series of buffer rinses after SmgGDS-607 data collection, both bilayers had comparably low R_{def} measuring in the kΩ range. It is possible a high density of defects do not substantially affect KRas association to the membrane but could result in non-specific aggregation of SmgGDS-607 over time. It is difficult to determine the origin of the long scale dissociation observed in Figure 3.8A as either from slow solubilization of membrane-bound KRas by SmgGDS-607 or by the deterioration of the stBLM over time.

For experiments measuring the effect of SmgGDS-558 on KRas membrane-association, two sudden decreases in response were observed (see Figure 3.9A). Following the initial drop after incubating KRas, a second, shallow, decrease was observed in independent repeat measurements of this system. The smaller response decrease could be due to a lagging fraction of membrane-bound KRas dissociating from the membrane. Comparing the data in Figures 3.9B and 3.5 indicate the Langmuir binding isotherm does not accurately describe the bound fraction of KRas following dilution.

The dissociation constant of KRas binding SmgGDS-558 was estimated from the SPR data in comparison to Langmuir binding isotherms of KRas titrations on model membranes of identical composition [34]. An assumption is made that solution concentrations have an uncertainty of ±10%. When introducing 2 ± 0.2 μM SmgGDS-558 to

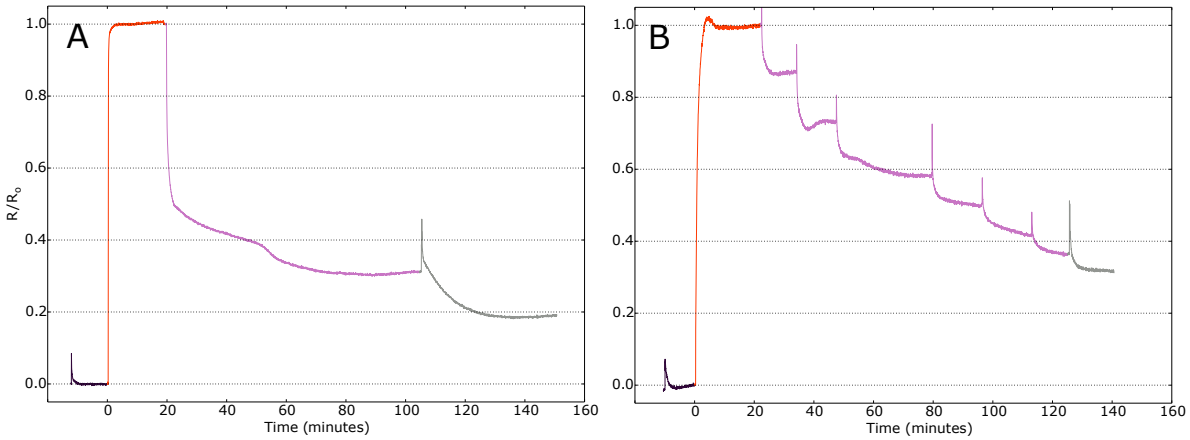

Figure 3.9: SPR sensorgrams of SmgGDS-558 solubilizing membrane-bound KRas and of rinsing KRas from an stBLM. *A:* SPR response data is shown for: the baseline response of the neat bilayer (black), incubating 2 μM KRas-FMe-GDP (red), adding SmgGDS-558 (purple), and a final buffer rinse (gray). The response decrease observed at approximately 50 minutes was independently reproduced in repeat experiments. *B:* Successive two-fold dilutions (purple) were performed on an stBLM incubated with 2 μM KRas-FMe-GDP with a final four-fold dilution (gray).

the system, the normalized response, R/R_o, drops to 0.45, equivalent to a solution concentration of 0.41 $\pm$ 0.14 μM on the Langmuir binding isotherm. Under the assumption that solubilized KRas binds SmgGDS-558, this indicates 0.59 $\pm$ 0.14 μM releases and forms a complex with SmgGDS-558. The dissociation constant for KRas-FMe-GDP binding SmgGDS-558 was calculated to be 0.96 $\pm$ 0.14 μM from

$$K_{\mathrm{d}} = \frac{([A]_0 - [AB])([B]_0 - [AB])}{[AB]}$$

where $([A]_0 - [AB])$ and $([B]_0 - [AB])$ are the concentrations of free SmgGDS-558 and KRas in solution, respectively, and $[AB]$ is the concentration of bound complex. In practice, diluting solution concentration of KRas several orders of magnitude leaves a lagging membrane bound population that slowly dissociates as evident in Figure 3.9B. Therefore, 0.59 $\pm$ 0.14 μM represents the upper bound on the concentration of bound KRas, and, correspondingly, 0.96 $\pm$ 0.14 μM represents an upper bound on the dissociation constant between SmgGDS-558 and KRas-FMe-GDP. This calculation was not possible for data of SmgGDS-607 interactions with KRas. The inferred solution concentration of KRas to produce the normalized response, $R/R_o = 0.75$, is 1.10 $\pm$ 0.14 μM, above the known experimental concentration. Calculating the bound concentration of SmgGDS-607 yields an unphysical, negative, value. If we assume the actual value of the concentration of KRas is at the lower bound of uncertainty, then 0.04 μM KRas

forms a complex with SmgGDS-607 (0.96 μM remains free) and the dissociation constant is 47 $\pm$ 10 μM. To obtain a more accurate estimation of the dissociation constant of binding SmgGDS-607, a redesign of the experiment is required to properly account for the lagging fraction of bound KRas after depleting the solution concentration

The change in free energy for formation of a SmgGDS-558 and KRas-FMe-GDP complex, using the upper bound on K_{d}, is $\Delta G^{\mathrm{o}}_{558/\mathrm{KRas}} = -44.3 \pm 0.4$ kJ/mol. For comparison, the free energy of KRas binding anionic stBLMs, -44.4 $\pm$ 0.8 kJ/mol. Biological membranes likely contain fewer binding sites for KRas with higher competition for those sites. Therefore, the change in free energy of KRas binding the plasma membrane could be lower. Additionally, while these energetics suggest KRas could spontaneously release the membrane and bind SmgGDS-558 without the need for an intermediary catalyst, it is not clear what energetic barrier is required to overcome for this process. SmgGDS-558 is speculated to associate fully processed KRas at ER membranes [6]; these experiments use stBLMs which contain a fraction of phosphatidylserine lipid headgroups modeling that of the plasma membrane [17]. Therefore, lipid bilayers modeling the composition of ER membranes would be required to make more substantial claims regarding the ability of SmgGDS-558 to solubilize KRas from ER membranes.

Studies of the effect of SmgGDS on KRas association to anionic bilayers presented here included 30 mol% negatively charged lipids. The pH near the ER is nearly neutral (7.1) and, similar to the experimental condition used. Lipid compositions of cellular membranes are shown in Figure 3.10. ER membranes are composed of roughly 45 % PC, 22 % PE, 23 % PI, 5 % PS, and 5 % remaining lipids [10]. 70 mol% PC lipid content in stBLMs could be a sufficient amount of zwitterionic headgroups to model the proportion of neutral lipids in ER membranes. Modeling charged components of ER membranes is a more complex problem because of elevated levels of PI headgroups whose charge depends on their phosphorylation state. PI headgroups contain an inositol ring, which can be phosphorphylated in the 3, 4, and 5 positions resulting in seven unique states [122, 123]. Fluorescence studies of KRas binding to lipid nanodiscs found the binding affinity of KRas to model membranes was highly sensitive to the presence of PIP_2 [124]. The dissociation constant of binding to lipid nanodiscs with 2.5 mol% up to 10 mol% PIP_2 was observed to be between half to an order of magnitude less than that of 30 mol% PS lipid. Due to the dependence of KRas binding to model membranes on PIP content and that the ER membrane PI lipid composition is not well known, obtaining evidence for SmgGDS-558 associating KRas at ER membranes via binding studies at membranes modeling the ER is not a trivial undertaking.

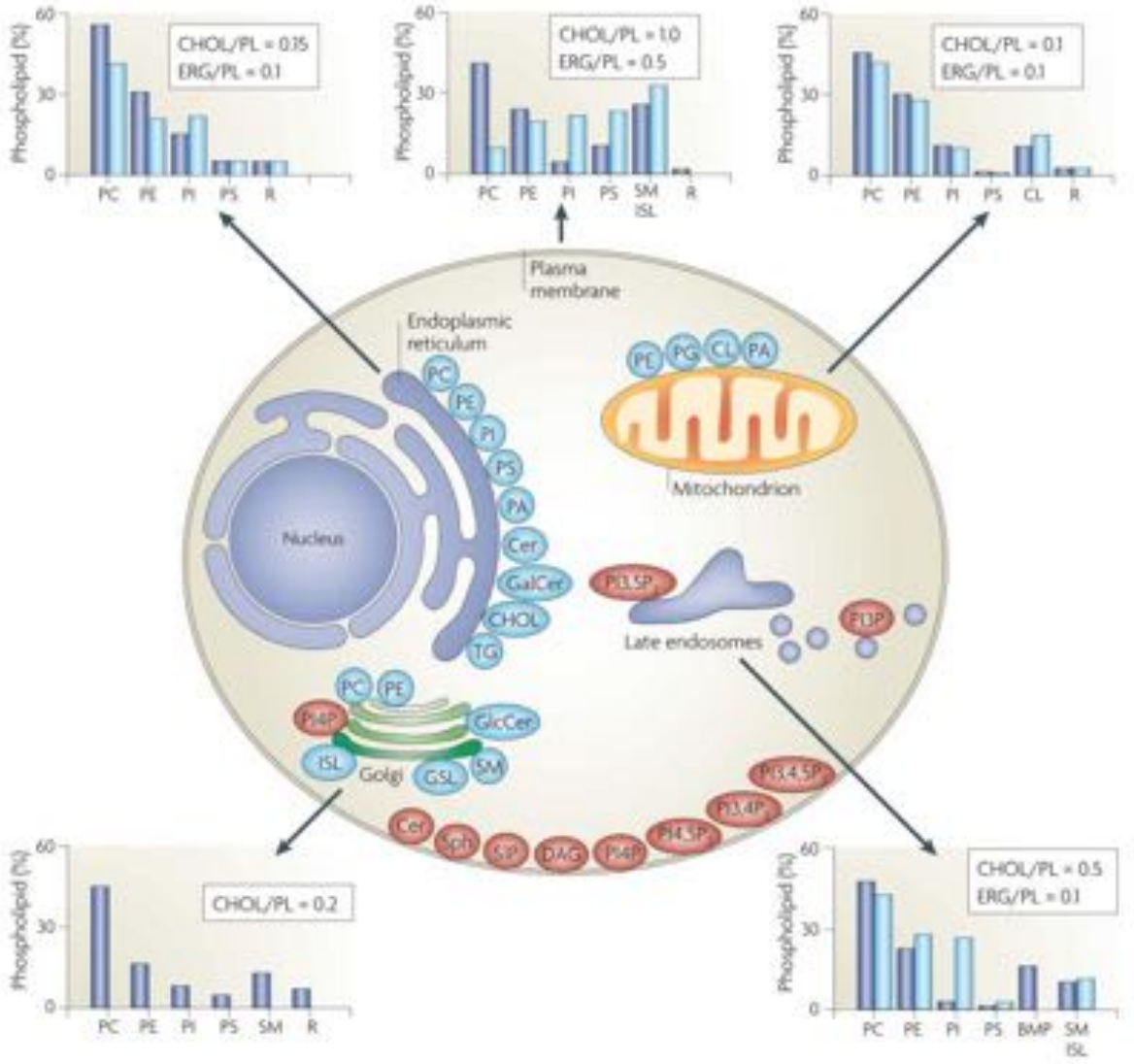

Figure 3.10: Biological membrane compositions and lipid synthesis sites. Figure adapted from [10]. Plots are shown of the membrane composition of various subcellular components in mammals (blue) and yeast (light blue). Listed components within the endoplasmic reticulum and plasma membrane include phosphatidylcholine (PC), phosphatidylethanolamine (PE), phosphatidylinositol (PI), phosphatidylserine (PS), sphingomyelin (SM), inositol sphingolipid (ISL), and remaining lipid species (R). The ratio of sterol to phospholipid content is shown for each plot: cholesterol (CHOL) for mammal cells and ergosterol (ERG) for yeast cells. The illustration of the cell shows the synthesis site for various phospholipid (blue) and lipids involved in organelle recognition pathways (red).

3.2.2 SAXS measurements of SmgGDS and KRas

SmgGDS has been identified as a major regulator in the prenylation pathway of small GTPases and their subsequent trafficking to signal transduction sites [106,109,115,125,126].

Five sets of SAXS intensity profiles were collected from samples of SmgGDS-558, SmgGDS-607, KRas-FMe-GDP, and mixed solutions of each SmgGDS isoform with KRas-FMe-GDP in a 1:1 molar ratio(Figure 3.11). Each protein was dialyzed with 500 mL buffer with 20 mM Tris-HCl, 150 mM NaCl, 5mM EDTA, 10 mM $MgCl_2$, and 10 mM DTT at pH 7.5. In addition to protein samples, scattering from pure buffer was collected for subtraction. Two detector configurations corresponding to SAXS and WAXS were used to collect data for each sample and merged (depicted in Figure 3.12) allowing data collection in a q-range of 0.006 to 0.4 $Å^{-1}$.

Data were measured from SmgGDS variants at 1.0 mg/mL and 0.5 mg/mL SmgGDS-558, and 2.0 mg/ml SmgGDS-607 sample concentrations. Additionally, mixed samples of SmgGDS and KRas at 1.4 mg/mL total concentrations including two-fold dilutions were subject to scattering in 1:1 molar ratios. Guinier analysis of these data indicate non-specific aggregation at higher concentrations (see Figures 3.13 and 3.14). A dependence of Guinier R_g on protein concentration was observed for SmgGDS-558, SmgGDS-558 and KRas mixtures, and SmgGDS-607 and KRas mixtures which indicate non-specific aggregation within the samples. As a result, SAXS data at low concentration was merged with WAXS data at higher concentrations to minimize scattering contributions from aggregation while leveraging higher signal-to-noise at wider angles. PRIMUS [11] performs an automated least-squares scaling routine in the overlapping region (approximately 0.03 to 0.08 $Å^{-1}$).

SmgGDS data from the WAXS detector configuration exhibited radiation damage after continuous exposure to radiation. Collected scattering data was averaged over multiple data frames collected over the entire q-range and the final three frames out of a total of 16 were rejected due to deviations at low angles. Reducing agents in the working buffer, DTT and TCEP, were tested up to 10 mM concentrations. DTT was far more effective in limiting damage however did not entirely resolve the issue. Visual inspection of SmgGDS in VMD [13] reveals a number of surface cysteines which have the potential to undergo reduction reactions when exposed to radiation. From examining the X-ray crystallography structure and homology model of SmgGDS-558, 4 to 5 solvent-exposed cysteine groups were identified. The homology model of SmgGDS-607 [127] contained 4 potentially vulnerable cysteine groups. Passivating mutations of these residues could ameliorate sensitivity of SmgGDS to prolonged radiation exposure.

Table 3.1 contains structural parameters obtained from Guinier and molecular weight (MW) estimation of the scattering data. Intensity at zero-angle and radius of gyration (R_g) were calculated with Guinier analysis. To estimate MW, a Bayesian inference

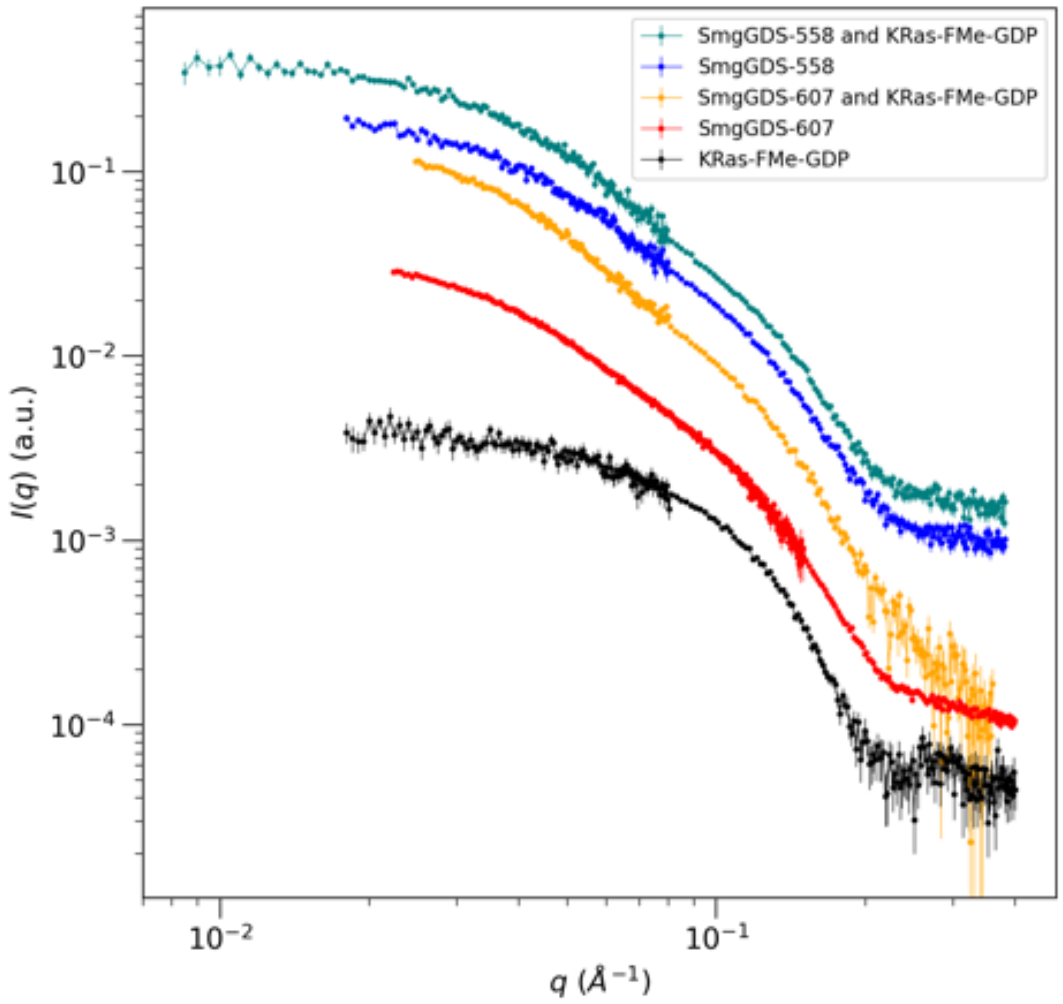

Figure 3.11: SAXS curves of SmgGDS, KRas-FMe-GDP, and mixed samples of SmgGDS isoforms with KRas in a 1:1 molar ratio. Solution scattering log-log data is shown after merging measured intensities from SAXS and WAXS detector configurations up to $q = 0.4$ Å^{-1}. The scattering profiles are artificially scaled for visual clarity. Scattering from mixed samples of SmgGDS and KRas displayed increased intensities for, roughly, $q < 0.08$Å^{-1} relative to pure SmgGDS solutions. Low-angle data for each sample were individually trimmed to remove data with increased scattering from non-specific aggregation based on Guinier analysis (see Figures 3.13 and 3.14). Notably, Guinier fits of SmgGDS-558 and KRas mixture data was uniquely well-behaved when extending the fit range to the lowest q.

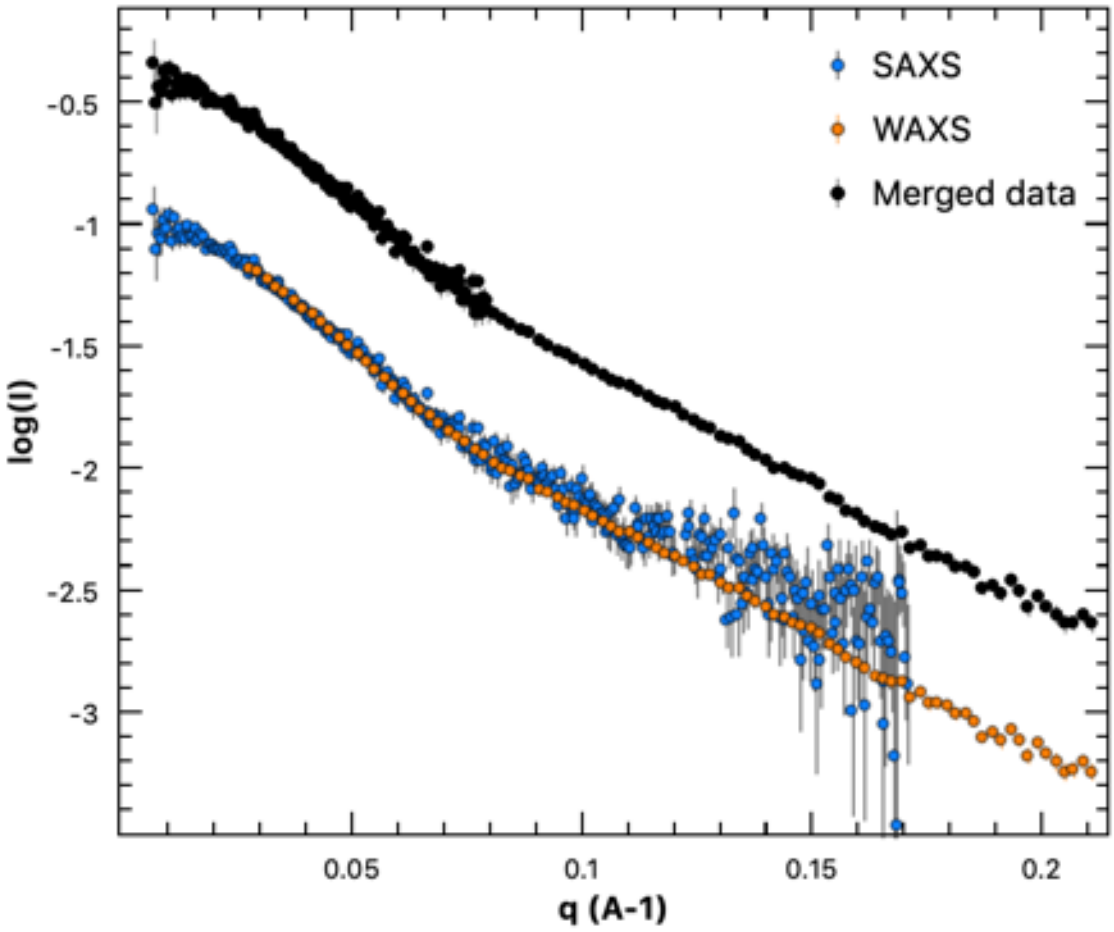

Figure 3.12: Illustration of merging scattering data from SAXS and WAXS detector configurations. Scattering data of SmgGDS-558 and KRas mixtures at 0.7 mg/mL (blue) and 1.4 mg/mL (orange) concentrations are shown. The merged scattering profile (black) is artificially scaled for visual clarity. Merging is performed in PRIMUS [11] after determining an overlap region (approximately 0.03 to 0.08 $Å^{-1}$) where the data are consistent and scaling SAXS intensites to the WAXS data. The SAXS data at high q is above WAXS due to poor signal-to-noise due to the lower concentration.

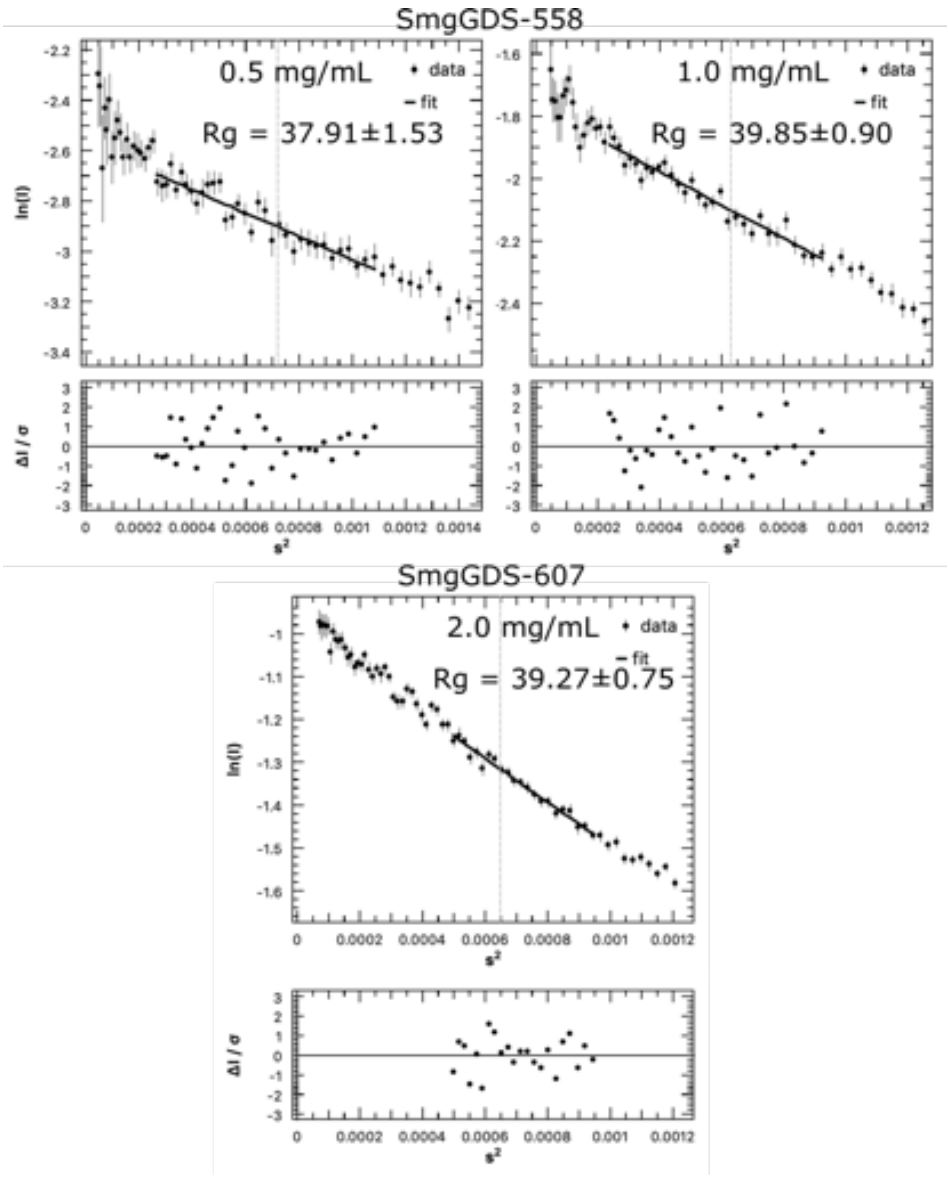

Figure 3.13: Guinier fits of SmgGDS solution scattering data. Guinier fitting was performed with the PRIMUS application [11]. Reported R_g values are in units of Å. The upper bound on the fitted range was initially determined automatically by PRIMUS before subsequently decreasing it to $q_{max}R_g \approx 1.2$. An upper limit of $q_{max}R_g = 1.3$ in Guinier analysis is for ideally spherical structures and SmgGDS is predicted to an elongated helical structure (see Figure 3.3). The lower bound was determined by incrementally decreasing $q_{min}R_g$ while ensuring the Guinier R_g remained constant. For example, extending the fitted range for 0.5 mg/mL SmgGDS-558 data to include all low-angle data increases the Guinier R_g to 41.02 ± 1.06 Å.

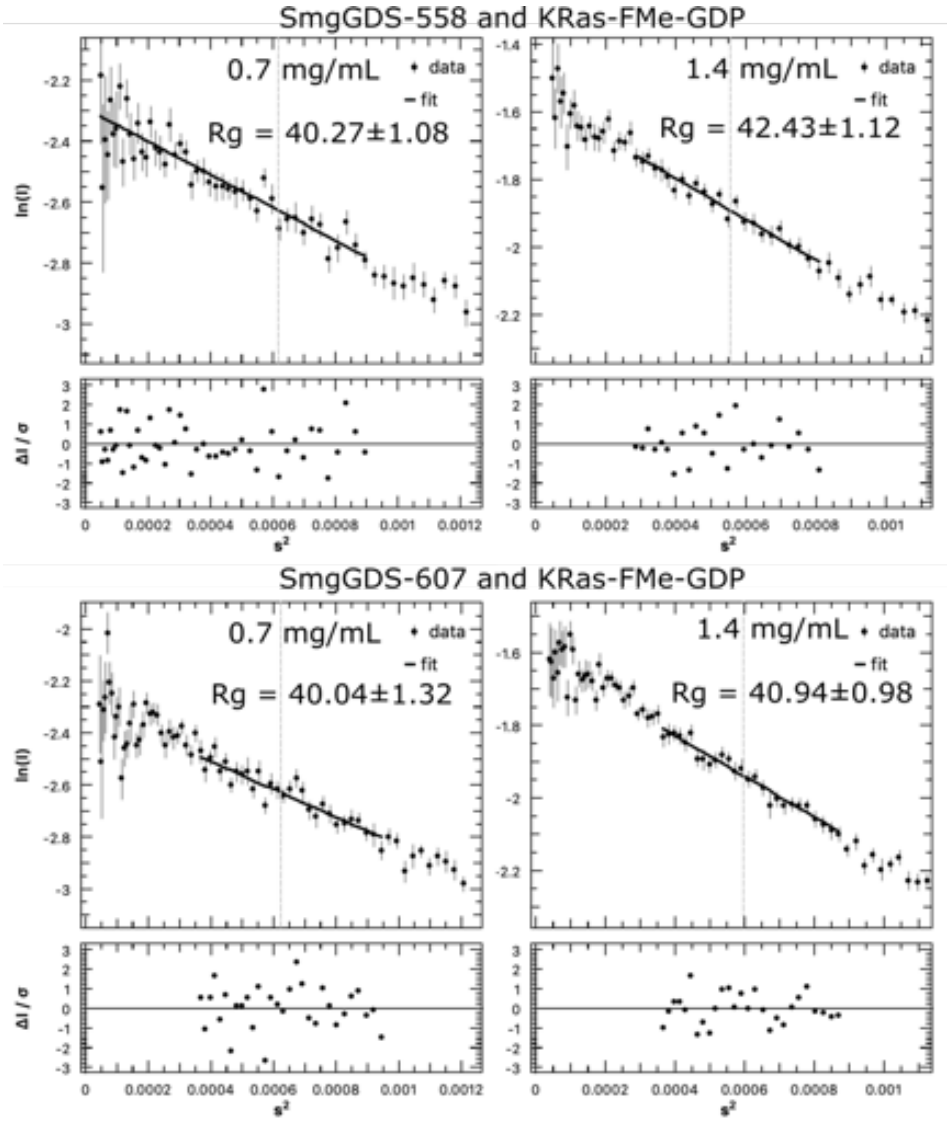

Figure 3.14: Guinier fits of SmgGDS and KRas scattering data. Reported R_g values are in units of Å. Bounds on the fitted range were determined as previously described (see Figure 3.13)

method was utilized taking into account calculations using the Porod invariant, volume of correlation, and the Size&Shape method which infers MW based on known values for proteins of similar size and shape. MWs from each method are shown for comparison. Bayesian estimation was chosen due to its reported higher accuracy compared to any single determination method regardless of signal-to-noise level and particle shape. The MW of KRas was estimated to be 18.1 kDa, about 15% less than the expected value, 21.4 kDa [119]. MW estimation of SmgGDS-558 scattering data is consistent with monomeric species to within 5% of its expected value. For samples containing a 1:1 mixed solution of SmgGDS-558 and KRas, the apparent MW is 74.3 kDa which is 10% smaller than the expected value for a 1:1 SmgGDS-558 and KRas complex, 82.6 kDa. In addition to an increase in MW, R_g for mixed solutions of SmgGDS-558 and KRas was found to be 40.02 ± 1.20 Å compared to 37.91 ± 1.53 Å for SmgGDS-558. Mixed samples including SmgGDS-558 form structures that are comparatively more extended than samples containing SmgGDS-558 alone. Additionally, the apparent MW is larger than that for solely SmgGDS-558. The increase in MW and R_g, and absence of aggregation evidence in Guinier and $P(r)$ analysis, is strong evidence for SmgGDS-558 and KRas forming a 1:1 complex. In contrast, SmgGDS-607 data yield a R_g of 39.15 ± 0.84 Å and MW of 68.8 kDa and increases to 42.49 ± 0.58 Å and 97.5 kDa. The change in R_g is approximately 50% larger compared to samples with SmgGDS-558 and the change in MW is more than 100% larger. A stable 1:1 complex of SmgGDS-607 and KRas-FMe-GDP would be expected to report R_g similar or lesser in magnitude than the SmgGDS-558 and KRas-FMe-GDP sample.

Pairwise distance distribution functions, $P(r)$, for each sample were determined and is displayed in Figures 3.15 and 3.16. The shape of the distance distribution function for KRas is approximately symmetric about half of the maximum dimension and consistent with a spherically shaped particle. SmgGDS $P(r)$ functions contain peaks at approximately 25 Å distances and linearly decay for increasing pairwise distances. Mixed samples display $P(r)$ distributions with notably wider peaks starting at approximately 25 Å until 50 Å. This additional density is likely due to the association of KRas to SmgGDS. A tail in the distribution density for mixtures of SmgGDS-607 and KRas contain a tail at high distances that does not follow the linear decay of the distribution. Cutting this tail short leads to high residuals for the lowest q data indicating non-specific aggregation in the sample. Analysis of KRas-FMe-GDP data presented challenges not found in SmgGDS data sets. Although the Guinier analysis was generally well-behaved when truncating low-q data, the pairwise distance distribution, $P(r)$ calculations from fitting the full scattering curve poorly described intensities for $q < 0.8\text{Å}^{-1}$. Additionally, R_g from the $P(r)$ distribution did not agree with the R_g from Guinier analysis except for when setting D_{max} to approximately 80 Å, nearly double than that shown in 3.16. There is likely a significant scattering contribution from non-specific aggregation in KRas-FMe

Table 3.1: Physical parameters calculated from SAXS data. Guinier analysis was used to approximate forward scattering intensity and radius of gyration for samples of KRas-FMe-GDP and SmgGDS. Molecular weights were estimated using a Bayesian inference method based on four concentration independent methods and are reported with 90% confidence intervals. The expected values for MW for mixed solutions were calculated assuming 1:1 binding.

	KRas-FMe-GDP	SmgGDS-558		SmgGDS-607	
KRas-FMe-GDP	+	−	+	−	+
Guinier $I(0)$	0.02 ± 0.0001	0.077 ± 0.0018	0.10 ± 0.0017	0.37 ± 0.0059	0.106 ± 0.00120
Guinier R_g (Å)	19.26 ± 0.22	37.91 ± 1.53	40.02 ± 1.20	39.15 ± 0.84	42.49 ± 0.58
qR_g range	0.53 to 1.19	0.62 to 1.19	0.28 to 1.18	0.88 to 1.19	1.02 to 1.20
Porod MW (kDa)	14.9	58.9	72.0	66.3	91.0
MoW MW (kDa)	18.7	64.1	78.4	74.9	109.8
Volume of Correlation MW (kDa)	18.2	56.7	71.9	65.0	97.0
Size&Shape MW (kDa)	18.8	75.8	89.0	75.2	108.8
Bayesian inference MW (kDa)	18.1 (17.1, 19.0)	59.5 (57.5, 63.1)	74.3 (69.7, 79.6)	68.8 (64.7, 73.4)	97.5 (92.7, 111.3)
Expected MW (kDa)	21.6	61.0	82.6	66.3	87.9

samples over a q-range spanning the Guinier region such that it is only detectable when examining the residuals from $P(r)$ fits.

By merging SAXS and WAXS data from differing concentrations, aggregation contributions were minimized at low angle data while the signal-to-noise was increased for wider angles. Although aggregation was not completely absent, the Guinier analysis, distance distribution functions, and MW estimation suggest KRas, SmgGDS-558, and SmgGDS-607 are monomeric in their respective solutions. SmgGDS-558 and KRas-FMe likely form a 1:1 complex in solution while SmgGDS-607 and KRas bound constructs are less well-defined potentially due to the absence of a hydrophobic pocket in SmgGDS-607 for the farnesyl group of KRas. To uncover more specific structural information, modeling of SmgGDS with and without KRas was performed, particularly to determine if the G-domain had specific interactions with SmgGDS.

3.2.3 Molecular dynamics simulation of SmgGDS-558 in solvent

Molecular dynamics simulations of a full-length homology model of SmgGDS-558 in solvent were performed with the GROMACS [90] simulation package for 2000 ns. The

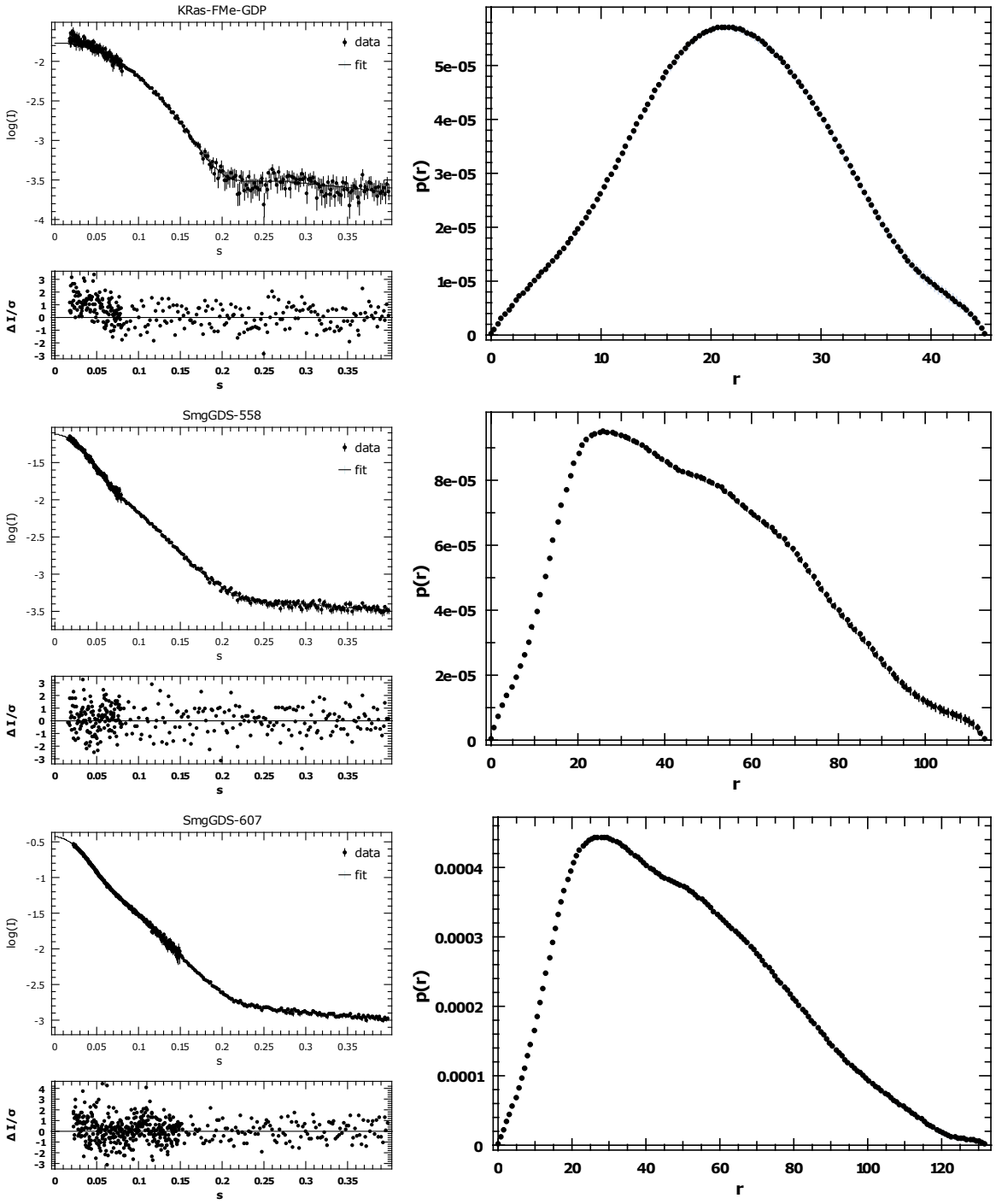

Figure 3.15: Distance distribution functions calculated from SAXS data of KRas-FMe-GDP and SmgGDS samples. The GNOM program was used to perform calculations [12]. The entire intensity profile of each set of data is used to calculate the distance distribution function $P(R)$ using a regularized indirect Fourier transform method. The maximum particle dimension $D_{\max}$ is specified by the user. $D_{\max}$ was chosen manually within a range of values which yielded stable distributions. The lowest value was chosen such that R_g was in agreement with Guinier analysis.

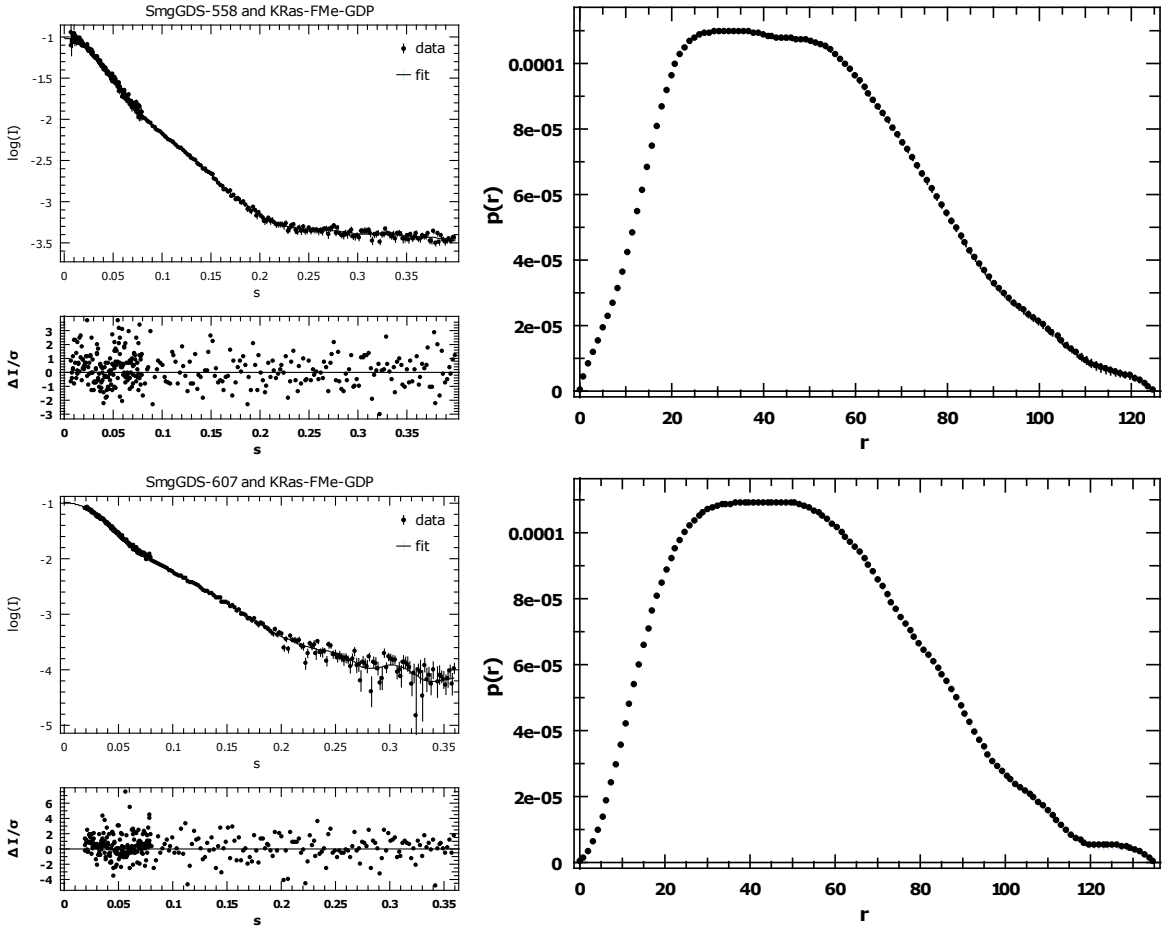

Figure 3.16: Distance distribution functions calculated for SmgGDS and KRas mixtures. The entire intensity profile of each set of data is used to calculate the distance distribution function $P(r)$ using a regularized indirect Fourier transform method. The maximum particle dimension $D_{\max}$ is specified by the user. $D_{\max}$ was chosen manually within a range of values which yielded stable distributions. The lowest value was chosen such that R_g was in agreement with Guinier analysis.

homology model was provided by the Williams group (Medical College of Wisconsin; Milwaukee, WI) which has been used in previous work [127]. Compared to the SmgGDS-558 species used in SAXS and SPR studies, the structure used in simulations contained an additional alanine at the N-terminal 2 position. The Sondek group (University of North Carolina School of Medicine; Chapel Hill, NC) produced work on SmgGDS-559 and originally produced the homology model utilized in this study. The additional alanine in SmgGDS-559 is generally considered to negligibly alter the structure and function of the shorter variant of SmgGDS and will therefore be referred to as SmgGDS-558 in subsequent discussion.

Molecular dynamics simulation of SmgGDS-558 were performed in aqueous solvent including 150 mM excess NaCl using the GROMACS 2018 package [90] with a step size of 100 ps. Input files were generated via the CHARMM-GUI [91, 92, 128]. The PDB file of the SmgGDS-558 homology was uploaded to the service and no additional modifications performed. A rectangular system shape was specified with equal side lengths that exceeded the largest dimension of the starting structure by 40 Å to ensure fluctuations in the structure of SmgGDS-558 remain within the solvent box. After energy minimization of the system using the CHARMM-GUI [92, 128] protocol, the system was simulated for 10 ns without restraint to relax the system before production runs. The CHARMM36m force field [129] was used for calculations of the protein while the CHARMM-modified TIP3P model was used for water [129, 130]. The LINCS algorithm constrained hydrogen covalent bond lengths [131]. Lennard-Jones interactions were subject to the Verlot cut-off scheme for neighbor searching with smooth switching of forces to zero between 1.0 nm and 1.2 nm. Coulomb interactions were determined using fast, smooth particle-mesh Ewald (SPME) electrostatics. A Nosé-Hoover thermostat with a coupling time constant of 1 ps was utilized at 303.15 K and the NpT ensemble was implemented by semi-isotropic coupling to a Parrinello-Rahman barostat at 1 bar with 4.5×10^{-6} bar^{-1} compressibilities [90]. Simulated structures were saved every 0.1 ns to save computation time in modeling SAXS intensity profiles to compare to experiment data.

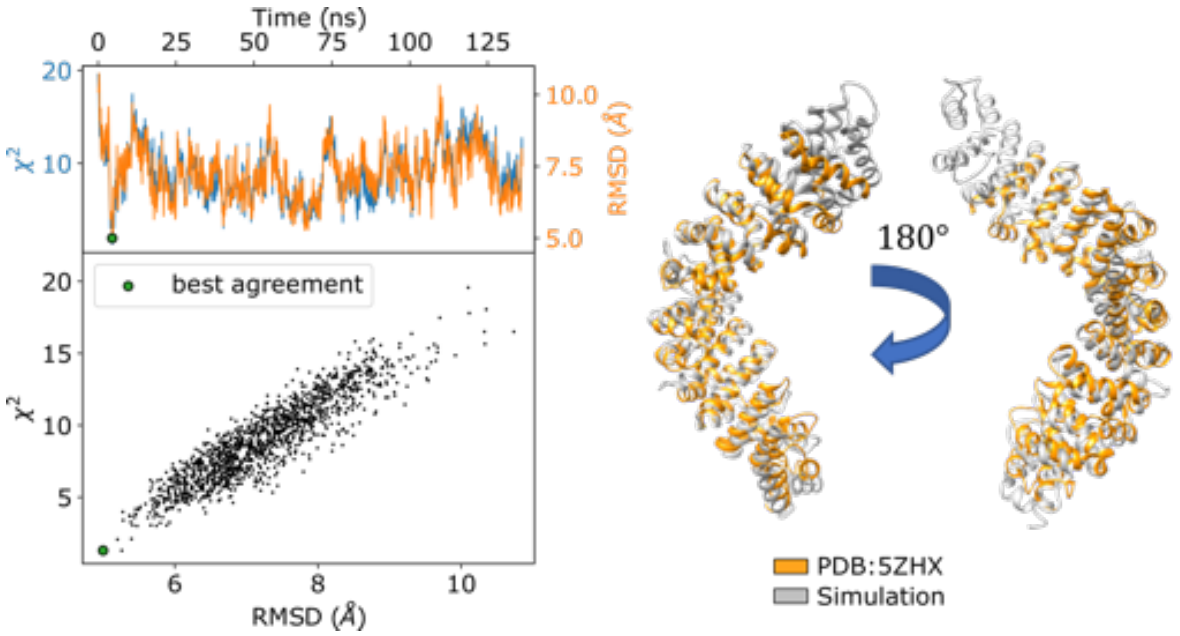

Figure 3.17: MD simulation of SmgGDS-558 yields a structure in agreement with the SAXS results and that of SmgGDS-558 in complex with RhoA (PDB:5ZHX) [7]. *Left:* Goodness-of-fit, χ^2, of the simulation-derived SAXS intensities to the experiment vs. pairwise RMSD to the partial structure of SmgGDS-558 in PDB:5ZHX for each simulation frame. *Right:* Simulated full-length structure of SmgGDS-558 with the best agreement to the SAXS results (gray) and partial structure of SmgGDS-558 from PDB:5ZHX (orange).

Theoretical scattering curves were calculated for structures every 0.1 ns with CRYSOL 3.0 and compared to the SAXS data of SmgGDS-558. In parallel, the root-mean-squared deviation (RMSD) was calculated between each simulated structure and the partial atomistic structure of SmgGDS-558 bound to RhoA [7]. Following equilibration, production steps began with the structure of SmgGDS in an elongated conformation (see Figure 3.18). These initial conformations were poor descriptions of the solution scattering profile of SmgGDS. Within 10 ns of the start, an increasing bend at the midpoint of the body led to both a decrease in χ^2 and decrease in RMSD from the atomistic structure in PDB:5ZHX. The structure relaxed after the bend angle reached an extremum but does not return to the elongated configuration seen in Figure 3.18. A strong correlation was found between χ^2 fits to the SAXS data and pairwise RMSD compared with the partial crystal structure of SmgGDS-558 in complex with RhoA (Figure 3.17). This suggests that the configuration of SmgGDS in PDB:5ZHX is consistent with the measured solution scattering profile from full-length SmgGDS-558. It is likely that modeling truncated residues in the partial crystal structure of SmgGDS-558 could produce a theoretical

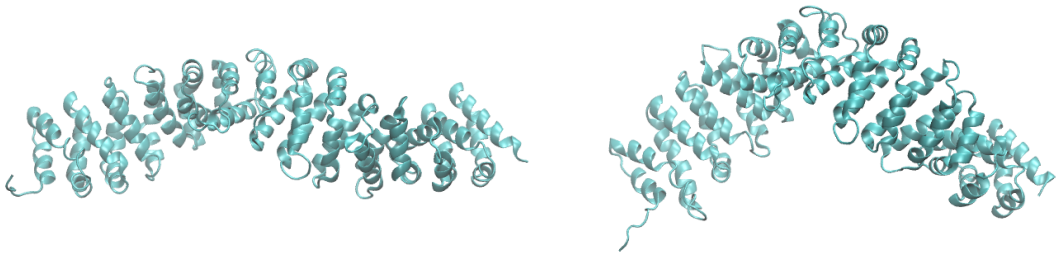

Figure 3.18: Conformations from simulating a SmgGDS-558 homology model. Production simulation steps began with SmgGDS-558 as shown on the left. Succeeding steps of the simulation quickly led to the conformation shown at the right, which simultaneously described solution scattering data and matched the truncated crystallized structured in PDB:5ZHX.

scattering profile in good agreement with experimental data. The structure with χ^2 of 1.34 and least 5.0 Å pairwise RMSD was used for modeling of a SmgGDS-558 / KRas complex.

3.2.4 MC simulation

SmgGDS has been observed to interact with small GTPases through an electronegative patch, a G-domain-binding groove which is highly conserved across species, and a hydrophobic pocket (in the case of SmgGDS-558) [6–8]. Additionally, SmgGDS has thus far been shown to activate RhoA and RhoC [8]. The residues which are critical in promoting GTP/GDP exchange in these small GTPases could still facilitate interactions with other Ras proteins. Sets of residues in SmgGDS implicated in activation of RhoA and binding of Rac1 were examined in MC simulations of a SmgGDS-558 and KRas-FMe complex to determine their role in binding KRas.

A Monte-Carlo simulation of KRas-FMe-GDP bound to SmgGDS-558 was performed using the SASSIE-WEB service [69] in a solvent-free environment. The starting structure was built by using the SmgGDS-558 structure chosen from MD simulated (see previous section) and aligning the C-terminal cysteine of a KRas model adapted from [132] to the terminal cysteine RhoA in PDB:5ZHX [7]. The farnesyl group of KRas was assumed to be housed within the hydrophobic pocket of SmgGDS-558 between ARMs B and D, thereby, fixing the C-terminus of KRas-FMe at the SmgGDS lipid binding pocket. HVR residues 167 to 185 were designated as flexible and varied. An additional constraint was

implemented based on reports of SmgGDS binding many small GTPases with polybasic regions (PBRs) [133–138]. Studies using a homology model of SmgGDS showed similar PBR iterations with KRas, RhoA, Rap1A, and DiRas1 [6,127]. The PBR of small GTPases associated with an electronegative patch proximal to the hydrophobic pocket of SmgGDS-558 while the G-domains interacted with the previously identified binding groove [8]. The HVR of KRas has a polybasic region containing six sequential lysines. The center-of-mass of this polylysine sequence was constrained to be within 6 Å of the acidic residues within the electronegative patch which neighbor the hydrophobic pocket. Previous modeling studies of salt bridge formation in proteins have used a 4.0 Å cutoff criteria between oppositely charged side-chain groups [139–141]. 6 Å was chosen for this study to facilitate conformational variability of new structures while maintaining proximity of the PBR and acidic residues of SmgGDS-558. Structures were sampled by varying backbone torsion angles within the flexible region. The MC acceptance criteria were computed from energetics of torsion angles determined by the CHARMM 27 all-atom protein force field [91]. SAXS intensities were computed for every simulated complex using CRYSOL 3.0, and χ^2 deviations from the measured data from mixed solutions of SmgGDS-558 and KRas were calculated (Figure 3.19), assuming the experimental SAXS intensities were sufficiently well described by structures of bound complex of SmgGDS-558 and KRas only.

Ca. 160,000 structures were generated and pruned to 19,582 models which fulfilled the specified constraints. Individual conformations of the simulated SmgGDS-558 and KRas-FMe-GDP complex were able to describe the experimental SAXS data suggesting KRas binds the hydrophobic pocket of SmgGDS-558. Due to the flexibility of the HVR of KRas and comparable χ^2 values from individual conformations from MC simulations, an ensemble description of the complex was tested. The entire population of generated MC structures was sorted by their χ^2 values, and subpopulations were defined such that they contained N structures with the lowest individual χ^2 values. An ensemble goodness-of-fit, χ^2_{ens} (defined below), was calculated for subpopulations incrementally increasing population size, N (Figure 3.19).

$$\chi^2_{\text{ens}} = \frac{1}{m-1}\sum_{i=1}^{m}\frac{(I_{\text{e}}(q_i) - \overline{I_{\text{ens}}(q_i)})^2}{\sigma_{\text{e}}(q_i)^2} \tag{3.1}$$

where q_i is the ith data point out of m in the experimental intensity profile I_e with RMS standard error on the mean $\sigma_{\text{e}}(q_i)$. $\overline{I_{\text{ens}}(q_i)}$ is the unweighted average of the modeled intensity at q_i from all conformations within an ensemble.

The plot in Figure 3.19C shows how χ^2_{ens} changes by increasing the population included within the ensemble. At N = 1, the ensemble is composed of the conformation which provides the single best fitting scattering profile to the data. Including more models

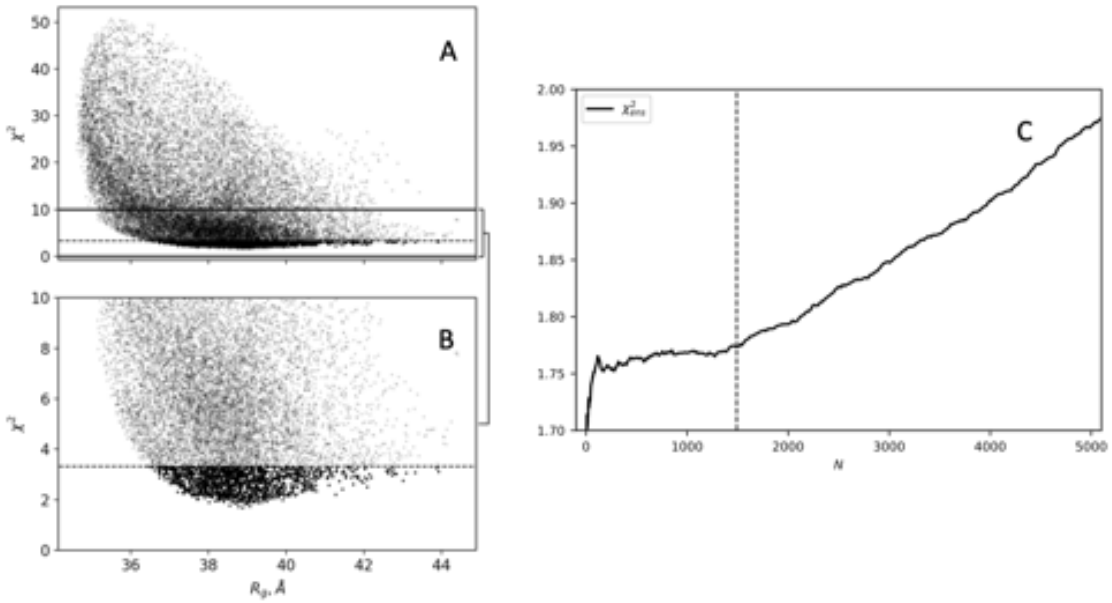

Figure 3.19: Ensemble of MC simulation structures of the SmgGDS-558/KRas complex and comparison to SAXS results. *Left top:* R_g vs. χ^2 where each data point representing a single simulated structure. χ^2 is calculated with CRYSOL 3.0 with respect to SmgGDS-558/KRas scattering data. *Left bottom:* The magnified region of the upper plot is shown in the range of $\chi^2 = 0$ to 10. The dashed line indicates the ensemble cutoff of χ^2=3.329. *Right:* Ensemble goodness-of-fit, χ^2_{ens}, calculated from the averaged SAXS intensity of the N structures with the lowest χ^2. The vertical dashed line indicates the point after which χ^2_{ens} increases without bound as more models are included. The corresponding value of χ^2 is indicated as a dashed line in the plots at the left.

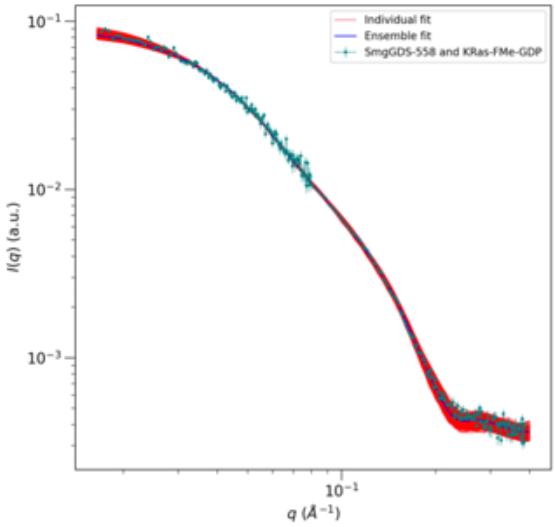

Figure 3.20: Modeled scattering profiles from a SmgGDS-558/KRas ensemble fit to experimental data. Fits from models of a SmgGDS-558 and KRas-FMe-GDP complex are shown with experimental data. Fits from individual models within the identified ensemble are shown as red lines while the ensemble scattering profile is shown in blue.

within the ensemble includes models which progressively provide poorer descriptions of the scattering data, therefore, χ^2_{ens} increases at the lowest values of N. After this increase, a point occurs where including more models briefly improved the quality of fit of the modeled ensemble scattering profile. A plateau in χ^2_{ens} was observed where varying N did not appreciably affect the quality of fit for sub-ensembles to measured data. A limit was chosen, depicted as a dashed line in Figure 3.19C, after which χ^2_{ens} increases without bound for higher N. A complex ensemble was chosen to include all structural configurations below this limit at $N = 1491$. The ensemble averaged predicted scattering profile with individual curves from models within the ensemble are shown in Figure 3.20.

The structural ensemble studied here was validated against solution scattering data by ordering the ability of individual conformations to describe the measured scattering profile of SmgGDS-558 and KRas 1:1 molar mixtures. The χ^2 fit to the data of cumulatively averaged scattering profiles is depicted in Figure 3.20. The largest ensemble was chosen within this region was chosen because, with this measure, there is insufficient reason to reject models up to $N = 1491$. χ^2_{ens} was calculated by incrementally adjusting a cutoff in χ^2, χ^2_{cutoff}, and averaging the scattering profile conformations with individual $\chi^2 < \chi^2_{\text{cutoff}}$. The data shown in Figure 3.20 was calculated with a cutoff

increment of $\Delta\chi^2_{\text{cutoff}} = 0.01$. The chosen ensemble size is the point after which the gradient in χ^2_{ens} remains positive and non-zero.

The occupancy volume of ensembles defined for subpopulations above and below $N = 1491$ were determined and are shown in Figure 3.22. Changing the cutoff value within the plateau does not appreciably change the volume shape or size. For structures above the plateau, their mapped volume is larger, however, does not affect conclusions made from this ensemble modeling study. While this shows that the precise extent of the configuration space of the SmgGDS-558/KRas complex is not well-defined, there are no additional residues identified by mutational studies (Figure 3.4) that could interact with KRas within the subpopulations shown in Figure 3.22. Although the precise definition of the ensemble does not impact interpretation in this scheme, the cutoff point as it is now lacks rigorous motivation. More work in this regard is required.

The relationship between the average of χ^2 values from individual fits, $\overline{\chi^2}$, to the χ^2 value for structural ensemble fits, χ^2_{ens} was explored. Figure 3.23 illustrates the trend of each value for incrementally increasing population size, N. χ^2_{ens} was observed to be less than $\overline{\chi^2}$ for all population sizes (except for $N = 1$ where they are equivalent). It was hypothesized that if χ^2_{ens} was lower than $\overline{\chi^2}$, then this fact might be used as evidence for the accuracy of the structural ensemble for describing the underlying structure which yielded the measured scattering data. Through Jensen's inequality [142], it can be shown that χ^2_{ens} being less than or equal to $\overline{\chi^2}$ is necessarily true. Jensen's inequality states that

$$E(\chi^2(I_{\text{ens}})) \geq \chi^2(E(I_{\text{ens}}))$$

where E denotes the expectation value, $\chi^2_{\text{ens}} = \chi^2(E(I_{\text{ens}}))$, and $\overline{\chi^2} = E(\chi^2(I_{\text{ens}}))$.

The space spanned by the positions of the G-domain for the chosen ensemble is shown in Figure 3.24. SASSIE-WEB [69] was used to generate Gaussian cube density files which were visualized with VMD [13]. It is immediately evident from the volume enclosed by the surface that the G-domain not constrained to a single position on the surface. Positions of the G-domain consistent with scattering data are observed to be near regions of SmgGDS adjacent to the hydrophobic pocket but away from the concave surface. Binding groove residues and one set of anionic residues identified in Figure 3.4 as important for binding KRas are not within the range of the ensemble. Positions of the HVR in the ensemble were mapped to determine if any configurations overlap with residues of interest in SmgGDS. The density is shown in Figure 3.25 and remains proximal to the hydrophobic pocket and encompasses the anionic residues (D190, E193, E197) which were assumed to bind the PBR. The ability of the modeled complex, which is defined by interactions in the PBR and farnesylated C-terminal cysteine residue, to describe SAXS data (see the ensemble fit in Figure 3.20) suggests specific binding

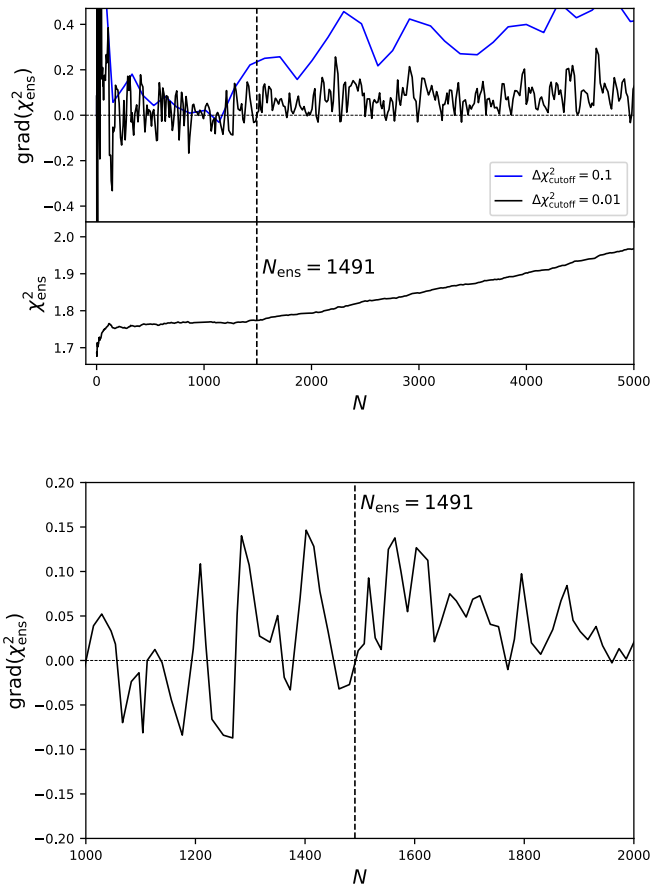

Figure 3.21: Cutoff criteria for the SmgGDS-558 and KRas ensemble. The gradient in χ^2_{ens} was calculated from sampled conformations with individual χ^2 fits to the measured scattering of SmgGDS-558 and KRas samples less than incrementally shifted values of χ^2_{cutoff}. The reported ensemble was chosen to be populated by the 1491 conformations with the lowest individual χ^2 by determining the point after which the gradient in χ^2_{ens} remained positive and non-zero on average. (Top) The gradient was calculated for two different $\Delta\chi^2_{cutoff}$. Larger values show the gradient becoming non-zero and positive for lower population sizes.

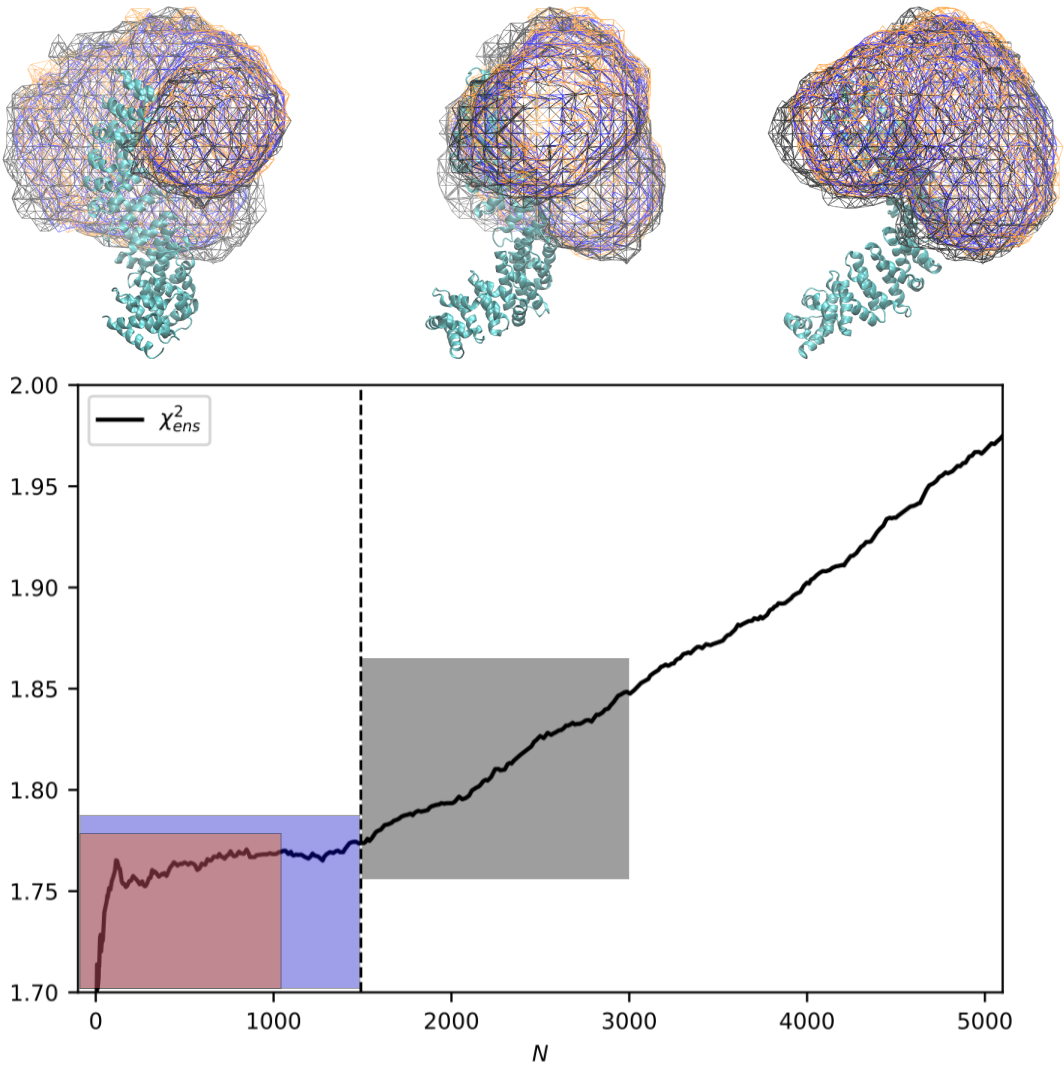

Figure 3.22: Dependence of ensemble volume on subpopulation selection. Real-space volumes enclosing three ranges of χ^2-ranked sampled configurations from MC simulations are shown. The color of the mesh surface in depicted models correspond to the shaded regions on the graph. Examined subpopulations were chosen by ending included structures within the observed plateau (red), at the end of the plateau (blue), and only those past the plateau up to the 3000th lowest χ^2 model.

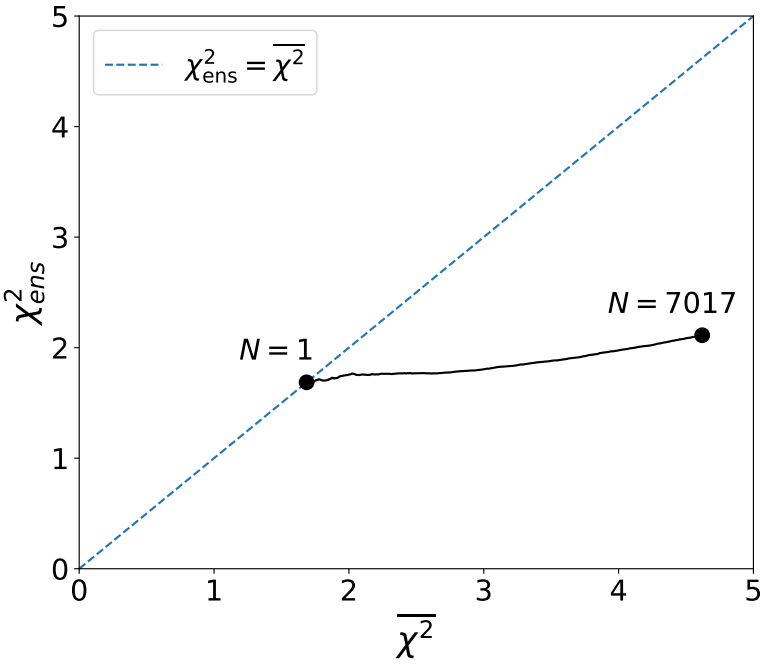

Figure 3.23: Plot of χ^2_{ens} vs. $\overline{\chi^2}$ for population size N. χ^2_{ens} and $\overline{\chi^2}$ was calculated for structures with individual $\chi^2 < 7.0$.

between SmgGDS-558 and fully processed KRas occurs via insertion of the prenyl group into the hydrophobic pocket of SmgGDS and association of the PBR of KRas with SmgGDS residues in the electronegative patch.

3.2.5 Discussion

KRas and other small GTPases within the Ras family which contain a polybasic region (PBR) localize at the plasma membrane (PM) to participate in signaling events [26]. Active processes within the cell have been demonstrated to enrich KRas localization at the PM [31, 99, 109]. SmgGDS-558 is thought to facilitate the transport of fully processed KRas from the ER through the cytosol [6]. A complex of SmgGDS-558 and KRas-FMe has been implicated in a driving role in the development of cancer [109]. Structural details of how SmgGDS isoforms regulate KRas in the membrane localization pathway are critical to the development of therapeutic strategies for Ras-driven cancers [6]. SPR binding studies of SmgGDS and fully processed KRas highlight the potential for SmgGDS-558 to significantly impact KRas membrane association. I report binding affinity of SmgGDS-558 for fully processed KRas is akin to that of KRas for

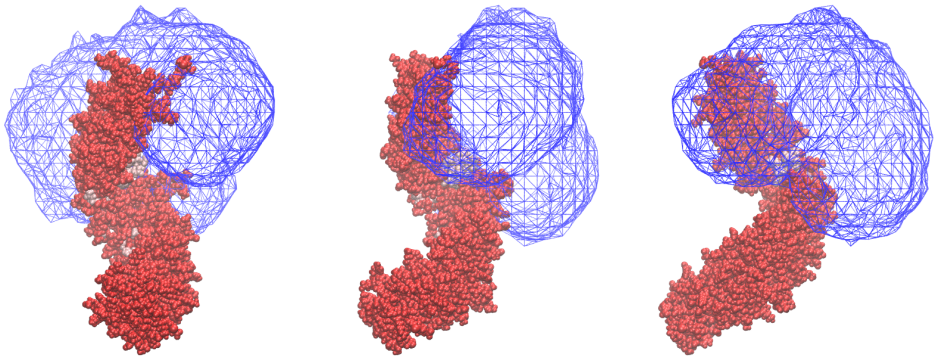

Figure 3.24: Visual representation of a SmgGDS-558 and KRas bound complex ensemble. Shown are three views, rotated by 45° each around the vertical axis of the SmgGDS-558 model used in MC simulations with a transparent surface representing the space occupied by bound KRas conformations populating ensemble which describes the experimental data. SmgGDS is colored red while residues important for binding prenylated KRas *in vivo* (see Figure 3.4) are in pink. The data used to generate the surface was obtained using the Density Map module in SASSIE-WEB and visualized in VMD [13].

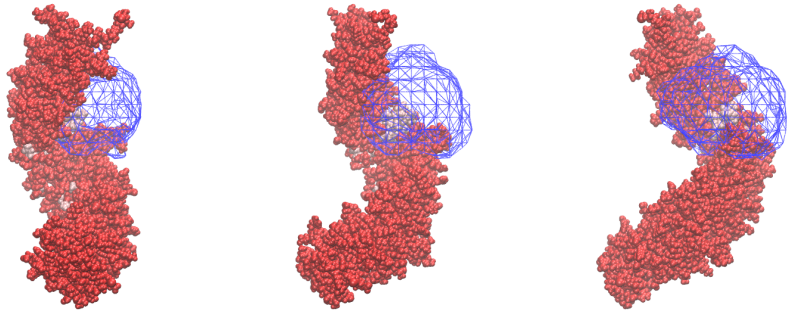

Figure 3.25: HVR structure density remains near the hydrophobic pocket. Three 45° rotations are shown of the space occupied by the HVR within the SmgGDS-558 and KRas ensemble. Of the residues groups interrogated in our mutation study, only (D190K, E193K, E197K) are found within the ensemble surface and thus within the observed interaction range of KRas.

effector proteins and cytosolic chaperones [33,143]. I propose an ensemble model, from a combination of MD and MC simulations, which is consistent with data from SAXS describing a flexible SmgGDS-558 and KRas complex. Implications of these studies on the current understanding of regulatory proteins in KRas pathways, and in particular, its trafficking between the ER and plasma membranes are discussed.

Following its processing by farnesyltransferases, KRas localizes at the ER to undergo further processing by Rce1 and Icmt [93]. SmgGDS-607 is thought to chaperone newly synthesized small GTPases to prenyltransferases [6,105]. SmgGDS-607 is observed to weakly interact with KRas-FMe-GDP at stBLMs consistent with its reported specificity for non-prenylated small GTPases (Figure 3.7). SmgGDS-558 is thought to participate in the subsequent trafficking of prenylated KRas to the PM [6,109,115]. The dissociation constant for KRas binding SmgGDS-558 at anionic stBLMs was found to be comparable to that of KRas-FMe and PDEδ [33]. Isothermal titration calorimetry studies on Ras effector proteins found binding affinities between the effectors and KRas-GppNHp to be similar in magnitude on the order of micromolars [143]. The affinity of KRas-FMe-GDP for SmgGDS-558 ($K_d = 0.53 \pm 0.14\mu$M) is well within the range measured for Ras effector proteins. Additionally, the reported dissociation constant is consistent with the inhibitory role of DiRas1 which reportedly outcompete small GTPase for binding SmgGDS with $K_d = 35 \pm 3$ nM [127]. These findings solidify the role of SmgGDS-558 in solubilizing fully processed KRas. The comparably elevated affinity of KRas for SmgGDS-558 relative to the affinity of KRas binding anionic model plasma membranes [34] suggests the release of KRas from the plasma membrane to bind SmgGDS-558 could be energetically favorable and occur spontaneously. In other words, these SPR binding studies suggest there need not be another participant to release KRas from the plasma membrane allowing it to subsequently bind SmgGDS. In fact, the affinity of KRas for SmgGDS-558 could inhibit its ultimate localization at the PM. It has been suggested and demonstrated in previous studies that active cellular processes enhance the PM association of KRas [31,99]. Arl2 and Arl3 proteins are known to release farnesylated GTPases from PDEδ in healthy cells. It is likely that a similar release factor exists for SmgGDS-558 to eject KRas and blocks KRas reuptake at the membrane. An example of this has been shown in some cancer cells where a truncated form of RabL3(1-36) accelerated prenylation and membrane localization of both wildtype and oncogenic KRas (G12V) by forming a trimeric complex with SmgGDS isoforms and KRas [109].

SmgGDS has been observed to interact with small GTPases through an electronegative patch, a highly conserved binding groove, and a hydrophobic pocket (in the case of SmgGDS-558) [6–8]. Additionally, SmgGDS has thus far been shown to activate RhoA and RhoC [7,8], however, the residues which are critical in promoting GTP/GDP exchange in these small GTPases could facilitate interactions with other Ras proteins.

Sets of residues in SmgGDS implicated in activation of RhoA and binding of Rac1 were subject to mutation to determine their importance in SmgGDS binding fully processed KRas-GDP. Three forms of KRas were test *in vivo*: nucleotide-free, wildtype, and constitutively active GTP-bound (G12V) forms. The nucleotide-state of KRas did not have a significant effect on the observed stability of SmgGDS-558 and KRas complex formation. These results are consistent with modeling of a complex ensemble where no specific interactions with the G-domain observed. Nine sets of residues were studied and only one (D190K, E193K, E197K) was found within the ensemble spanning volume depicted in Figure 3.24. Homology models of SmgGDS-558 binding RhoA, KRas, Rap1A, and DiRas1 were recently reported indicating these small GTPases share binding interfaces with SmgGDS-558. Results from the ensemble modeling of a KRas and SmgGDS-558 complex suggest KRas binds in a manner fundamentally different from RhoA and that shown in homology constructions. Therefore, refinement of SmgGDS-558 homology models interacting with small GTPases is required to predict the contrasting binding mechanisms to KRas and RhoA.

MD simulations of a SmgGDS-558 homology model yielded a collection of structures varying in their ability to describe measured SAXS data collected from SmgGDS-558 samples. RMSD calculations of simulated SmgGDS-558 compared to the partial crystal structure bound to RhoA (PDB:5ZHX) [7] were found to strongly correlate with reduced χ^2 fits of theoretical scattering profiles from models to measured SAXS data of SmgGDS-558 (Figure 3.17). These two independent validation measures assess simulated SmgGDS-558 conformations against solution scattering data and atomistic positions derived from X-ray crystallography studies; the strong correlation between χ^2 and RMSD, therefore, implies the underlying conformation of SmgGDS in solution closely matches that found in crystallography studies [7]. Further, the simultaneous agreement between solution scattering data of SmgGDS-558 and the atomistic crystal structure of a SmgGDS-558 and RhoA complex suggests binding small GTPases does not induce a large conformational change in SmgGDS within the resolution limit of SAXS.

SAXS intensities from mixed samples of SmgGDS-558 and KRas-FMe-GDP were described by a flexible complex under the assumptions that the farnesyl group was housed in the hydrophobic pocket and the PBR interacts with an adjacent subset of electronegative residues. This finding is consistent with previous work suggesting the PBR and C-terminus could be sufficient for binding SmgGDS [7]. The modeling work for a SmgGDS-558 and KRas complex (Figure 3.24) together with mutation sets in IP studies (Figure 3.4) suggest a subset of SmgGDS residues (D190, E193, E197) are important for a stable complex with KRas. The remaining residues highlighted in immunoprecipation studies could be important for initially associating KRas at ER membranes or for binding other ER proteins which facilitate the transfer of fully processed KRas from endomembranes to the cytosol. The SAXS studies were performed under equilibrium

conditions and therefore cannot capture time-resolved structural information of KRas and SmgGDS-558 binding. It is possible these residues are beneficial for the initial binding of KRas but do not interact once the farnesyl tail of KRas is housed within the hydrophobic pocket. In a complex with PDEδ, only the C-terminal CaaX motif, farnesylation, and carboxymethylation groups of KRas were found to interact. In both SmgGDS-558 and PDEδ, complexation interactions are confined within the HVR of KRas which could be of functional important for chaperoning KRas.

SmgGDS is a selective GEF which activates RhoA and RhoC. The identified structural ensemble for SmgGDS-558/KRas in comparison to the structure of SmgGDS-558 and RhoA [7] shows differences in G-domain interactions. This could provide a structural explanation for why SmgGDS does not activate KRas but can activate RhoA. The RhoA G-domain binds to a groove on the concave surface of SmgGDS which induces conformational changes that alter the nucleotide binding region of RhoA. Modeling of KRas bound to SmgGDS-558 refined with SAXS data indicates specific interactions do not occur with the KRas G-domain.

These mutational and biophysical studies suggest SmgGDS-558 binds KRas-FMe in a structurally similar fashion to PDEδ. The structural information reported here is a crucial step toward the development of chemical inhibitors targeting SmgGDS and KRas binding. An ensemble model was presented for a SmgGDS and KRas-FMe complex consistent with SAXS measurements where specific interactions were confined to the PBR and C-terminus of KRas. The upper bound on the binding affinity for SmgGDS solibilizing KRas suggests release factors could be important for localizing KRas to the plasma membrane.

3.2.6 Towards characterization of SmgGDS and small GTPase complexes by NR

Nickel-chelating lipids are frequently used to reversibly immobilize proteins with histidine tags on supported lipid bilayers [144]. Exploratory SPR studies were conducted to measure binding affinities of SmgGDS, which is expressed with a polyhistidine tag, to stBLMs composed of DOPC and 5 mol% nickel-chelating lipid, DGS-NTA(Ni). Both SmgGDS isoforms were titrated onto stBLMs and response values at each concentration to fit to the Langmuir isotherm which is shown in Figure 3.26. Fitted parameters of the response at saturation and dissociation constant are comparable between SmgGDS variants. Slow association occurred at every measured concentration for both SmgGDS isoforms. The elapsed time between measurements was approximately equal and therefore the Langmuir isotherm model can only be loosely applied. These measurements were used in optimizing surface coverage for subsequent neutron reflectometry measurements.

Structural characterization of SmgGDS was performed with NR at 19:1 DOPC:DGS-

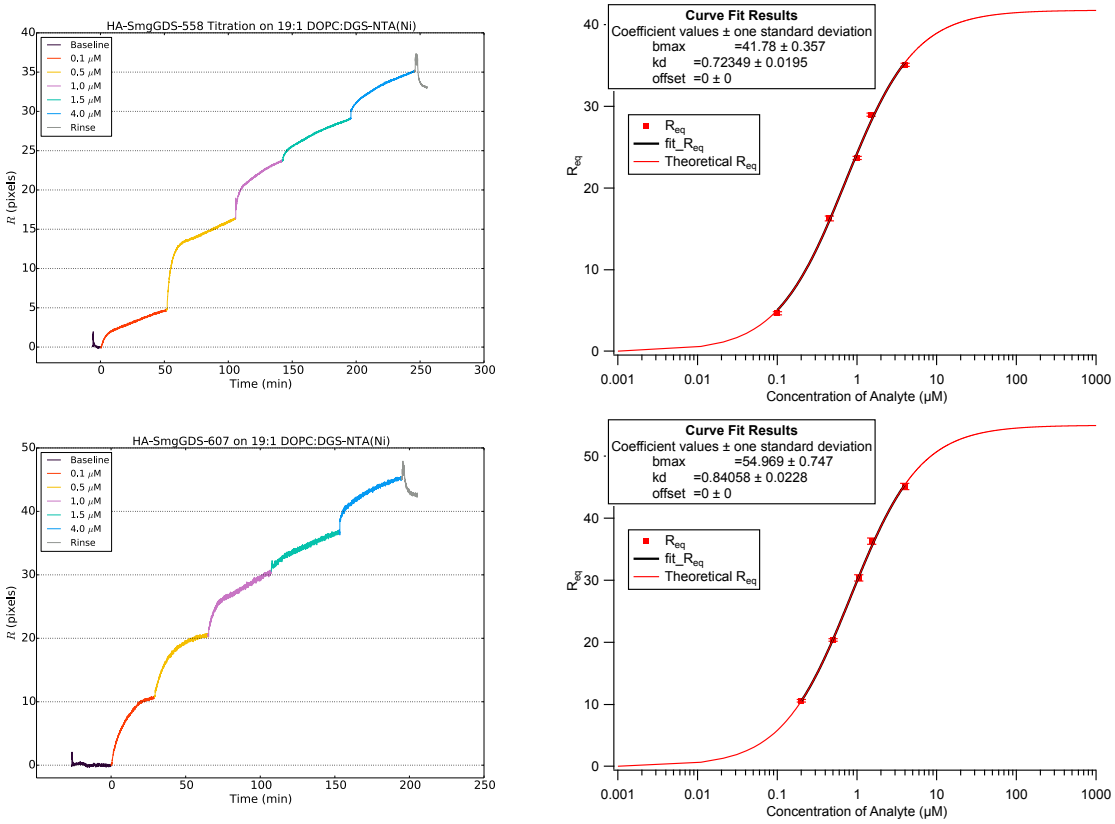

Figure 3.26: Sensorgrams and Langmuir isotherm models of SmgGDS binding via nickel chelation. Representative data is presented of SPR measurements of SmgGDS isoforms binding to 19:1 DOPC:DGS-NTA(Ni) stBLMs. SmgGDS was added to stBLMs at increasing concentrations to obtain equilibrium binding responses. For all concentrations, SmgGDS accumulated at the stBLM surface without reaching a stable equilibrium level. Each concentration was incubated for the same amount of time in a given experiment to attempt a Langmuir isotherm fit. *Top:* SmgGDS-558 is titrated into the stBLM system and a Langmuir model is applied. *Bottom:* SPR data of SmgGDS-607 is shown with the Langmuir model applied to the response values.

NTA(Ni) stBLMs. SmgGDS associates with stBLMs via a polyhistidine tag and nickel-chelating lipid interaction. Two measurements were conducted of 1 and 4 μM concentrations for each SmgGDS variant. Reflectivity profiles of stBLMs incubated with 4 μM are shown in Figure 3.27. The cell was flushed after one hour incubation time and reflectometry profiles were collected. Fit parameters from jointly modeled data sets for each isoform are shown in Table 3.2.

CVO profiles of differing concentration were compared and an increase in concentration led to an increase in magnitude of the protein density profile. This suggests the formation of a monolayer for both isoforms because incubating higher solution concentrations of SmgGDS led to higher densities without lengthening the extent.

The published X-ray crystallography structure of truncated SmgGDS-558 (61-558) [7] was utilized in determining the orientation at the surface via rigid body modeling (see Figure 3.29). Euler angles defining the orientation of SmgGDS relative to the membrane surface were determined and are commensurate with the polyhistidine tag positioned proximal to the membrane surface. Modeling the larger isoform, SmgGDS-607, shows a comparatively elongated density profile which extends into the bilayer. For both isoforms, there is unaccounted for protein density modeled within the bilayer. Density localized within the membrane has large uncertainties and is invariant to the incubation concentration (Figure 3.28) which suggests the bilayer is insufficiently modeled. The modeling algorithm compensates for this by increasing superfluous protein density. It is possible at the time of analysis that DGS-NTA(Ni) was not well described in the fitting process. It is also unlikely SmgGDS-607 inserts into stBLMs as no interaction mechanism with membranes (aside from nickel-chelation with a histidine tag) is known.

This system serves as a platform for future characterization of complexes of SmgGDS and small GTPases. SmgGDS-558 adopts a well-defined orientation when bound peripherally to the stBLM, which facilitates decoupling density profiles arising from a multiple protein construct. Furthermore, contrast can be enhanced within the protein layer at the stBLM interface by deuterating one of the constituents in a protein complex. A potential difficulty in designing these structural studies is the association of the small GTPase to the substrate. Given that SmgGDS is the desired binding site for the ligands, a surface functionalized with nickel-chelating groups that is passive to the small GTPase would be desired. Characterizing a SmgGDS-607 complex is also possible but presents additional challenges. The orientation of SmgGDS-607 was not able to be determined due the lack of an atomistic structure. It can be assumed the N-terminus is oriented proximal to the bilayer surface however the cause of the intermembrane protein density will need to be explored further.

Table 3.2: NR fit parameters for spline modeling of membrane bound SmgGDS. NR data from neat 95:5 ratio DOPC:DGS-NTA(Ni) bilayers and SmgGDS-bound membranes were jointly fit for each SmgGDS isoform. Overall reduced χ^2 values for SmgGDS-558 and SmgGDS-607 data were 1.72 and 1.18, respectively. Uncertainties on substrate parameters are notably large suggesting the MCMC fitting algorithm might not have been sampling from an equilibrated posterior distribution. More *burn in* steps are required to confirm this.

	SmgGDS-558	SmgGDS-607
d_{SiOx} (Å)	$25.2^{+4.7}_{-20.2}$	$11.32^{+2.94}_{-3.76}$
d_{Cr} (Å)	$20.9^{+12.2}_{-10.9}$	$38.51^{+6.82}_{-4.66}$
d_{Au} (Å)	$127.7^{+9.01}_{-17.3}$	$96.83^{+4.72}_{-6.27}$
ρ_{SiOx} (10^{-6} Å^2)	$3.413^{+0.386}_{-0.913}$	$2.547^{+0.504}_{-0.047}$
ρ_{Cr} (10^{-6} Å^2)	$3.744^{+0.456}_{-0.578}$	$4.158^{+0.128}_{-0.060}$
ρ_{Au} (10^{-6} Å^2)	$4.377^{+0.133}_{-0.039}$	$4.346^{+0.161}_{-0.080}$
Roughness (global) (Å)	$3.04^{+2.34}_{-2.04}$	$1.591^{4.156}_{-0.591}$
Roughness (Cr/Au) (Å)	$11.28^{+0.72}_{-10.27}$	$1.535^{+9.381}_{-0.535}$
l_{tether} (Å)	$6.62^{+1.48}_{-0.62}$	$6.45^{+0.97}_{-0.45}$
l_{inner} (Å)	$15.66^{+1.76}_{-1.77}$	$15.01^{+1.63}_{-3.02}$
l_{outer} (Å)	$13.29^{+2.42}_{-1.36}$	$11.24^{+2.74}_{-1.90}$
Neat ν_{bilayer}	$0.995^{+0.005}_{-0.033}$	$0.995^{+0.049}_{-0.067}$
ν_{bilayer} with protein	$0.989^{+0.011}_{-0.033}$	$0.965^{+0.023}_{-0.058}$
Bilayer undulations (Å)	$3.62^{+0.64}_{-0.77}$	$4.43^{+0.07}_{-2.28}$
$\rho_{\mathrm{D_2O}}$ (10^{-6} Å^2)	$6.185^{+0.215}_{-0.038}$	$6.115^{+0.270}_{-0.141}$
$\rho_{\mathrm{H_2O}}$ (10^{-6} Å^2)	$-0.148^{+0.048}_{-0.180}$	$-0.544^{+0.125}_{-0.016}$
Background D_2O (10^{-6})	$-8.437^{+1.381}_{-0.563}$	$-8.470^{+1.29}_{-0.529}$
Background H_2O (10^{-6})	$-5.726^{+0.124}_{-0.131}$	$-5.709^{+0.125}_{-0.093}$

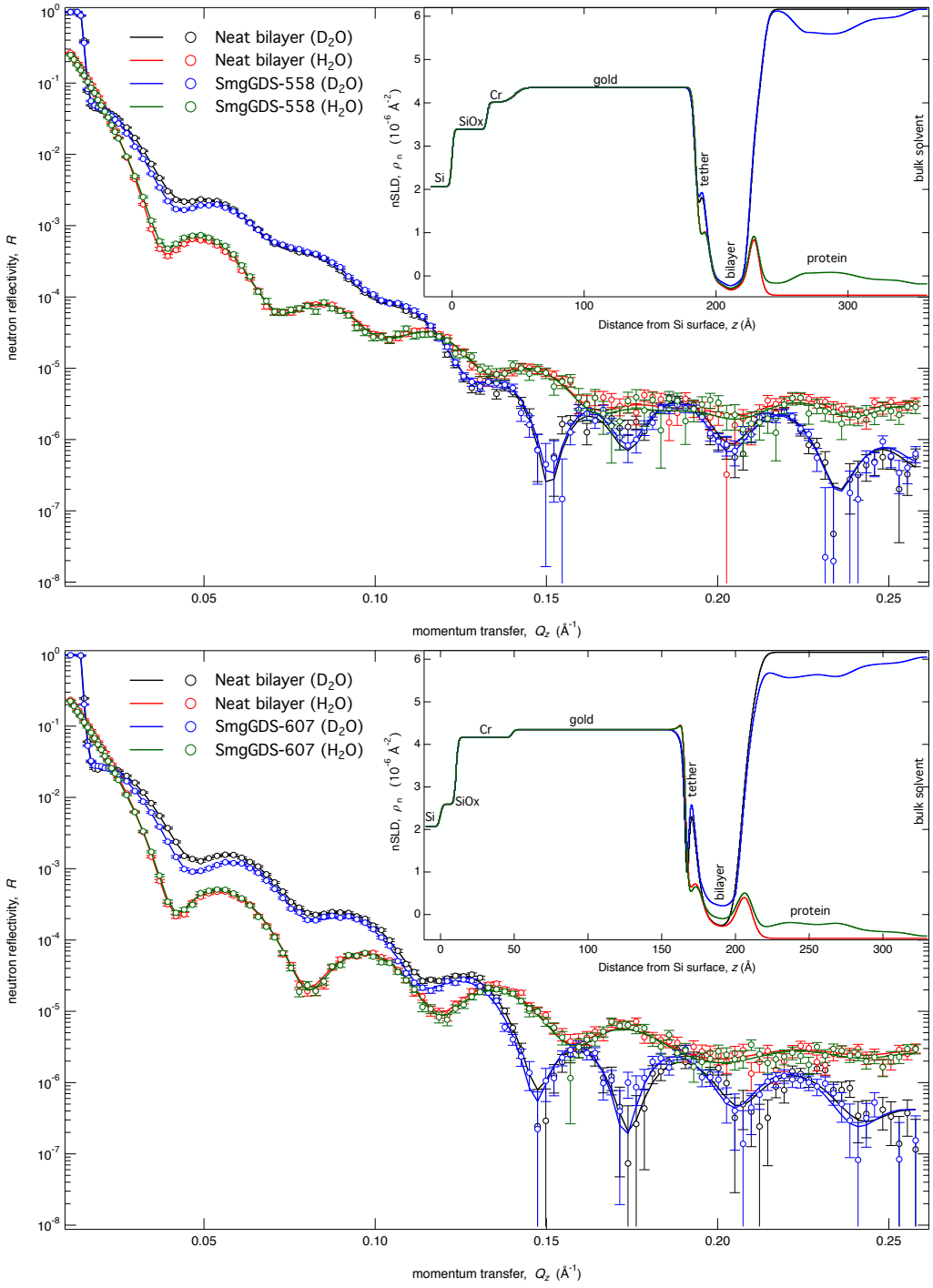

Figure 3.27: Neutron reflectometry data of SmgGDS isoforms bound to stBLM via His-Ni chelation. Four NR datasets are shown for each SmgGDS isoform with accompanying fits. For each sample, two measurements were collected from a neat bilayer and the bilayer following incubation of 4 μM SmgGDS. Two contrasts of D_2O and H_2O based buffer were used to determine the bound structure of SmgGDS to stBLMs with Ni-chelating lipids. Inset within the reflectivity figures are the neutron scattering length density profiles as a function of distance form the silicon wafer surface.

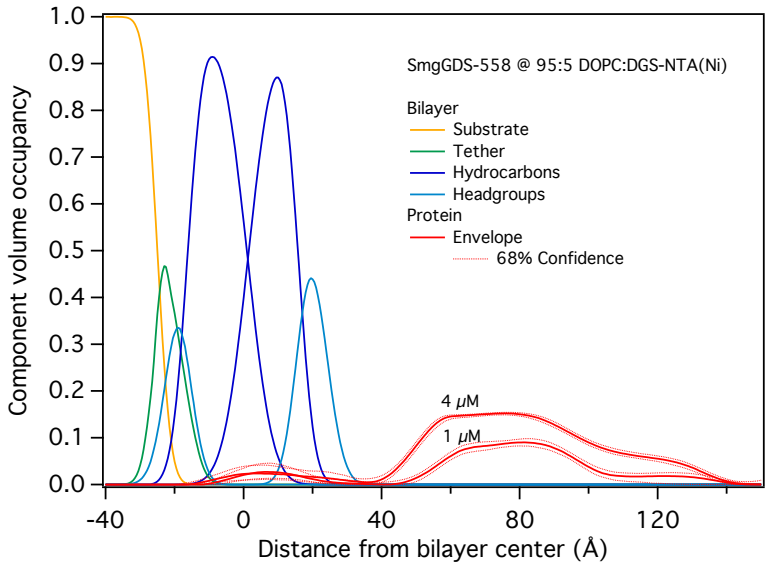

Figure 3.28: Concentration dependence of the CVO of SmgGDS-558 at stBLMs. Modeling of the SmgGDS-558 spline density for increasing incubating concentrations of 1 and 4 μM. Protein density above the bilayer surface differs in magnitude depending on the concentration of SmgGDS-558.

3.3 Conclusions

The effect of SmgGDS isoforms on the binding of fully processed KRas to anionic model membranes was quantitatively assessed in SPR studies. SmgGDS-558 was found to substantially associate and deplete a large fraction of KRas incubated at the membrane. A weak membrane depletion effect was also observed for SmgGDS-607. An upper bound on the dissociation constant of SmgGDS-558 binding fully processed KRas was determined. Solution scattering studies complemented by molecular dynamics and Monte Carlo simulations determined a configurational ensemble of a 1:1 SmgGDS-558/KRas complex in which specific interactions take place in the C-terminal end of the HVR. Characterizations reported here are consistent with the biological role of SmgGDS in the prenylation and localization of Ras proteins.

SPR studies utilizing a stBLM with a charge density which models a generic cellular membrane showed the presence of SmgGDS-558 removes a substantial fraction of bound, fully processed, KRas from the membrane. This finding is in agreement with the model of SmgGDS regulation of KRas (Figure 3.2) in which SmgGDS-558 binds fully processed KRas at the ER. Analysis of SAXS data of a 1:1 mixture of SmgGDS-558 and KRas suggests the proteins bind in a 1:1 ratio. Subsequent molecular modeling, refined with SAXS data, yielded a conformational ensemble which describes the measured scattering profile of the SmgGDS-558 and KRas mixture where the hydrophobic farnesyl

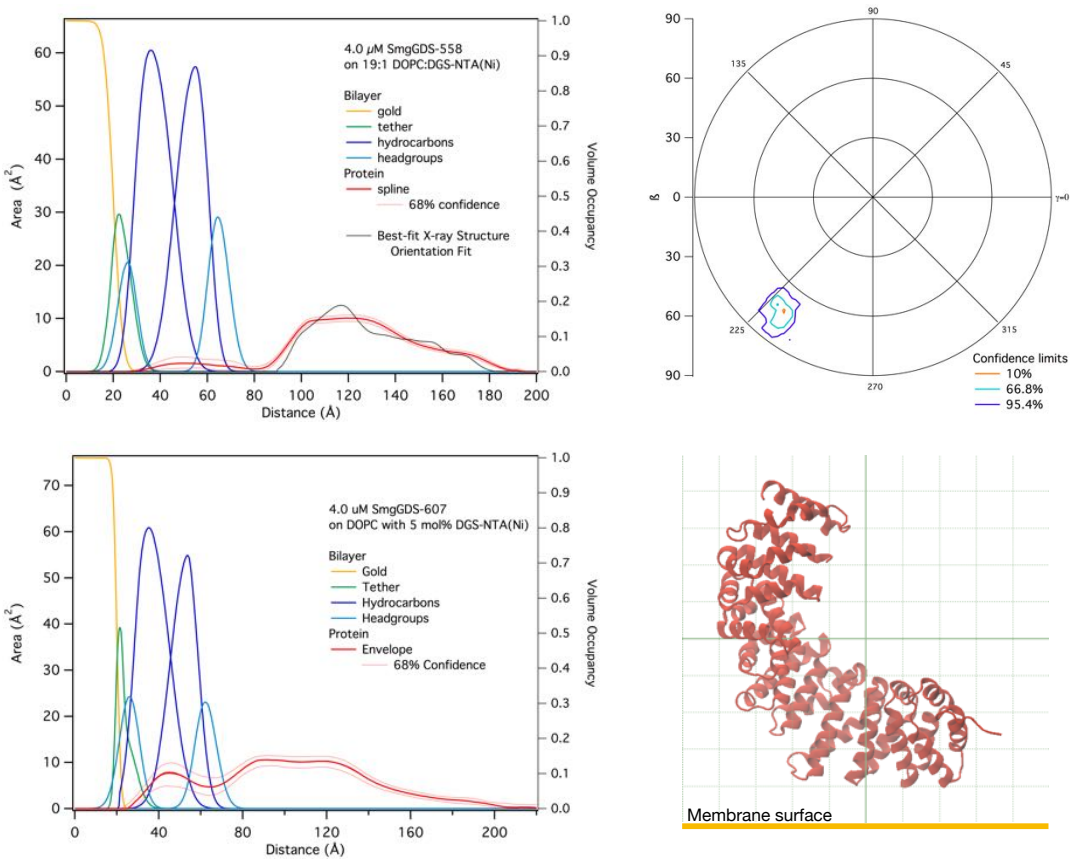

Figure 3.29: CVO profiles with rigid body modeling of SmgGDS-558. 4.0 μM SmgGDS-558 was incubated on stBLMs for one hour. The NR cell was flushed with buffer to remove free SmgGDS from the cell and data was collected. CVO profiles calculated from MCMC fitting of reflectometry data are shown. The red profile representing protein density is modeled at every depth relative to the bilayer. *Top left:* SmgGDS-558 is peripherally bound to stBLMs via nickel-chelation whose density represented by the red spline. *Top right:* The orientation fit with PDB:5XGC is shown. *Bottom right:* The SmgGDS-558 model is shown in the fit orientation relative to the membrane surface. *Bottom left:* CVO profiles of SmgGDS-607 and stBLM are shown.

of KRas is sequestered in SmgGDS-558. Shielding the hydrophobic tail of KRas could be functionally important for trafficking fully processed KRas from the ER to the plasma membrane.

Release factors could be important for catalyzing the release of KRas from SmgGDS-558 to bind the plasma membrane. The conformational ensemble of a SmgGDS-558/KRas complex described in this work suggests the G-domain is loosely interacting with SmgGDS. Effectors or regulators of KRas could feasibly bind the G-domain and promote dissociation from SmgGDS. Abnormal Rabl3(1-36) promotes the prenylation and membrane localization of KRas by binding complexes of KRas with both SmgGDS isoforms in pancreatic cancer [109]. Because this was observed for both isoforms, it is likely this interaction occurs in the cytosol and suggests cytosolic release of KRas enhances its localization to the plasma membrane. Additionally, Ras effector interactions at the plasma membrane could facilitate the transfer of the prenyl group from SmgGDS to the membrane.

Therapeutic targeting of SmgGDS/KRas interactions in cancer is complicated by the expected shared role of SmgGDS with PDEδ in the membrane-localization of KRas. Inhibiting interactions with SmgGDS could have a limited impact if PDEδ remains active in the membrane-localization pathway. One way to circumvent this is to simultaneously introduce inhibitors which separately target PDEδ and SmgGDS. A similar chemical to the PDEδ inhibitor NHTD [114], which targets the hydrophobic pocket, could be similarly effective in preventing SmgGDS from sequestering the prenyl group of KRas.

3.4 Future Directions

3.4.1 Measuring the binding thermodynamics of SmgGDS and KRas

The binding constant between SmgGDS and fully processed KRas was estimated indirectly by inferring the change in concentration of free KRas from the change in membrane-bound coverage upon introducing SmgGDS. It is desirable to perform an experiment where the binding is more accurately quantified. Surface binding assays could be problematic for this specific system as the hydrophobic tail of KRas is sequestered within a specific site on SmgGDS. Immobilizing SmgGDS on a surface could restrict its orientation presented to the bulk solvent and artificially reduce the measured binding with KRas. A solution-based method would be preferred for this system. Isothermal titration calorimetry (ITC) is a method which measures the heat due to the association of a ligand to a receptor. The binding constant, stoichiometry, and enthalpy of binding can be determined from a single experiment [145].

3.4.2 Methods for determining a modeled conformational ensemble

Multiple methods exist in the literature for determining a conformational ensemble of a flexible macromolecular system using structural data [88, 146–150]. The principle disadvantage of the method used in this work is that the ensemble is constructed based on the quality-of-fit of modeled scattering profiles from individual conformations to the experimentally determined profile due to an ensemble of conformations. This heavily penalizes conformations which might individually provide poor descriptions but whose scattering profile could be averaged with other conformations which appropriately compensate in the total scattering profile.

A more rigorous approach than that presented in this thesis would be to first show that the MC simulation successfully converged in the conformational space of the SmgGDS-558/KRas model. In [88], the authors quantified the number of unique 5 Å voxels occupied by C-α atoms as a function of the number of structures in the ensemble. For their system, the simulation converged after approximately 1000 accepted structures. For the SmgGDS and KRas system, this would reduce the computational cost of any subsequent method for determining the flexible ensemble by reducing the number of sampled conformations used. The conclusions drawn in this work are primarily concerned with whether or not the G-domain of KRas is specifically interacting with SmgGDS. Therefore, it could be sufficient to use a method which assigns weights to the scattering profiles of a small number of representative structures from the entire MC simulation of the complex. A Bayesian approach was developed which quantifies the uncertainties of the weights associated with individual conformations within an ensemble which describes the scattering of a flexible macromolecular system [151, 152].

3.4.3 Characterizing the binding of SmgGDS to unprenylated KRas

SmgGDS-607 is known to bind unprenylated small GTPases in cellular contexts [6]. Structural studies of a biologically relevant complex of SmgGDS-607 with unprenylated KRas could identify the binding interface between the two proteins. From the work presented here where fully processed KRas binds SmgGDS-558 via its hydrophobic prenylation, it is not immediately evident how SmgGDS-607 associates with unprenylated KRas. Scattering data of SmgGDS-607 and the fully processed form of KRas suggested signficant aggregate formation occured in these samples. It is unclear whether this is primarily due to reduction of surface cysteines by X-rays or through the, assumedly, solvent-exposed hydrophobic tail of KRas. It is possible that a mixture of unprenylated KRas and SmgGDS-607 would not present the aggregation propensity observed in this

study and, therefore, provide a reliable means of validating MD simulations of the complex.

Chapter 4

Neutron reflectometry studies of zwitterionic DOPC membrane and solid-state surface interactions

Text and figures in this chapter are adapted with permission from [1] D. Michalak, M. Lösche, and D. Hoogerheide. (2021) Langmuir 37, 3970-3981. Copyright 2021 American Chemical Society.

4.1 Introduction

Biophysical studies of planar biomimetic membranes have provided insight to a variety of topics such as membrane protein characterization [153, 154], adsorption of small molecules [155], and lipid bilayer mechanics [67, 156–158]. Additionally, future work on solid substrates are often critical components of model membrane platforms in these studies. Although interfacial forces and potentials governing interactions between phospholipid bilayers and solid support surfaces have been extensively studied [159, 160], a generalized quantitative description is lacking. A variety of challenges inherent to these systems have, thus far, hindered significant developments in this area. Oxidic substrates, such as silica, display complex interactions with aqueous environments [161]. Surface-associated lipid bilayers introduce distinctive interaction mechanisms such as repulsive thermal undulations [162–164] and surface hydration dynamics [165, 166]. Additionally, techniques commonly used for synthesizing bilayers often produce inhomogeneous structural features such as locally pinned areas.

Conventional methods for fabricating lipid bilayers at solid surfaces are limited to a subset of surface chemistries. Formation of planar bilayers by vesicle fusion is generally

successful at silica-based surfaces including glass [167], thermally oxidized silicon [168], and mica [169]. The recently developed solvent-assisted lipid bilayer (SLB) method of formation has shown success on a variety of substrate chemistries [52,170]. Hohner *et al.* described a method for bilayer formation where pure water is slowly titrated into a lipid solution in organic solvent until the solution was 90 mol% aqueous. After thorough rinsing with pure water, contiguous and fluid DMPC membranes were observed at silicon dioxide surfaces. Bulk volume lipidic phases in solution were thoroughly explored with SAXS through the titration process and by varying the temperature. Phase progression was found to correlate with surface coverage. The study also found a somewhat counter-intuitive result where zwitterionic DMPC was observed to have higher affinity to the negatively charged SiO_2 surface than cationic DMTAP [170]. The method was further developed by Tabaei *et al.* into a one-step process utilizing gradual continuous solvent exchange from organic solvent to aqueous buffer [52,171]. QCM-D and ellipsometry studies quantified dry and hydrated masses of surface films at silicon dioxide and oxygen plasma treated gold surfaces. Bilayers at gold surfaces were found to have a greater hydration mass than at silica substrates. The authors suggested differing interfacial hydration forces between gold and silica could explain the differences in hydrated mass. Specifically, TiO_2 is predicted to have strong hydration forces which affect bilayer formation by vesicle fusion; gold was predicted to exhibit similar phenomena due to Hamaker constants for gold and titania surfaces both having much greater values than SiO_2. Although the effects of varying the formation procedure have been extensively scrutinized [52], detailed structural information of the formed bilayers has remained limited. In particular, completeness of SLBs was indirectly measured via BSA protein adsorption.

Neutron reflectometry is a versatile structural characterization technique for planar geometries and has been utilized in a plethora of studies of phospholipid membrane systems [47,60,61]. In combination with composition-space refinement, isotopic variation of the neutron-scattering contrast yields structural profiles of the underlying molecular components with ångström-level precision [46,172]. This framework provides predictive control of unpinned complete zwitterionic bilayers to explore the interaction potential through fine-tuning environmental and compositional parameters.

I present neutron reflectometry studies of a practical system utilizing the SLB formation method which enables fine control of bilayer-substrate interactions through varying buffer composition, lipid composition, and substrate parameters. In addition, a generalized free energy, F, was developed to describe bilayers adsorbed to solid substrates based on an analysis by Israelachvili *et al.* [1,173]. The composite free energy contains four interaction terms: a Hogg-Healy-Fuerstenau (HHF) electrostatic term [174], van der Waals (vdW) interactions for a finite slab at a distance from a half-space with infinite depth [160], bilayer confinement forces [159,162], and short-range hydration

repulsion [175,176]. Discussions of each term and interpretation of experimental results with the free energy model are presented.

NR was used to characterize the formation and structural details of bilayers at solid substrates. All bilayers studied in this work are entirely composed of DOPC, a zwitterionic lipid. Electrophoretic liposome studies show DOPC bilayers have a slightly negative surface potential [177–179]. DOPC bilayers were assumed to have a surface potential of $\psi_b = -5$ mV. Contrasts of fully deuterated and protonated 2-propanol were used in data collections to study SLB formation. Lipid solutions in 2-propanol formed incomplete monolayers at TiO_2 and SiO_2 surfaces whose density is dependent on lipid concentration. These monolayers likely form a template for lipid self-assembly upon gradual solvent exchange to aqueous buffer. After the formation procedure, bilayers at SiO_2, TiO_2, and βMe-passivated Au surfaces were found to be more than 95% complete. Incomplete SLB formation was observed at magnetically sputtered Au surfaces as opposed to Au surfaces treated with oxygen plasma [52]. For silica, strong membrane association with the surface occurred while bilayers were separated by an aqueous layer approximately 14 Å and 18 Å thick for TiO_2 and Au/βMe surfaces, respectively. RMS bilayer corrugations were found to commensurately increase with separation distance and are quantitatively described by the developed generalized potential. Varying the pH and ionic strength of buffering solutions had little effect on the bilayer on SiO_2 due to its strongly negative surface potential while interactions at TiO_2 were highly sensitive to pH changes at intermediate ionic strength (150 mM NaCl). Substituting Tris for HEPES as the buffering compound alters bilayer-substrate interactions and is interpreted as a shift in the surface potential of titania.

4.2 Methods and Materials

Sample preparation

Silicon wafers (1,0,0; surface roughness less than 5Å; 5 mm thick and 3 in. diameter) n-doped to a conductivity between 1 and 100 Ωcm were coated with 100 to 200 Å thick amorphous SiO_2 by dry thermal oxidation or magnetron sputtered to coat with 140 Å thick TiO_2 or Au (300 W, 11 sccm Ar flow rate, chamber pressure: < 1 mTorr) on a Denton Vacuum Discovery 550 sputtering system at the NIST Center for Nanoscale Science and Technology cleanroom. Coated wafers were mounted with surface films facing a 100 μm fluid reservoir for NR measurements as depicted in Figure 4.1. A cylindrical Viton gasket with 65 mm inner diameter separated the sample wafer from a roughened backing wafer. An inlet and outlet were fashioned to the backing wafer and coupled by flat-bottomed fittings (IDEX Health and Science, Oak Harbor, WA) to external tubing for solution exchanges. The Au/βMe sample was formed by incubating

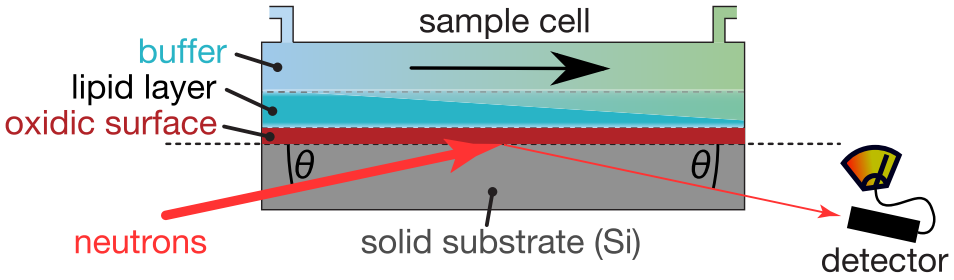

Figure 4.1: Illustration of bilayer formation by solvent exchange in NR sample cell. The NR fluids cell consists of a silicon backing wafer coated by a thin film layer (TiO_2, SiO_2, or Au). A lipid solution in 2-propanol is incubated in the fluid reservoir where an incomplete lipid monolayer adsorbs to the surface. Continuous buffer exchange with an aqueous solution transforms the associated lipidic structure into continuous, complete phospholipid bilayers.

an ethanol solution with 0.2 mM β-mercaptoethanol in an Au-coated wafer cell for one hour followed by rinsing with pure ethanol and water.

Solvent-assisted lipid bilayer (SLB) formation

Dried DOPC (Avanti Polar Lipids, Alabaster, AL) was dissolved in 2-propanol at the desired concentrations, and injected into the fluids cell. An aqueous solution (Millipore), buffered at pH 7.4 by 10 mM tris(hydroxymethyl)-aminomethane ("Tris") or 5 mM 4-(2-hydroxyethyl)-1-piperazine-ethanesulfonic acid ("HEPES") with the desired NaCl concentration, was then injected via syringe pump at 0.057 mL/min for total volume of 5.13 mL (∼12 cell volumes). The average fluid velocity through the cell was comparable to previous work by Tabaei *et al.* at ∼2 $\times 10^{-4}$ m/s.

4.3 Results and Discussion

4.3.1 Characterization of SLB formation on SiOx and TiOx

To investigate the mechanism of SLB formation, two sample cells were constructed containing either amorphously sputtered TiO_2 or thermally oxidized SiO_2. Two NR datasets were collected from each sample where the fluid reservoir was filled with either entirely deuterated (d-IPA) or protonated (h-IPA) 2-propanol. For SiO_2, lipid concentrations of DOPC solutions in 2-propanol were varied to determine the dependence of interfacial structure on the amount of soluble phospholipid. Data was collected on the same substrates as previously measured in both isotopic contrasts for 0.3 mg/mL

and 3.0 mg/mL DOPC concentrations at SiO_2 and 3.0 mg/mL DOPC at TiO_2. Neutron scattering length density (nSLD) profiles of all datasets for a given oxide surface were simultaneously optimized with an MCMC fitting algorithm (as previously described) to determine optimal fit parameter values and 68% confidence intervals and are shown in Figure 4.2 with corresponding reflectivities. Monolayers of lipid were modeled at the surface as a mixture of either headgroup or acyl chain adsorbing to the substrate. An additional fit parameter describing the "completeness" of a monolayer film at the interface was optimized and interpreted as a fractional lipid density by comparison to a fully hydrated DOPC bilayer leaflet ($A = 72.4 \pm 0.5 \text{Å}^2$ per lipid [180]). Interfacial structures for both TiO_2 and SiO_2 substrates were determined to be an incomplete monolayer with acyl chains oriented toward bulk 2-propanol. Fractional lipid densities were found to be $38.6 \pm 0.8\%$ and $58.5 \pm 0.8\%$ for 0.3 and 3.0 mg/mL DOPC in 2-propanol respectively at SiO_2. 3.0 mg/mL DOPC in 2-propanol formed a $47.8 \pm 2.5\%$ fractional density monolayer at the TiO_2 surface.

Incubation of DOPC solutions in 2-propanol at oxidic surfaces is likely necessary to form a template for bilayer formation following continuous solvent exchange. Monolayer headgroups at the interface were resolved to be entirely oriented toward the oxide surface. It is likely that OH-terminal groups at the surface present a sufficiently polar environment, relative to the solvent, to associate the zwitterionic headgroups [181]. Fractional lipid density was found to commensurately increase with increasing dissolved lipid concentration. Although this was not investigated, it is possible that solutions of lower lipid concentration require slower exchange with aqueous buffer to form similarly complete bilayers. The reduced dissolved lipid available to associate and self-assemble at the surface could necessitate a sufficiently slow flow such that bulk motion of the fluid does not significantly inhibit lipid diffusion to within the interaction range of the oxide surface.

SLB formation was completed by gradually exchanging 2-propanol solutions with aqueous buffer. Structures at TiO_2 and SiO_2 surfaces in deuterated and hydrogenated buffer were separately measured and characterized by NR (reflectivity data and modeled nSLD profiles are shown in Figure 4.3; fit parameters for DOPC on TiO_2 at pH 7 are shown in Table 4.3). Following solvent exchange, both substrates yielded bilayers of greater than 95% completeness. CVO profiles of DOPC monolayers and fully formed bilayers on the oxide surfaces, following solvent exchange, are illustrated in Figure 4.4. Solvent was found to fill a 14 Å thick separation between the TiO_2 surface and bilayer headgroups. In contrast, on SiO_2, the membrane was determined to be strongly associated with a negative modeled separation between the surface and bilayer implying headgroup deformation. Bilayer surface corrugations σ_{rms} were similar in magnitude to the roughness of both substrates ($\sigma_s \approx 4$Å and 5 Å for TiO_2 and SiO_2, respectively) where $\sigma_{\text{rms}}^2 = \sigma^2 + \sigma_s^2$ and σ describes bilayer fluctuations. This implies that bilayers

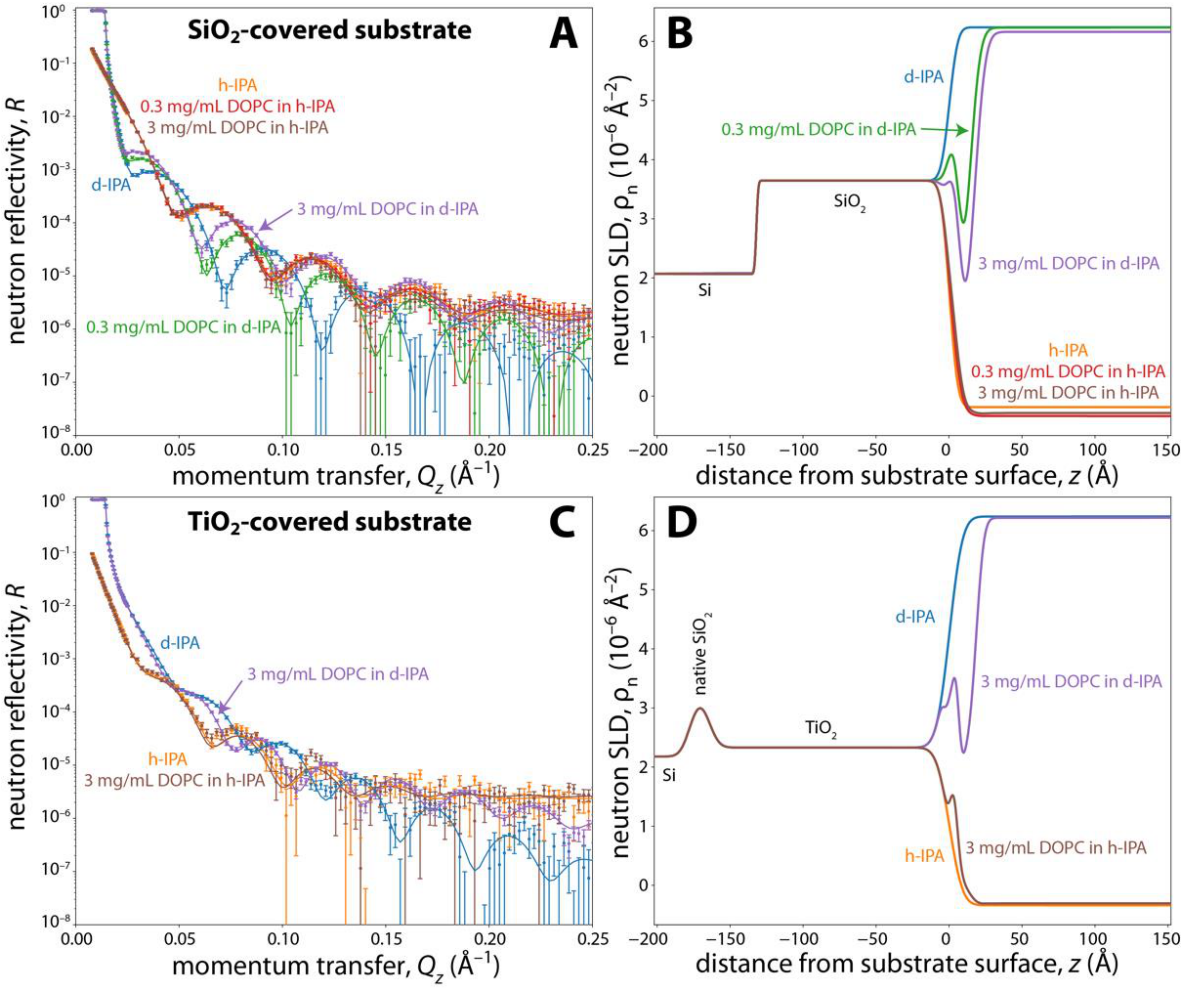

Figure 4.2: Neutron reflectivity curves for describing lipid monolayer formation on SiO_2 and TiO_2 substrates. NR data is shown measuring bare substrates of SiO_2 (A) and TiO_2 (C) with h-IPA and d-IPA bulk solvents. SiO_2 was additionally measured with deuterated and hydrogenated 2-propanol DOPC solutions at 0.3 mg/mL and 3.0 mg/mL concentrations; TiO_2 was measured with similarly contrasting DOPC solutions at 3.0 mg/mL. Error bars represent 68% confidence intervals and solid lines are predictions of the reflectivity calculated from the neutron scattering length density (nSLD) profiles shown in (B) and (D).

were largely conformal to the substrates. On TiO_2, the presence of a water cushion together with the observation that bilayer corrugations were conformal to the surface suggests the bilayer was not locally pinned. If the membrane was pinned to the surface and a water cushion was observed, one would expect the bilayer roughness, σ, to be significantly higher to spread the lipid density closer to the substrate.

4.3.2 Ionic content and pH effects

Bilayers studied in the previous section were subject to further characterization under a variety of aqueous environments to determine differences in membrane interaction with SiO_2 and TiO_2 substrates. After bilayer formation, the pH and ionic strength of the bulk solvent was systemically varied *in situ* to determine how altering the substrate surface potential affected the bilayer distance and RMS corrugations. The observed bilayer properties were then compared to the developed free energy model (in the following section). Buffer exchanges were performed in an identical manner to those used in SLB formation.

Responses to pH variation varied greatly between titania and silica surfaces. Little change was observed for the DOPC bilayer at SiO_2 throughout the entire pH range. Fit parameters from composition space modeling for pH 4, 7, and 11 at SiO_2 and TiO_2 surfaces are listed in Tables 4.2 and 4.3, respectively. On TiO_2, the separation distance and bilayer undulations varied significantly dependent on the solution pH. Raising pH (equivalently, increasing the concentration of negative OH^- ions in solution) pushed the membrane to further equilibrium distances from the surface. At the maximum value of pH 11, modeled CVO profiles displace the bilayer approximately 40 Å away. Bilayer undulations correspondingly increased to $\sigma_{\text{rms}} \approx \sigma \approx 15$ Å. A comprehensive reflectivity dataset (Figure 4.5) was obtained to systemically elucidate interactions of a DOPC membrane on titania surfaces throughout the pH range at differing ionic strengths of 10 mM, 150 mM, and 1 M NaCl. Bilayer-substrate distances and RMS bilayer corrugations were optimized in the model for all data and are summarized in Figure 4.6.

Bilayers were observed to be in contact with the SiO_2 film immediately after formation and throughout a pH range of 4 to 11. At pH 7 and 4, the optimized separation distances between substrate and inner leaflet headgroups were non-zero negative values. This indicates compression of the inner leaflet and, in particular, the headgroup region. Visual inspection of Figure 4.4 finds the inner headgroup distribution more compact on SiO_2 compared to the inner headgroup region of the "floating" bilayer on TiO_2. These results suggest particularly strong association of the bilayer.

Bilayer interactions with TiO_2 were generally similar at 10 mM and 1 M NaCl concentrations remaining proximal to the surface separated by an aqueous cushion.

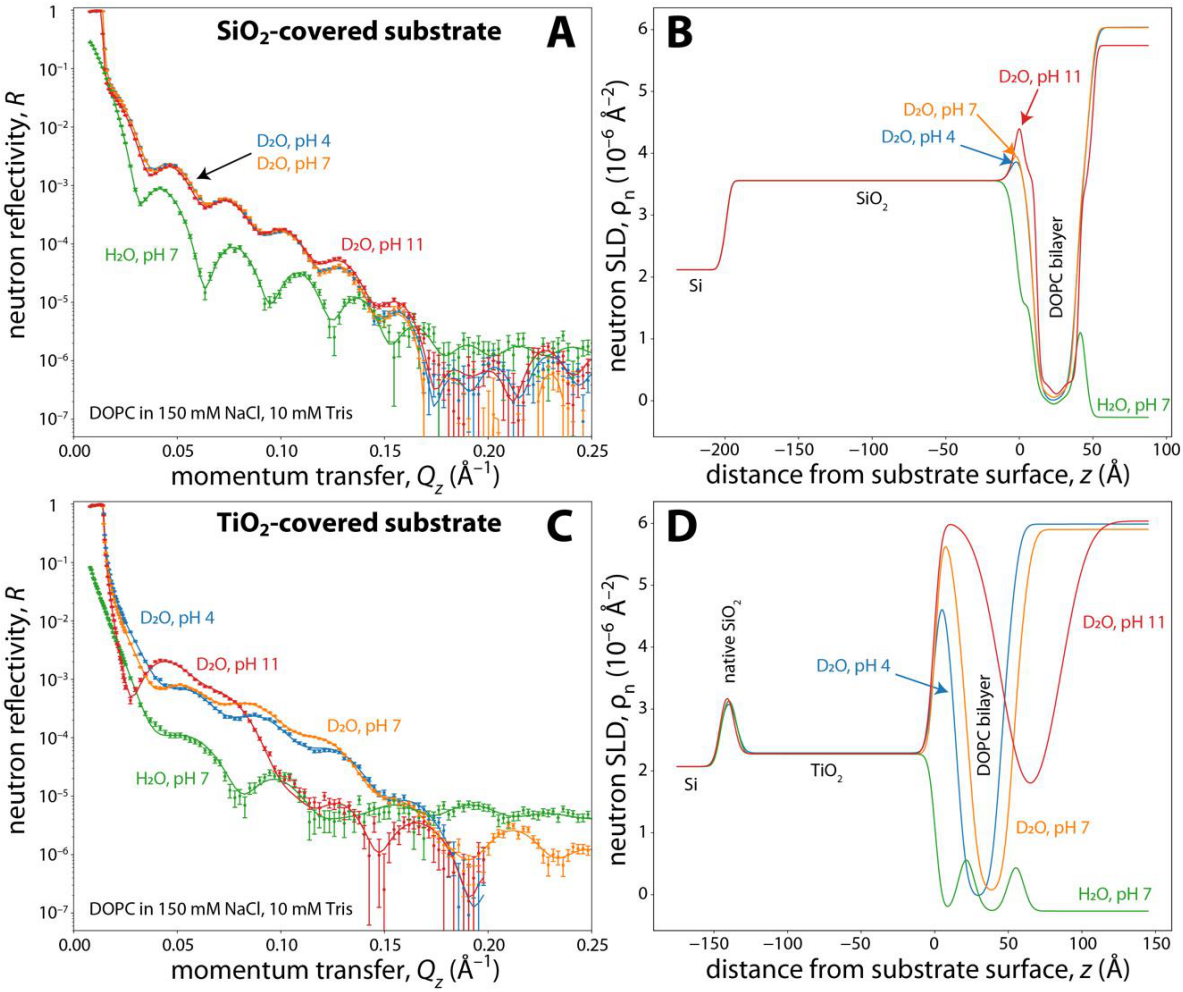

Figure 4.3: Neutron reflectivity curves of lipid bilayers following buffer exchange and pH variation on SiO_2 and TiO_2 substrates. NR data is shown from samples of complete DOPC bilayers on SiO_2 (A) and TiO_2 (C) in H_2O and D_2O solutions buffered with 10 mM Tris-HCl. 2-propanol 3.0 mg/mL DOPC lipid solutions were exchanged with fully hydrogenated buffer at pH 7 to form bilayers and measured with NR. Subsequent measurements were performed at pH 7 followed by pH 4 or 11 in deuterated buffer. Error bars represent 68% confidence intervals and solid lines are predictions of the reflectivity calculated from neutron scattering length density (nSLD) profiles shown in (B) and (D).

Table 4.1: Representative model fit parameters in NR data evaluation Fit parameters for modeling a bilayer adsorbed to TiO_2 at pH 7 and 150 mM NaCl concentration are shown with optimization limits, median value, and confidence intervals (CI). Optimized data sets included both D_2O and H_2O solvent contrasts and were used as a reference for distance determinations for all TiO_2 data.

Parameter (units)	**Lower bound**	**Upper bound**	**Lower 68% CI**	**Median value**	**Upper 68% CI**
Beam parameters					
Total reflectance	*0.9*	*1.05*	0.9470	**0.9493**	0.9517
Sample broadening factor	*0.1*	*10*	0.95	**1.08**	1.2
Angle misalignment (°)	*–0.01*	*0.01*	–0.0091	**–0.0077**	–0.0059
Bulk parameters					
SLD of D_2O (10^{-6} Å^{-2})	*4*	*6.4*	5.87	**5.91**	5.95
SLD of H_2O (10^{-6} Å^{-2})	*–0.566*	*0.4*	–0.3	**–0.27**	–0.24
Background of D_2O data (10^{-6})	*–10*	*100*	0.29	**0.4**	0.5
Background of H_2O data (10^{-6})	*–10*	*100*	3.76	**3.9**	4.04
Substrate parameters					
Si/SiO_x and SiO_x/TiO_x rms interfacial roughness (Å)	*2*	*15*	2.57	**3.66**	4.38
SiO_x thickness (Å)	*0*	*50*	5.96	**8.93**	12.59
SiO_x SLD (10^{-6} Å^{-2})	*2.4*	*4.4*	3.08	**3.43**	4.06
TiO_x thickness (Å)	*40*	*150*	134	**136.9**	137.5
TiO_x SLD (10^{-6} Å^{-2})	*1.4*	*3.4*	2.268	**2.276**	2.285
TiO_x rms surface roughness (Å)	*2*	*25*	3.16	**3.7**	4.2
Bilayer parameters					
Substrate-headgroup separation (Å)	*–5*	*50*	13.66	**13.99**	14.32
Bilayer rms fluctuations (Å)	*2*	*15*	4.88	**5.27**	5.68
Volume fraction of bilayer	*0*	*1*	0.941	**0.952**	0.964
Acyl chain length, inner leaflet (Å)	*10*	*25*	13.62	**14.11**	14.6
Acyl chain length, outer leaflet (Å)	*10*	*25*	11.09	**11.69**	12.28

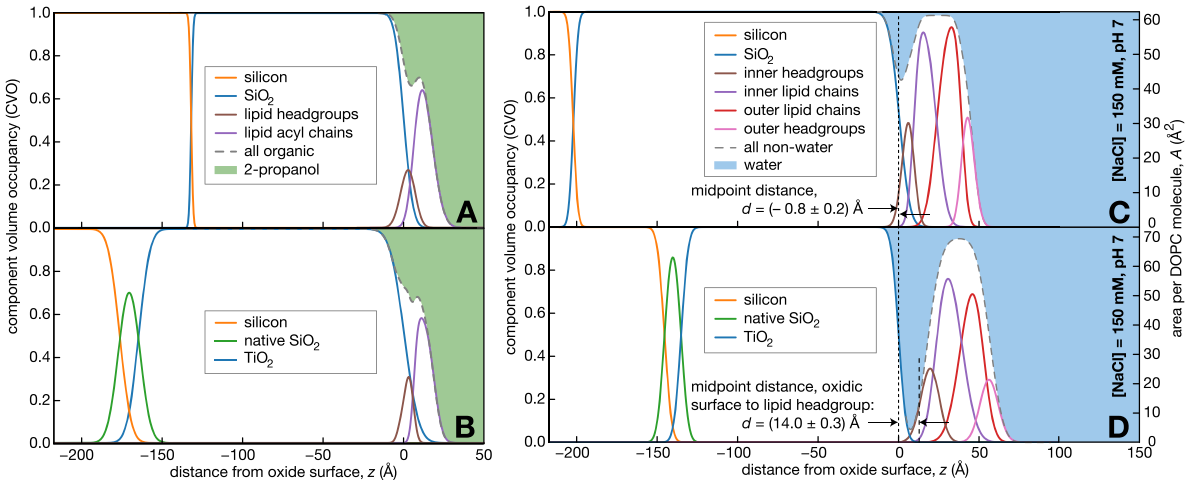

Figure 4.4: CVO profiles of DOPC bilayer formation on oxidic surface films. (A, B) Composition space models of the interfacial structure for 2-propanol DOPC lipid solutions at oxidic surfaces reveal incomplete monolayer formation where lipid headgroups are associating the substrate. (C, D) Following buffer exchange, a complete and continuous DOPC bilayer forms at both surface films. Bilayers formed at SiO_2 (C) are tightly adsorbed while a submembrane aqueous cushion distances DOPC bilayers from TiO_2 surfaces. 68% confidence intervals in the distance from the surface to lipid head are reported.

Slight differences were observed at pH 4 and 5 where the bilayer approached the substrate surface (approximately 5 Å away at pH 4) where RMS bilayer corrugations were similar in magnitude to the substrate roughness. At pH 7 and higher, corrugations of bilayers at 10 mM and 1 M NaCl were effectively equal while bilayers in 1 M NaCl were roughly 5 Å further away. At intermediate ionic strength and high pH, bilayers were only loosely associated with the TiO_2 surface located between 20 and 40 Å away at pH 10 and 11, respectively. Similarly, their RMS corrugations increased to approximately 10 Å at pH 10 and 15 Å at pH 11.

All observed changes in structural characteristics of bilayers studied at TiO_2 and SiO_2 were reproducible regardless of sample history and preparation. For each ionic strength, pH values were pseudo-randomly varied, and optimized fit parameters were reproduced indicating these structural variations are reversible. These provide strong evidence for the characterization of bilayers described here at all pH and ionic strength values being equilibrium properties.

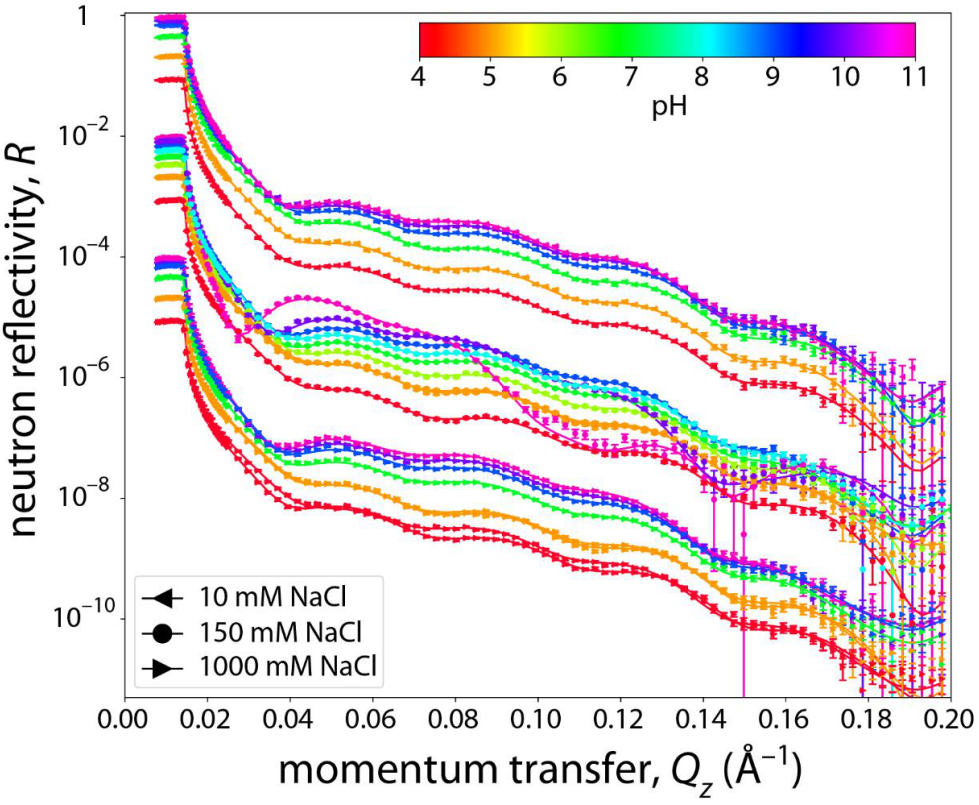

Figure 4.5: Neutron reflectometry profiles from DOPC bilayers in D2O on TiO2. Reflectivity curves are offset on the vertical scale for clarity and pH is denoted by the color scale. From top to bottom, three sets of reflectivity curves are shown at differing concentrations of NaCl at 10 mM, 150 mM, and 1 M NaCl buffered with 10 mM Tris. Error bars represent 68% confidence intervals. Solid lines are predicted reflectivities from composition space models.

Table 4.2: Fit parameters for compositional models of a DOPC bilayer at SiO_2. NR data collected from a single sample under various pH conditions were jointly fit, and shared fit parameters describing the neutron beam and substrate are shown. The ionic strength was held fixed for all measurements using 20 mM Tris and 150 mM NaCl. Uncertainties listed correspond to 68% confidence intervals.

Fit parameters (units)	SiO_2		
	pH 4	pH 7	pH 11
Beam parameters			
Total reflectance		$0.9693^{+0.0022}_{-0.0024}$	
Sample broadening factor		0.024 ± 0.020	
Bulk parameters			
SLD of D_2O (10^{-6} Å^{-2})	$6.396^{+0.003}_{-0.008}$	$6.385^{+0.009}_{-0.011}$	$6.068^{+0.008}_{-0.010}$
SLD of H_2O (10^{-6} Å^{-2})	$-0.424^{+0.027}_{-0.025}$	$-0.552^{+0.020}_{-0.020}$	$-0.180^{+0.030}_{-0.030}$
Background of D_2O data ($10^{-}6$)	$0.062^{+0.048}_{-0.052}$	$-0.022^{+0.08}_{-0.08}$	$0.073^{+0.067}_{-0.073}$
Background of H_2O data ($10^{-}6$)	$1.26^{+0.11}_{-0.11}$	$-0.22^{+0.08}_{-0.08}$	$1.05^{+0.11}_{-0.11}$
Substrate parameters			
Si/SiO_2 rms interfacial roughness (Å)		2.88 ± 1.28	
SiO_2 thickness (Å)		$199.9^{+4.5}_{-1.3}$	
SiO_2 SLD (10^{-6})		3.66 ± 0.01	
SiO_2 rms roughness (10^{-6})		5.23 ± 0.22	
Bilayer parameters			
Substrate-headgroup separation (Å)	-0.7 ± 0.2	-0.8 ± 0.2	2.0 ± 0.2
Inner acyl chain length (Å)	$12.7^{+0.4}_{-0.5}$	$13.0^{+0.5}_{-0.4}$	$11.8^{+0.5}_{-0.4}$
Outer acyl chain length (Å)	14.3 ± 0.4	14.0 ± 0.4	14.3 ± 0.4
Bilayer rms fluctuations (Å)	$3.5^{+0.2}_{-0.3}$	2.6 ± 0.4	$2.4^{+0.3}_{-0.4}$
Volume fraction of bilayer	0.989 ± 0.005	0.976 ± 0.005	0.97 ± 0.005

Table 4.3: Fit parameters for jointly fitting compositional models of a DOPC bilayer in D_2O at TiO_2. NR data collected from a single sample under various pH conditions were jointly fit, and shared fit parameters describing the neutron beam and substrate are shown for pH 4, 7, and 11. The ionic strength was held fixed for measurements using 20 mM Tris and 150 mM NaCl at all pH values. Uncertainties listed correspond to 68% confidence intervals. (Note: the values reported in the publication [1] are from individually fitting each TiO_2 NR profile. Therefore, it is not expected that these joint fit parameters should be identical.)

Fit parameters (units)	TiO_2		
	pH 4	pH 7	pH 11
Beam parameters			
Total reflectance		0.9649 ± 0.0034	
Sample broadening factor		$0.24^{+0.13}_{-0.10}$	
Bulk parameters			
SLD of D_2O (10^{-6} Å^{-2})	$6.251^{+0.006}_{-0.006}$	$6.152^{+0.006}_{-0.005}$	$6.259^{+0.006}_{-0.005}$
Background of D_2O data (10^-6)	$0.039^{+0.087}_{-0.081}$	$-0.046^{+0.033}_{-0.032}$	$0.033^{+0.071}_{-0.069}$
Substrate parameters			
Si/SiO_2 and SiO_2/TiO_2 rms interfacial roughness (Å)		$3.72^{+0.85}_{-1.15}$	
SiO_2 thickness (Å)		$12.9^{+2.7}_{-2.0}$	
SiO_2 SLD (10^{-6})		3.17 ± 0.15	
TiO_2 thickness (Å)		$133.0^{+1.4}_{-1.5}$	
TiO_2 SLD (10^{-6})		2.33 ± 0.02	
TiO_2 rms roughness (10^{-6})		$4.04^{+0.85}_{-1.15}$	
Bilayer parameters			
Substrate-headgroup separation (Å)	$6.0^{+0.6}_{-0.7}$	13.5 ± 0.5	39.0 ± 1.1
Inner acyl chain length (Å)	$14.4^{+0.9}_{-1.3}$	$12.8^{+0.8}_{-1.1}$	$12.7^{+1.2}_{-1.1}$
Outer acyl chain length (Å)	$11.7^{+1.2}_{-1.1}$	$13.0^{+1.2}_{-0.9}$	$16.0^{+1.8}_{-1.3}$
Bilayer rms fluctuations (Å)	$4.1^{+0.7}_{-0.8}$	$3.8^{+0.6}_{-0.8}$	$13.3^{+0.9}_{-0.8}$
Volume fraction of bilayer	$0.956^{+0.017}_{-0.017}$	$0.944^{+0.015}_{-0.013}$	$0.830^{+0.6}_{-0.4}$

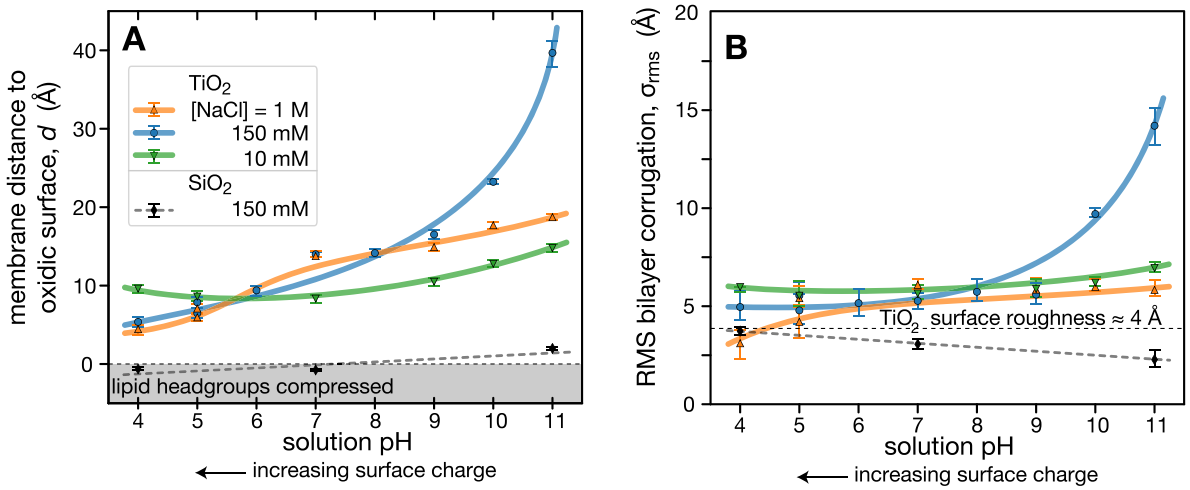

Figure 4.6: Dependence of DOPC membrane separation and RMS corrugation on pH and ionic strength. (A) Separation distances of bilayers as measured from lipid headgroups to substrate surface. (B) RMS undulation amplitudes. Bilayers adsorbed to SiO_2 surface films in 10 mM Tris, 150 mM NaCl buffer are strongly coupled to the surface throughout the pH range with negative apparent distances between bilayers and the oxide film at pH 7 and 4 indicating headgroup deformation. Membranes at TiO_2 films in identical buffer conditions display substantially differing interaction. When varying ionic strength, RMS corrugation and bilayer distances remain similar in a pH range from 4 to 9. Only at an intermediate value of 150 mM NaCl at high pH do bilayers begin decoupling from the surface. Lines through data are visual aides. Error bars represent 68% confidence intervals.

Anionic bilayers were not tested in this study. Measurements of SiO_2 and TiO_2 2-propanol lipid solutions and following buffer exchange would test whether bilayer formation occurs for anionic lipid solutions. It is possible anionic headgroups do not associate OH-terminated surfaces as readily as zwitterionic lipids. During the solvent exchange process, these lipids could be washed out of the cell and be absent from the fully formed bilayer. If anionic lipids are incorporated into a fully formed bilayer, modifications to the free energy model might be needed to describe the separation distance; in particular, the surface potential of an anionic bilayer is unlikely to remain constant under varying pH conditions.

4.3.3 Free energy

The free energy used to quantitatively interpret the NR results of this study was generalized from work by Israelachvili *et al.* for bilayers on glass [173]. Four terms are summed in this model which describe interactions between zwitterionic bilayers and

solid-state substrates: electrostatic interactions, vdW interactions, energetics of bilayer confinement, and a repulsive term describing hydration forces [1]. The assumptions and limitations of each term will be discussed here. The validity of the interaction potential is not expected to hold for separation distances where atomistic structure becomes important (less than 10 Å).

The electrostatic contribution (Equation 4.1) was derived from Derjaguin-Landau-Verwey-Overbeek (D.L.V.O.) theory by Hogg, Healy, and Fuerstenau using the Debye-Hückel approximation for low surface potentials [174]. This term depends on the surface potentials of the solid substrate, ψ_s, and the bilayer, ψ_b, spatially separated by distance, d. The range of electrostatics in a medium with dielectric constant ϵ is also heavily dependent on the Debye screening length, κ^{-1}. Although this was developed explicitly for small potentials (less than |25 mV|), it was reported to be valid for higher potentials [173]. The surface potential of DOPC bilayers was assumed to be constant at -5 mV. Previous studies have shown this value can vary from -6 mV to lower values in the range of 10 to 90 mM NaCl [182]. An assumption in modeling electrostatics in this manner is that the Debye screening length is constant. This is likely a valid assumption when the screen length is smaller than the bilayer separation distance. At closer distances the

$$F_{\text{elec}}(d;\kappa,\psi_s,\psi_b) = \frac{\epsilon\epsilon_0[2\psi_s\psi_b - (\psi_s^2+\psi_b^2)e^{-\kappa d}]}{e^{\kappa d}-e^{-\kappa d}} \tag{4.1}$$

The attractive vdW term is obtained using Hamaker summation for a half-space interacting with a finite slab at a distance, d. For bilayers with headgroup layer thickness t_{hg} and acyl chain layer thickness t_b at oxidic surfaces, the vdW contribution to the free energy is:

$$F_{\text{vdW}}(d;t_b,t_{hg}) = -\frac{A_{132}}{12\pi}\left(\frac{1}{(d+t_{hg})^2} - \frac{1}{(d+t_{hg}+t_b)^2}\right) \tag{4.2}$$

with the Hamaker parameter A_{132}. Hamaker parameters were calculated for titania and silica surfaces interacting with a finite slab of hydrocarbons through water using the summation method [183]. A two-damped-oscillator model was used to calculate the dielectric dispersion functions of silica and titania with resonant frequencies corresponding to infrared and ultraviolet ranges. Low frequency screening of the vdW term by electrolytic solutions can reduce its magnitude by as much as 50% between a bilayer and a SiO_2 surface [184,185]. Estimation of the dielectric response of TiO_2 was reported to not exhibit this screening effect at low frequencies [1]. The dielectric properties of water and tetradecane (representing the acyl chain layer) were calculated using a four-damped-oscillator with tabulated data [160].

An assumption in Equation 4.2 is that the dielectric response of lipid headgroups

is negligibly different from that of water. This assumption is evident in Equation 4.2 the quantity $d + t_{\mathrm{hg}}$ represents the thickness of the medium through which interactions between the solid surface and acyl chain layer take place. This assumption is likely valid for the general case of zwitterionic bilayers at solid-state surfaces. The aqueous medium is a heavily polar environment and the polar nature of the phosphatidylcholine headgroup defines its hydrophilic properties.

Energetics from steric repulsion of bilayers near solid surfaces were calculated as

$$F_{\mathrm{fluct}}(d; c_{\mathrm{H}}, \kappa_{\mathrm{bend}}) = c_{\mathrm{H}} \frac{(k_{\mathrm{b}}T)^2}{\kappa_{\mathrm{bend}} d^2} \tag{4.3}$$

where c_{H} is an empirically determined constant and κ_{bend} is the bending modulus of the membrane. The values of c_{H} and κ_{bend} were set at 0.111 and 19.9 $k_{\mathrm{b}}T$, respectively, based on previous studies [186–188]. This notably does not account for all entropic contributions for confining a fluctuating bilayer at a distance d from a solid surface. F_{fluct} was derived for a bilayer between two rigid plates separated by a distance $2d$ [162]. Only steric interactions were considered in which undulation amplitudes were suppressed.

The short-range hydration forces are in the form of an exponential decay and were empirically derived in [175]. The decay length, λ, was determined for supported lipid membrane stacks to be 1.88 Å and the energy constant, F_0, was found to be 0.2 J/m^2 [165].

$$F_{\mathrm{hydr}}(d; F_0, \lambda) = F_0 e^{d/\lambda} \tag{4.4}$$

The range of F_{hydr} such that it can make significant contributions to the total free energy at distances larger than 10 Å until approximately 20 Å bilayer separation. This form of the hydration force is inadequate for closer distances where it has been shown to be strongly oscillatory [189]. The effect of surface charge on the decay length was found to be negligible in previous studies and therefore was held fixed for all analyses in this study [190].

The components of the free energy of a DOPC bilayer at TiO_2 were plotted at constant substrate surface potential in Figure 4.7A and the summed total of all free energy terms was plotted in panels B-D. The vdW interaction, free energy of bilayer confinement at a surface, and hydration free energy were collectively labelled as "invariant terms" as these contributions are assumed to not vary with ionic strength and surface charge. The potential from the invariant terms is minimum at approximately 18 Å separation. The magnitude of the minimum was calculated to be -2×10^{-13} $k_{\mathrm{b}}T$/lipid using the area per lipid of 71 Å^2. At high ionic strength, the electrostatic contribution is heavily screened. Figure 4.7D illustrates this, where shifting the substrate surface potential from -30 to 30 mV does not significantly change the equilibrium separation

distance. Electrostatics overcome the invariant free energy terms at low ionic strength (Figure 4.7), increasing the depth of the free energy minimum further as the magnitude of the surface potential increases.

Interpretation of TiO_2 and SiO_2 NR data with the free energy model

Each term was summed to model the interaction potential between zwitterionic bilayers near oxidic substrates. Bilayer separations measured at TiO_2 and SiO_2 surfaces were mapped to the free energy landscape in Figure 4.8. The generalized potential predicts bilayers at SiO_2 will remain strongly associated at all pH values measured with $F > 0.5 k_B T$ per lipid. This large interaction energy explains the advantage of using silica substrates for formation of solid-support bilayers by vesicle fusion [191]. The electrostatic component of the free energy dominate interactions between the bilayer and SiO_2 substrate. The surface potential of the SiO_2 substrate at 150 mM NaCl is strongly negative (-100 mV $< \psi_s >$ -50 mV) at all measured pH values [192]. The measurements depicted in Figure 4.6, together with the strongly negative surface potential, suggest this system is localized in lower-left portion of the free energy landscape depicted in Figure 4.8B. The TiO_2-bilayer system exhibits high sensitivity to pH variation at 150 mM NaCl. At this intermediate ionic strength, the electrostatic component to the free energy match the magnitude and range of the invariant components. An experimental study of free TiO_2 (anatase) particles revealed correlation between pH and substrate surface potential [193]. A similar relationship between pH and surface potential is expected for the bilayer-TiO_2 system studied here. In this intermediate ionic strength regime, small changes in pH (surface charge) result in dramatic shifts in the position of the free energy minimum (Figure 4.7C). At pH 7, the TiO_2 surface potential is small, and the invariant interaction terms dictate the position of the equilibrium separation. When the pH is increased, the attractive vdW interaction is countered by a repulsive contribution and shifted the energy minimum to larger separations and shallower in depth ($F \approx 0.29 \times 10^{-3} k_B T$). Although the variations in bilayer-substrate distance are quantitatively described by the generalized potential, two factors prevent direct comparisons between the TiO_2 system in this work and reported anatase surface potentials: ψ_s is likely shifted due to the slightly negative potential of DOPC membranes decreasing the local pH at the interface, and the amorphous sputtered TiO_2 substrate may have differing surface chemistry to anatase particles.

The validity of the electrostatic free energy term at surface potentials greater than 25 mV was tested in by comparing calculations of Equation 4.1 with numerical solutions to the non-linear Poisson-Boltzmann equation in the total free energy as shown

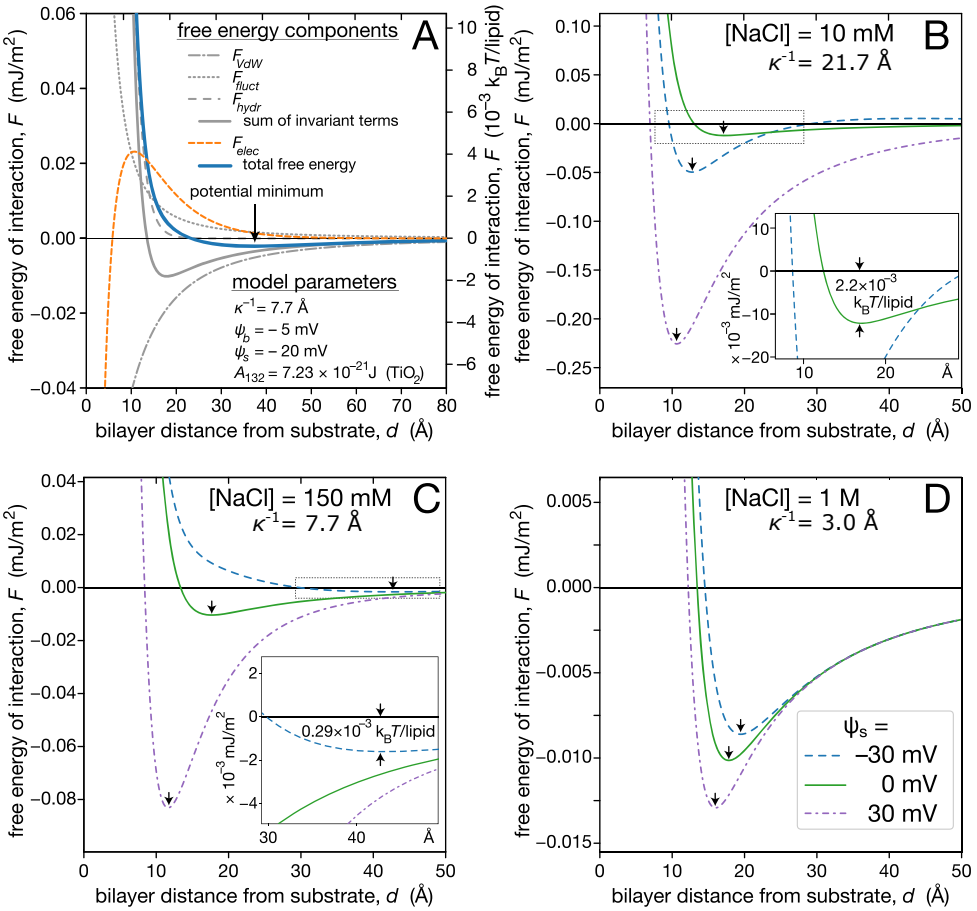

Figure 4.7: Free energy calculations at constant substrate surface potential. (A) Components of the total free energy were calculated for a DOPC bilayer at a titania substrate in 20 mM Tris and 150 mM NaCl buffer. The electrostatic term is the only one which varies with ionic strength and surface charge. The vdW, confinement, and hydration contributions are collectively referred to as "invariant". The invariant free energy minimum is approximately at 18 Å bilayer-substrate separation. Three substrate surface potentials are plotted (ψ_s =-30 mV, 0 mV, and +30 mV) in NaCl concentrations of (B) 10 mM, (C) 150 mM, (D) 1 M. Black arrows indicate the position of the local free energy minimum. (B) and (D) contain insets which magnify the the boxed regions in the plots.

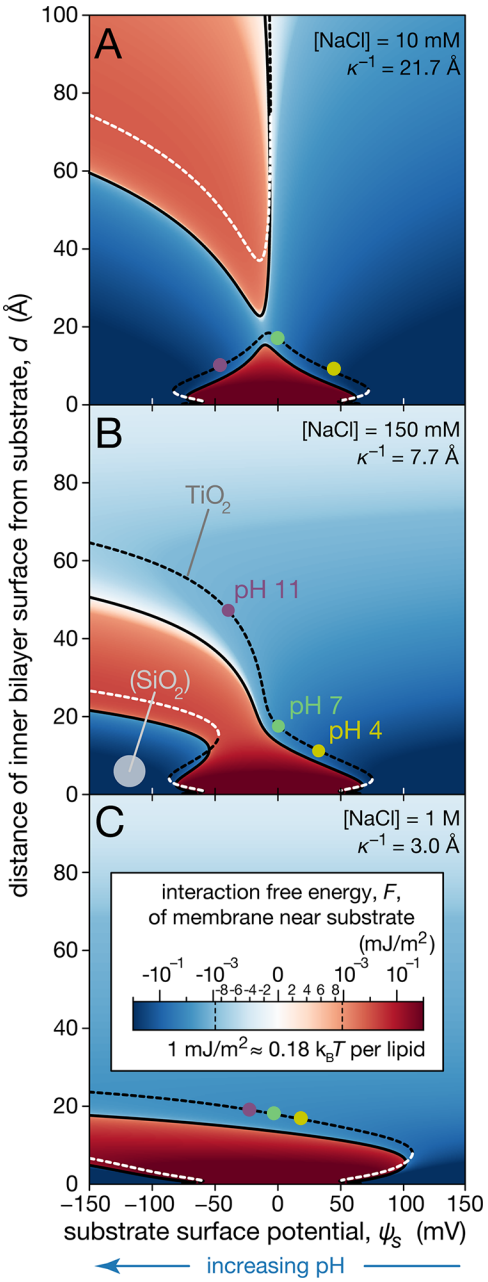

Figure 4.8: Free energy landscape describing DOPC membranes at oxidic surfaces. Energy landscapes were calculated at three ionic strengths including 10 mM Tris. The free energy is represented on a blue to red color scale indicating negative and positive values, respectively. The color scale is linear for magnitudes less than 9×10^{-4} mJ/m^2 and logarithmic at higher values. Solid lines depicting zero potential are shown in black while dashed lines indicate local minima (black) and maxima (white).

in Figure 4.9. Differences between the free energies calculated using each method are apparent at each ionic strength (10 mM, 150 mM, and 1 M NaCl concentrations). The position of bilayers on titania are approximated qualitatively to make comparisons in regions relevant to the experimental work discussed in this chapter. For 10 and 150 mM NaCl, there are negligible differences in the qualitative features of the free energy. At high ionic strength, for high substrate surface potentials, the exact solution displays two minima in the free energy due to the presence of a repulsive region within 20 Å of the surface. Using the HHF equation, only one minimum is observed at zero separation. Despite the magnitude at nearly all surface potentials differing between the linear HHF equation and the Poisson-Boltzmann equation solutions at small separations, the overall landscape in the regions of interest are qualitatively equivalent.

4.3.4 Buffer chemistry can significantly impact bilayer-substrate interactions

From the previous results, it is clear that varying the buffer composition can significantly impact interactions between bilayers and oxidic substrates. A wide variety of pH buffering compounds are utilized in biological and electrochemical studies [194]. Effects of changing the buffering compound were explored in bilayers formed on a TiO_2 substrate. The dependence of bilayer-substrate separation distance on solution pH was explored in HEPES buffered solution for a DOPC membrane at a TiO_2 surface. Four datasets between pH 6 and 11 were collected in HEPES buffer containing 150 mM NaCl. NR data was optimized as described previously.

Optimized fit parameters describing bilayer-substrate separation were plotted (Figure 4.10) with 68% confidence intervals. Bilayers in HEPES at TiO_2 were found to be approximately 7 Å closer to the surface in 5 mM HEPES buffered solution compared with 10 mM Tris solutions from pH 6 to 9 while a larger discrepancy was observed at pH 11. The bilayer in HEPES buffer was closer to the substrate surface at pH 6 than at the lowest separation in Tris buffer. It is likely that differences in buffer adsorption to titania surfaces shifts the effective surface potential. Separation distances plotted in Figure 4.10 between buffering compounds are shifted by approximately 2 pH units.

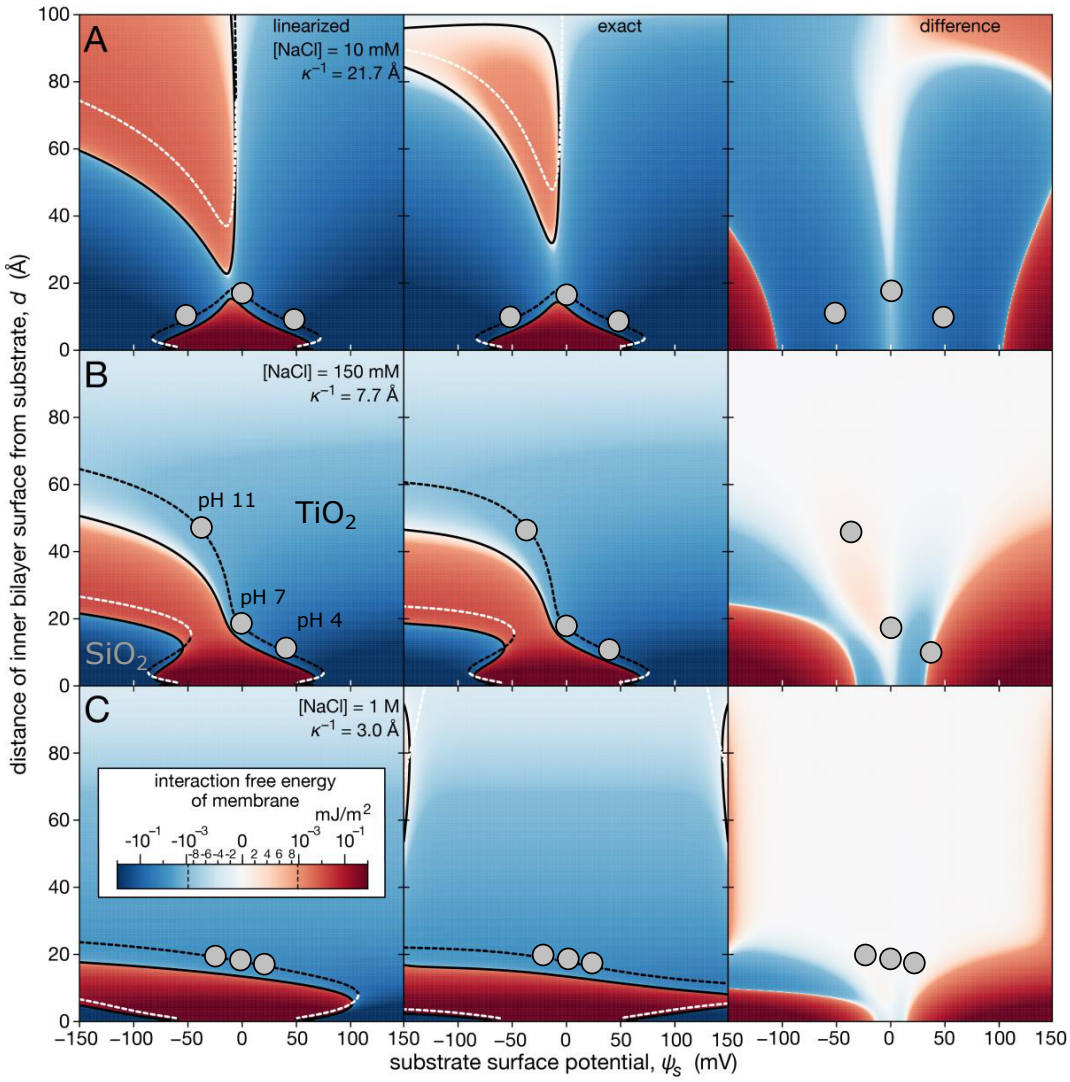

Figure 4.9: Precision of the HHF electrostatic free energy compared to numerical solutions to the non-linear Poisson-Boltzmann equation. Calculated free energies using HHF equation (left) are compared to solutions to the Poisson-Boltzmann equation (middle) by quantifying the difference between the two (right). The interaction free energy of the bilayer is plotted in color as a function of substrate separation distance (y-axis) and substrate surface potential (x-axis). Calculations were performed for three ionic strength conditions corresponding to the concentrations of NaCl tested in NR studies. Approximate locations of bilayers at TiO_2 surfaces in the free energy landscape are shown assuming the substrate surface potential does not change with ionic strength.

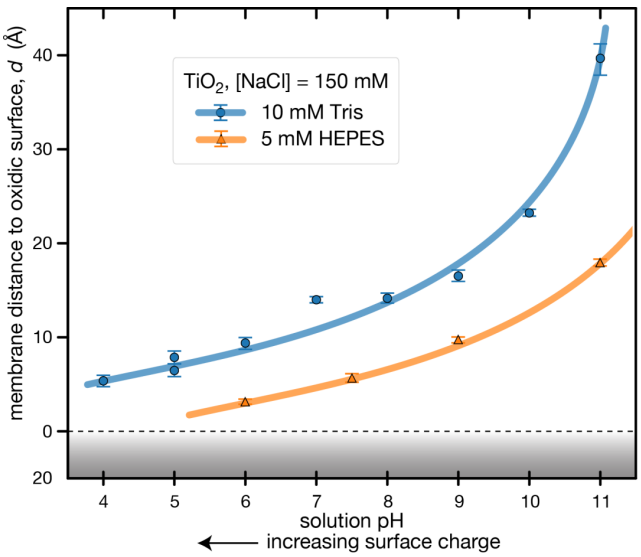

Figure 4.10: Differential effects of buffer chemistry on DOPC bilayer association. A comparison of the bilayer-substrate distances at variable pH is shown for a DOPC bilayer in buffer at physiological ionic strength on a TiO_2 substrate. Data from bilayers in 10 mM Tris and 5 mM HEPES buffered solutions are shown in blue and orange, respectively. Lines tracing the data are visual aides and identical except for a shift by one pH unit and 4 Å.

4.3.5 Bilayer formation at bare Au and βMe-terminated Au substrates

The SLB method has been shown to successfully form bilayers on Au surfaces which were treated with oxygen plasma [52]. Bilayer synthesis was attempted on amorphously sputtered Au substrates with and without a βMe functionalized surface. The SLB formation procedure was identical to those used previously, and NR data was collected in deuterated and protonated aqueous buffers following solvent exchange.

Bare Au substrates were not observed to facilitate formation of complete and inhomogeneous bilayers. Two attempts at bilayer formation were performed at 0.3 and 3.0 mg/mL DOPC lipid concentrations in organic solvent. Following aqueous buffer exchange, NR data was analyzed and optimized bilayer parameters from compositional space modeling reduced bilayer leaflet thicknesses to their minimum values (10 Å) with $\sim$ 40 to 50% bilayer completeness. This mass of lipid was determined to be approximately 4 Å away from the surface. It is difficult to determine the nature of interfacial structures due to poor modeling. An additional fit was attempted without a bilayer but was not able to describe the reflectivity data. This inability to form a high quality bilayer at Au substrates is at odds with published data [52,195]. An important step mentioned in the sample preparation procedure of [52] describes treating the Au

surface with oxygen plasma. Au substrates in this work were amorphously sputtered and vacuum sealed until data collection. Low-pressure oxygen plasma treatments of Au films are known oxidize the surface forming Au_2O_3 with a half-life on the order of a day [196,197]. It is conceivable that the presence of such an oxide layer could facilitate SLB formation.

Following attempts at bare Au, lipid bilayer formation was attempted at a gold surface chemically passivated by a self-assembled monolayer of β-mercaptoethanol (βMe). 0.2 mM βMe dissolved in ethanol was incubated in the NR sample cell and the SLB procedure was performed using 3.0 mg/mL DOPC. A complete ($> 95\%$) bilayer was observed separated from the surface by approximately 18 Å of aqueous cushion at pH 7. Bilayer fluctuations were similar to those found for bilayers on TiO_2 at intermediate ionic strength and high pH at roughly 8 Å. These results suggest βMe adsorption modified the Au surface to facilitate SLB formation by presenting a OH-terminated chemistry to associate DOPC headgroups.

To determine if the free energy model could explain the observed bilayer properties, the magnitude of the vdW contribution to the generalized free energy was calculated for bilayers at gold substrates. The Hamaker parameter was calculated with the dielectric dispersion function $\epsilon(i\xi)$ of gold as [183]

$$A_{132} = \frac{3k_bT}{2}\sum_{m=0}^{\infty}\sum_{s=1}^{\infty}\frac{(\Delta_{13,m}\Delta_{23,m})^s}{s^3}$$

where

$$\Delta_{kl} = \frac{\epsilon_k(i\xi_m) - \epsilon_l(i\xi_m)}{\epsilon_k(i\xi_m) + \epsilon_l(i\xi_m)}$$

The summation in the equation for the Hamaker parameter are over m where sampling frequencies ξ_m are spaced apart by $4\pi^2 k_bT/\hbar$. The summation over s is the third order polylogarithm of the quantity $\Delta_{13}\Delta_{23}$. A four-damped oscillator model was used to calculate the dielectric dispersion as

$$\epsilon(i\xi_m) \approx 1 + \sum_{j=1}^{4}\frac{f_j}{\omega_j^2 + g_j\xi + \xi^2} \tag{4.5}$$

where the index j represents the jth oscillator with spectroscopic fit parameters ω_j, g_j, and f_j [160]. Tabulated fit parameters for gold in [160] do not include a value for ω_1. When setting ω_1 to zero, the $m = 0$ term in Equation 4.5 diverges due to the first sampled frequency being zero. The contribution of this term to the Hamaker parameter for gold interacting with a bilayer through water was estimated by shifting the sampling

frequencies by $+C4\pi^2 k_B T/\hbar$, where C varied from 10^{-9} to 10^0. The upper limit on this range corresponds to omitting the $m = 0$ term when integrating over the sampling frequencies. During this process, the Hamaker parameter of gold ranged from 6.33×10^{-21} J to 8.95×10^{-21} J. These are similar in magnitude as the Hamaker parameter for TiO_2 interacting with a bilayer through water, 7.23×10^{-21} J, and, therefore, it is expected that the free energy model would predict similar equilibrium bilayer-substrate separations for gold and TiO_2 surfaces. The observed separation between the bilayer and gold surface, 18 Å, falls in line with this assessment where the separation at TiO_2 was 14 Å. As a result, this is evidence for the generalized potential describing zwitterionic bilayers at oxidic surfaces could predict interactions at βMe-terminated gold surfaces. The ability of the free energy potential to quantitatively describe observed phenomena between zwitterionic bilayers and TiO_2, SiO_2, and βMe-terminated Au substrates suggests this model could be generalized to surfaces with OH-termination.

Due to restrictions on NR measurement time, the formation at bare Au and βMe-terminated Au substrates was not measured in this study. Due to OH groups at the surface, it is likely that Au surfaces functionalized with βMe present a sufficiently hydrophilic surface for zwitterionic headgroups to associate. NR data to confirm the presence of a monolayer template for subsequent bilayer formation upon solvent exchange is needed to confirm this. A more rigorous means of estimating the Hamaker parameter of gold interacting with a lipid bilayer across water would aide in fully interpreted observed separations at βMe/Au substrates. This would also provide a check for the model's ability to describe bilayer-substrate interactions with varying pH and ionic strength.

4.4 Conclusions

The formation mechanism and morphology of bilayers synthesized by solvent exchange at solid substrates was characterizations by a combination of systematic experimental studies and theoretical predictions. Incomplete lipid monolayers associated to TiO_2 and SiO_2 were observed in 2-propanol lipid solutions in which the headgroups were oriented toward the surface. Upon exchange with aqueous solvent, complete DOPC bilayers were characterized at TiO_2, SiO_2, and Au/βMe substrates via composition space modeling of NR data. Buffer conditions were systematically varied to study the effects of substrate surface charge on the adsorption of zwitterionic bilayers. Using a free energy model describing bilayer-substrate interactions as a superposition of electrostatic, van der Waals, steric, and hydration components, we determined that, in a narrow range of experimental conditions, electrostatic forces balance the remaining free energy contributions. The range and magnitude of electrostatic interactions can be finely controlled by changes in surface and buffer chemistry. Additionally, the ability of the free

energy potential to quantitatively describe observed phenomena between zwitterionic bilayers and TiO_2, SiO_2, and βMe-terminated Au substrates suggests this model of zwitterionic bilayers extends to surfaces with OH-termination. Limitations of the terms in the generalized free energy were discussed and corrections for atomistic distances are required to accurately describe interactions at this level. This study highlights the complexity of interactions defining the interface of solid and soft materials while providing a means to probe their delicate balance with a lipid membrane system.

The properties of the system studied in this work could be exploited for the development of a biosensor. At intermediate ionic strength, the bilayer-substrate separation is highly sensitive to the surface charge (i.e., potential) of titanium dioxide. Altering the charge density of the bilayer *in situ* should produce a measureable change in the surface potential of the substrate. A cylindrical electrochemical sensor could be constructed such that one circular surface is composed of Au while the opposite surface is an Au film functionalized with βMe. The wall separating the caps should be highly insulating to ensure the only electrochemical connection between the surfaces is through the solution filling the cell. By monitoring the potential difference between the caps, an analyte can be introduced to the system and any adsorption to the bilayer which alters the surface chemistry should be detectable. Proper precautions should be taken to ensure the analyte does not adsorb to the substrate surface. In this case, a three step process can be performed where the substrate potential is measured in 1) a "blank" buffer solution, 2) the analyte solution (with identical buffer composition), and 3) a second "blank" solution. Any difference between the potentials measured in steps 1) and 3) would indicate analyte adsorption to the oxidic surface. A bilayer could then be formed in the cell and the surface potential could be measured to detect changes in bilayer properties due to an analyte.

4.5 Future Directions

4.5.1 Dependence of bilayer-substrate separation on ionic strength and pH at a functionalized Au surface

A gold substrate functionalized with βMe-SAc was found to facilitate the formation of a DOPC bilayer by slow solvent exchange. To explore the sensor-like properties of this system, it would be beneficial to map the free energy landscape of a DOPC bilayer formed at the functionilized Au surface. If the surface charge of the substrate can be similarly altered as for titania, this suggests that externally altering the surface charge, by applying a potential across the cell, could controllably shift the distance between bilayer and substrate surfaces.

4.5.2 Voltage control of bilayer-substrate separation

The experimental cell used in this study could be constructed such that an external potential could be applied between the two surfaces separated by a Viton O-ring. The Au surface functionalized with βMe could serve as a working electrode while a reference Ag/AgCl electrode is positioned near the opposite bare Au surface. An auxiliary electrode could be adhered and electrically isolated from the bare Au surface. A bilayer formed in this cell using the preparation method described in this work could be studied with NR under a varying applied surface potentials. Properly constructed, it is possible that the separation could be simply controlled by varying an applied DC voltage across the cell. This would present an opportunity to further interrogate the free energy model described previously.

Bibliography

[1] Michalak DJ, Lösche M, Hoogerheide DP (2021) Charge Effects Provide Ångström-Level Control of Lipid Bilayer Morphology on Titanium Dioxide Surfaces. *Langmuir* 37(13):3970–3981.

[2] Berman HM, et al. (2000) The Protein Data Bank. *Nucleic Acids Research* 28(1):235–242.

[3] Steinman RM, Mellman IS, Muller WA, Cohn ZA (1983) Endocytosis and the recycling of plasma membrane. *The Journal of cell biology* 96(1):1–27.

[4] Shenoy S, et al. (2010) In-plane homogeneity and lipid dynamics in tethered bilayer lipid membranes (tBLMs). *Soft Matter* 6(6):1263–1274.

[5] Pettersen EF, et al. (2004) UCSF Chimera–a visualization system for exploratory research and analysis. *Journal of Computational Chemistry* 25(13):1605–1612.

[6] Brandt AC, Koehn OJ, Williams CL (2021) SmgGDS: An Emerging Master Regulator of Prenylation and Trafficking by Small GTPases in the Ras and Rho Families. *Frontiers in Molecular Biosciences* 8:685135.

[7] Shimizu H, Toma-Fukai S, Kontani K, Katada T, Shimizu T (2018) GEF mechanism revealed by the structure of SmgGDS-558 and farnesylated RhoA complex and its implication for a chaperone mechanism. *Proceedings of the National Academy of Sciences* 115(38):9563–9568.

[8] Hamel B, et al. (2011) SmgGDS is a guanine nucleotide exchange factor that specifically activates RhoA and RhoC. *Journal of Biological Chemistry* 286(14):12141–12148.

[9] Williams CL (2003) The polybasic region of Ras and Rho family small GTPases: A regulator of protein interactions and membrane association and a site of nuclear localization signal sequences. *Cellular Signalling* 15(12):1071–1080.

[10] van Meer G, Voelker DR, Feigenson GW (2008) Membrane lipids: Where they are and how they behave. *Nature reviews. Molecular cell biology* 9(2):112–124.

[11] Konarev PV, Volkov VV, Sokolova AV, Koch MHJ, Svergun DI (2003) *PRIMUS* : A Windows PC-based system for small-angle scattering data analysis. *Journal of Applied Crystallography* 36(5):1277–1282.

[12] Svergun DI (1992) Determination of the regularization parameter in indirect-transform methods using perceptual criteria. *Journal of Applied Crystallography* 25(4):495–503.

[13] Humphrey W, Dalke A, Schulten K (1996) VMD: Visual molecular dynamics. *Journal of Molecular Graphics* 14(1):33–38, 27–28.

[14] Phillips R, Kondev J, Theriot J, Garcia H, Orme N (1998) *Physical Biology of the Cell*. (Garland Science), Second edition.

[15] Watson H (2015) Biological membranes. *Essays in Biochemistry* 59:43–69.

[16] Sengupta D, Linstedt AD (2011) Control of Organelle Size: The Golgi Complex. *Annual Review of Cell and Developmental Biology* 27(1):57–77.

[17] Fahy E, et al. (2009) Update of the LIPID MAPS comprehensive classification system for lipids. *Journal of Lipid Research* 50(Suppl):S9–S14.

[18] Hutagalung AH, Novick PJ (2011) Role of Rab GTPases in Membrane Traffic and Cell Physiology. *Physiological Reviews* 91(1):119–149.

[19] Hodgkin AL, Huxley AF (1952) A quantitative description of membrane current and its application to conduction and excitation in nerve. *The Journal of Physiology* 117(4):500–544.

[20] Drosten M, et al. (2010) Genetic analysis of Ras signalling pathways in cell proliferation, migration and survival. *The EMBO Journal* 29(6):1091–1104.

[21] Uversky VN, Dunker AK (2010) Understanding protein non-folding. *Biochimica et Biophysica Acta (BBA) - Proteins and Proteomics* 1804(6):1231–1264.

[22] Fukuchi S, Hosoda K, Homma K, Gojobori T, Nishikawa K (2011) Binary classification of protein molecules into intrinsically disordered and ordered segments. *BMC Structural Biology* 11(1):29.

[23] von Ossowski I, et al. (2005) Protein Disorder: Conformational Distribution of the Flexible Linker in a Chimeric Double Cellulase. *Biophysical Journal* 88(4):2823–2832.

[24] Antz C, et al. (1997) NMR structure of inactivation gates from mammalian voltage-dependent potassium channels. *Nature* 385(6613):272–275.

[25] Resh MD (2012) Targeting protein lipidation in disease. *Trends in Molecular Medicine* 18(4):206–214.

[26] Gray JL, von Delft F, Brennan PE (2020) Targeting the Small GTPase Superfamily through Their Regulatory Proteins. *Angewandte Chemie International Edition* 59(16):6342–6366.

[27] Wright LP, Philips MR (2006) Thematic review series: Lipid Posttranslational Modifications CAAX modification and membrane targeting of Ras. *Journal of Lipid Research* 47(5):883–891.

[28] Wang M, Casey PJ (2016) Protein prenylation: Unique fats make their mark on biology. *Nature Reviews Molecular Cell Biology* 17(2):110–122.

[29] Stephen AG, Esposito D, Bagni RK, McCormick F (2014) Dragging Ras Back in the Ring. *Cancer Cell* 25(3):272–281.

[30] Goitre L, Trapani E, Trabalzini L, Retta SF (2014) The Ras Superfamily of Small GTPases: The Unlocked Secrets in *Ras Signaling: Methods and Protocols*, Methods in Molecular Biology, eds. Trabalzini L, Retta SF. (Humana Press, Totowa, NJ), pp. 1–18.

[31] Schmick M, Kraemer A, Bastiaens PIH (2015) Ras moves to stay in place. *Trends in Cell Biology* 25(4):190–197.

[32] Lee KY, et al. (2020) Two Distinct Structures of Membrane-Associated Homodimers of GTP- and GDP-Bound KRAS4B Revealed by Paramagnetic Relaxation Enhancement. *Angewandte Chemie* 132(27):11130–11138.

[33] Dharmaiah S, et al. (2016) Structural basis of recognition of farnesylated and methylated KRAS4b by PDEδ. *Proceedings of the National Academy of Sciences of the United States of America* 113(44):E6766–E6775.

[34] Van QN, et al. (2020) Uncovering a membrane-distal conformation of KRAS available to recruit RAF to the plasma membrane. *Proceedings of the National Academy of Sciences* 117(39):24258–24268.

[35] Yano JK, et al. (2004) The Structure of Human Microsomal Cytochrome P450 3A4 Determined by X-ray Crystallography to 2.05-Å Resolution *. *Journal of Biological Chemistry* 279(37):38091–38094.

[36] Nicholas RA, Krings S, Tomberg J, Nicola G, Davies C (2003) Crystal structure of wild-type penicillin-binding protein 5 from Escherichia coli: Implications for deacylation of the acyl-enzyme complex. *The Journal of Biological Chemistry* 278(52):52826–52833.

[37] Wlodawer A, Minor W, Dauter Z, Jaskolski M (2008) Protein crystallography for non-crystallographers, or how to get the best (but not more) from published macromolecular structures: Protein crystallography for non-crystallographers. *FEBS Journal* 275(1):1–21.

[38] Salnikov ES, Aisenbrey C, Pokrandt B, Brügger B, Bechinger B (2019) Structure, Topology, and Dynamics of Membrane-Inserted Polypeptides and Lipids by Solid-State NMR Spectroscopy: Investigations of the Transmembrane Domains of the DQ Beta-1 Subunit of the MHC II Receptor and of the COP I Protein p24. *Frontiers in Molecular Biosciences* 6:83.

[39] Purslow JA, Khatiwada B, Bayro MJ, Venditti V (2020) NMR Methods for Structural Characterization of Protein-Protein Complexes. *Frontiers in Molecular Biosciences* 7:9.

[40] Bai Xc, McMullan G, Scheres SHW (2015) How cryo-EM is revolutionizing structural biology. *Trends in Biochemical Sciences* 40(1):49–57.

[41] Thompson RF, Walker M, Siebert CA, Muench SP, Ranson NA (2016) An introduction to sample preparation and imaging by cryo-electron microscopy for structural biology. *Methods* 100:3–15.

[42] Feigin LA, Svergun DI (1987) *Structure Analysis by Small-Angle X-Ray and Neutron Scattering* ed. Taylor GW. (Springer US, Boston, MA).

[43] Ashkar R, et al. (2018) Neutron scattering in the biological sciences: Progress and prospects. *Acta Crystallographica Section D: Structural Biology* 74(12):1129–1168.

[44] Feigin LA, et al. (1989) A small-angle scattering study of bacteriophage T7 using synchrotron radiation. *Nuclear Instruments and Methods in Physics Research Section A: Accelerators, Spectrometers, Detectors and Associated Equipment* 282(2):486–489.

[45] Grishaev A, Guo L, Irving T, Bax A (2010) Improved Fitting of Solution X-ray Scattering Data to Macromolecular Structures and Structural Ensembles by Explicit Water Modeling. *Journal of the American Chemical Society* 132(44):15484–15486.

[46] Shekhar P, Nanda H, Lösche M, Heinrich F (2011) Continuous distribution model for the investigation of complex molecular architectures near interfaces with scattering techniques. *Journal of Applied Physics* 110(10).

[47] Heinrich F, Lösche M (2014) Zooming in on disordered systems: Neutron reflection studies of proteins associated with fluid membranes. *Biochimica et Biophysica Acta (BBA) - Biomembranes* 1838(9):2341–2349.

[48] Yap TL, et al. (2015) Structural Features of Membrane-bound Glucocerebrosidase and α-Synuclein Probed by Neutron Reflectometry and Fluorescence Spectroscopy *. *Journal of Biological Chemistry* 290(2):744–754.

[49] Heinrich F, et al. (2014) Myristoylation Restricts Orientation of the GRASP Domain on Membranes and Promotes Membrane Tethering*. *Journal of Biological Chemistry* 289(14):9683–9691.

[50] Eells R, et al. (2017) Structural characterization of membrane-bound human immunodeficiency virus-1 Gag matrix with neutron reflectometry. *Biointerphases* 12(2):02D408.

[51] Hoogerheide D, IUCr (2021) Neutron reflectometry of peripheral membrane proteins on biomimetic membranes: Capabilities and examples (https://scripts.iucr.org/cgi-bin/paper?S010876732109749X).

[52] Tabaei SR, Choi JH, Haw Zan G, Zhdanov VP, Cho NJ (2014) Solvent-assisted lipid bilayer formation on silicon dioxide and gold. *Langmuir* 30(34):10363–10373.

[53] McGillivray DJ, et al. (2007) Molecular-scale structural and functional characterization of sparsely tethered bilayer lipid membranes. *Biointerphases* 2(1):21–33.

[54] Heinrich F, et al. (2009) A New Lipid Anchor for Sparsely Tethered Bilayer Lipid Membranes. *Langmuir* 25(7):4219–4229.

[55] Budvytyte R, et al. (2013) Structure and Properties of Tethered Bilayer Lipid Membranes with Unsaturated Anchor Molecules. *Langmuir* 29(27):8645–8656.

[56] Valincius G, Meškauskas T, Ivanauskas F (2012) Electrochemical impedance spectroscopy of tethered bilayer membranes. *Langmuir* 28(1):977–990.

[57] Richard B M Shasfoort, Tudos AJ (2008) *Handbook of Surface Plasmon Resonance*. (RSC Publishing), First edition.

[58] Sambles JR, Bradbery GW, Yang F (1991) Optical excitation of surface plasmons: An introduction. *Contemporary Physics* 32(3):173–183.

[59] Weise K, et al. (2013) Gibbs energy determinants of lipoprotein insertion into lipid membranes: The case study of Ras proteins. *Faraday Discussions* 161:549–561; discussion 563–589.

[60] Krueger S, et al. (2001) Investigation of Hybrid Bilayer Membranes with Neutron Reflectometry: Probing the Interactions of Melittin. *Langmuir* 17(2):511–521.

[61] Heinrich F, Kienzle PA, Hoogerheide DP, Lösche M (2020) Information gain from isotopic contrast variation in neutron reflectometry on protein–membrane complex structures. *Journal of Applied Crystallography* 53(3):800–810.

[62] Majkrzak CF, et al. (2014) Determination of the effective transverse coherence of the neutron wave packet as employed in reflectivity investigations of condensed-matter structures. I. Measurements. *Physical Review A* 89(3):033851.

[63] Majkrzak CF, Berk NF, Perez-Salas UA (2003) Phase-Sensitive Neutron Reflectometry. *Langmuir* 19(19):7796–7810.

[64] Kirby BJ, et al. (2012) Phase-sensitive specular neutron reflectometry for imaging the nanometer scale composition depth profile of thin-film materials. *Current Opinion in Colloid and Interface Science* 17(1):44–53.

[65] Pynn R (1992) Neutron scattering by rough surfaces at grazing incidence. *Physical Review B* 45(2):602–612.

[66] Ankner JF, Majkrzak CF (1992) Subsurface profile refinement for neutron specular reflectivity (Invited Paper) in *Neutron Optical Devices and Applications*. (SPIE), Vol. 1738, pp. 260–269.

[67] Nagle JF, Tristram-Nagle S (2000) Structure of lipid bilayers. *Biochimica Et Biophysica Acta* 1469(3):159–195.

[68] Vrugt JA, et al. (2009) Accelerating Markov Chain Monte Carlo Simulation by Differential Evolution with Self-Adaptive Randomized Subspace Sampling. *International Journal of Nonlinear Sciences and Numerical Simulation* 10(3):273–290.

[69] Curtis JE, Raghunandan S, Nanda H, Krueger S (2012) SASSIE: A program to study intrinsically disordered biological molecules and macromolecular ensembles using experimental scattering restraints. *Computer Physics Communications* 183(2):382–389.

[70] Franke D, et al. (2017) *ATSAS 2.8* : A comprehensive data analysis suite for small-angle scattering from macromolecular solutions. *Journal of Applied Crystallography* 50(4):1212–1225.

[71] Weiel M, Reinartz I, Schug A (2019) Rapid interpretation of small-angle X-ray scattering data. *PLOS Computational Biology* 15(3):e1006900.

[72] Hajizadeh NR, Franke D, Jeffries CM, Svergun DI (2018) Consensus Bayesian assessment of protein molecular mass from solution X-ray scattering data. *Scientific Reports* 8(1):1–13.

[73] Manalastas-Cantos K, et al. (2021) *ATSAS 3.0* : Expanded functionality and new tools for small-angle scattering data analysis. *Journal of Applied Crystallography* 54(1):343–355.

[74] Guinier A (1939) La diffraction des rayons X aux très petits angles : application à l'étude de phénomènes ultramicroscopiques. *Annales de Physique* 11(12):161–237.

[75] Hjelm RP (1985) The small-angle approximation of X-ray and neutron scatter from rigid rods of non-uniform cross section of finite length. *Journal of Applied Crystallography* 18(6):452–460.

[76] Jacques DA, Trewhella J (2010) Small-angle scattering for structural biology—Expanding the frontier while avoiding the pitfalls. *Protein Science* 19(4):642–657.

[77] Porod G (1951) Die Röntgenkleinwinkelstreuung von dichtgepackten kolloiden Systemen. *Kolloid-Zeitschrift* 124(2):83–114.

[78] Fischer H, de Oliveira Neto M, Napolitano HB, Polikarpov I, Craievich AF (2010) Determination of the molecular weight of proteins in solution from a single small-angle X-ray scattering measurement on a relative scale. *Journal of Applied Crystallography* 43(1):101–109.

[79] Franke D, Jeffries CM, Svergun DI (2018) Machine Learning Methods for X-Ray Scattering Data Analysis from Biomacromolecular Solutions. *Biophysical Journal* 114(11):2485–2492.

[80] Schneidman-Duhovny D, Hammel M, Sali A (2010) FoXS: A web server for rapid computation and fitting of SAXS profiles. *Nucleic Acids Research* 38(suppl_2):W540–W544.

[81] Svergun D, Barberato C, Koch MHJ (1995) *CRYSOL* – a Program to Evaluate X-ray Solution Scattering of Biological Macromolecules from Atomic Coordinates. *Journal of Applied Crystallography* 28(6):768–773.

[82] Grudinin S, Garkavenko M, Kazennov A (2017) Pepsi-SAXS: An adaptive method for rapid and accurate computation of small-angle X-ray scattering profiles. *Acta Crystallographica Section D: Structural Biology* 73(5):449–464.

[83] Yang S (2014) Methods for SAXS-Based Structure Determination of Biomolecular Complexes. *Advanced Materials* 26(46):7902–7910.

[84] Cheng X, Schoenborn BP (1990) Hydration in protein crystals. A neutron diffraction analysis of carbonmonoxymyoglobin. *Acta Crystallographica Section B: Structural Science* 46(2):195–208.

[85] Badger J (1993) Multiple hydration layers in cubic insulin crystals. *Biophysical Journal* 65(4):1656–1659.

[86] (2014) Excluded volume fit in CRYSOL - Saxier Forum (https://www.saxier.org/forum/viewtopic.php?f=11&t=2214&p=6157).

[87] Zhang W, et al. (2017) Combined Monte Carlo/torsion-angle molecular dynamics for ensemble modeling of proteins, nucleic acids and carbohydrates. *Journal of Molecular Graphics and Modelling* 73:179–190.

[88] Krueger S, et al. (2021) Structural Characterization and Modeling of a Respiratory Syncytial Virus Fusion Glycoprotein Nanoparticle Vaccine in Solution. *Molecular Pharmaceutics* 18(1):359–376.

[89] Panjkovich A, Svergun DI (2016) Deciphering conformational transitions of proteins by small angle X-ray scattering and normal mode analysis. *Physical chemistry chemical physics: PCCP* 18(8):5707–5719.

[90] Abraham MJ, et al. (2015) GROMACS: High performance molecular simulations through multi-level parallelism from laptops to supercomputers. *SoftwareX* 1–2:19–25.

[91] Brooks BR, et al. (2009) CHARMM: The biomolecular simulation program. *Journal of Computational Chemistry* 30(10):1545–1614.

[92] Lee J, et al. (2016) CHARMM-GUI Input Generator for NAMD, GROMACS, AMBER, OpenMM, and CHARMM/OpenMM Simulations Using the CHARMM36 Additive Force Field. *Journal of Chemical Theory and Computation* 12(1):405–413.

[93] Avruch J, et al. (2001) Ras activation of the Raf kinase: Tyrosine kinase recruitment of the MAP kinase cascade. *Recent progress in hormone research* 56:127–155.

[94] Rezatabar S, et al. (2019) RAS/MAPK signaling functions in oxidative stress, DNA damage response and cancer progression. *Journal of Cellular Physiology* 234(9):14951–14965.

[95] Prior IA, Lewis PD, Mattos C (2012) A Comprehensive Survey of Ras Mutations in Cancer. *Cancer Research* 72(10):2457–2467.

[96] Cherfils J, Zeghouf M (2013) Regulation of Small GTPases by GEFs, GAPs, and GDIs. *Physiological Reviews* 93(1):269–309.

[97] Hancock JF, Magee AI, Childs JE, Marshall CJ (1989) All ras proteins are polyisoprenylated but only some are palmitoylated. *Cell* 57(7):1167–1177.

[98] Gysin S, Salt M, Young A, McCormick F (2011) Therapeutic Strategies for Targeting Ras Proteins. *Genes & Cancer* 2(3):359–372.

[99] Chandra A, et al. (2012) The GDI-like solubilizing factor PDEδ sustains the spatial organization and signalling of Ras family proteins. *Nature Cell Biology* 14(2):148–158.

[100] Weise K, et al. (2012) Dissociation of the K-Ras4B/PDEδ Complex upon Contact with Lipid Membranes: Membrane Delivery Instead of Extraction. *Journal of the American Chemical Society* 134(28):11503–11510.

[101] Ismail SA, et al. (2011) Arl2-GTP and Arl3-GTP regulate a GDI-like transport system for farnesylated cargo. *Nature Chemical Biology* 7(12):942–949.

[102] Ozdemir ES, Jang H, Gursoy A, Keskin O, Nussinov R (2018) Arl2-Mediated Allosteric Release of Farnesylated KRas4B from Shuttling Factor PDEδ. *The Journal of Physical Chemistry B* 122(30):7503–7513.

[103] Erwin N, et al. (2016) Lipoprotein insertion into membranes of various complexity: Lipid sorting, interfacial adsorption and protein clustering. *Physical Chemistry Chemical Physics* 18(13):8954–8962.

[104] Cho Kj, et al. (2016) Inhibition of Acid Sphingomyelinase Depletes Cellular Phosphatidylserine and Mislocalizes K-Ras from the Plasma Membrane. *Molecular and Cellular Biology* 36(2):363–374.

[105] Berg TJ (2010) Identification of SmgGDS Isoforms as Novel Regulators of Small GTPase Prenylation and Localization : Potential New Therapeutic Targets in Non-Small Cell Lung Carcinoma . By Tracy Berg A Dissertation Submitted to the Faculty of the Graduate School of Biome. *Dissertations*.

[106] Schuld NJ, et al. (2014) The Chaperone Protein SmgGDS Interacts with Small GTPases Entering the Prenylation Pathway by Recognizing the Last Amino Acid in the CAAX Motif*. *Journal of Biological Chemistry* 289(10):6862–6876.

[107] García-Torres D, Fierke CA (2019) The chaperone SmgGDS-607 has a dual role, both activating and inhibiting farnesylation of small GTPases. *Journal of Biological Chemistry* 294(31):11793–11804.

[108] Shimizu H, et al. (2017) Structure-based analysis of the guanine nucleotide exchange factor SmgGDS reveals armadillo-repeat motifs and key regions for activity and GTPase binding. *Journal of Biological Chemistry* 292(32):13441–13448.

[109] Nissim S, et al. (2019) Mutations in RABL3 alter KRAS prenylation and are associated with hereditary pancreatic cancer. *Nature Genetics* 51(9):1308–1314.

[110] Kodaz H (2017) Frequency of RAS Mutations (KRAS, NRAS, HRAS) in Human Solid Cancer. *Eurasian Journal of Medicine and Oncology*.

[111] Ferrer I, et al. (2018) KRAS-Mutant non-small cell lung cancer: From biology to therapy. *Lung Cancer* 124:53–64.

[112] Fujioka H, et al. (1992) Transforming and c-fos promoter/enhancer-stimulating activities of a stimulatory GDP/GTP exchange protein for small GTP-binding proteins. *Journal of Biological Chemistry* 267(2):926–930.

[113] Zimmermann G, et al. (2013) Small molecule inhibition of the KRAS–PDEδ interaction impairs oncogenic KRAS signalling. *Nature* 497(7451):638–642.

[114] Leung ELH, et al. (2019) Identification of a new inhibitor of KRAS-PDEδ interaction targeting KRAS mutant nonsmall cell lung cancer. *International Journal of Cancer* 145(5):1334–1345.

[115] Berg TJ, et al. (2010) Splice variants of SmgGDS control small gtpase prenylation and membrane localization. *Journal of Biological Chemistry* 285(46):35255–35266.

[116] Azoulay-Alfaguter I, Strazza M, Mor A (2015) Chaperone-mediated specificity in Ras and Rap signaling. *Critical Reviews in Biochemistry and Molecular Biology* 50(3):194–202.

[117] Zimmermann K, et al. (2017) The cytosolic domain of T-cell receptor ζ associates with membranes in a dynamic equilibrium and deeply penetrates the bilayer. *Journal of Biological Chemistry* 292(43):17746–17759.

[118] Petoukhov MV, Svergun DI (2013) Applications of small-angle X-ray scattering to biomacromolecular solutions. *The International Journal of Biochemistry & Cell Biology* 45(2):429–437.

[119] Gillette WK, et al. (2015) Farnesylated and methylated KRAS4b: High yield production of protein suitable for biophysical studies of prenylated protein-lipid interactions. *Scientific Reports* 5(1):15916–15916.

[120] Lakshman B, et al. (2019) Quantitative biophysical analysis defines key components modulating recruitment of the GTPase KRAS to the plasma membrane. *The Journal of Biological Chemistry* 294(6):2193–2207.

[121] Jang H, et al. (2015) Mechanisms of membrane binding of small GTPase K-Ras4B farnesylated hypervariable region. *The Journal of Biological Chemistry* 290(15):9465–9477.

[122] Tolias KF, Cantley LC (1999) Pathways for phosphoinositide synthesis. *Chemistry and Physics of Lipids* 98(1):69–77.

[123] Luchini A, et al. (2019) Towards biomimics of cell membranes: Structural effect of phosphatidylinositol triphosphate (PIP3) on a lipid bilayer. *Colloids and Surfaces B: Biointerfaces* 173:202–209.

[124] Gregory MC, McLean MA, Sligar SG (2017) Interaction of KRas4b with anionic membranes: A special role for PIP2. *Biochemical and Biophysical Research Communications* 487(2):351–355.

[125] Williams CL (2013) A new signaling paradigm to control the prenylation and trafficking of small GTPases. *Cell Cycle* 12(18):2933–2934.

[126] Brandt AC, et al. (2020) Splice switching an oncogenic ratio of SmgGDS isoforms as a strategy to diminish malignancy. *Proceedings of the National Academy of Sciences* 117(7):3627–3636.

[127] Bergom C, et al. (2016) The tumor-suppressive small GTPase DiRas1 binds the noncanonical guanine nucleotide exchange factor SmgGDS and antagonizes SmgGDS interactions with oncogenic small GTPases. *Journal of Biological Chemistry* 291(12):6534–6545.

[128] Jo S, Kim T, Iyer VG, Im W (2008) CHARMM-GUI: A web-based graphical user interface for CHARMM. *Journal of Computational Chemistry* 29(11):1859–1865.

[129] Huang J, et al. (2017) CHARMM36m: An improved force field for folded and intrinsically disordered proteins. *Nature Methods* 14(1):71–73.

[130] Jorgensen WL, Chandrasekhar J, Madura JD, Impey RW, Klein ML (1983) Comparison of simple potential functions for simulating liquid water. *The Journal of Chemical Physics* 79(2):926–935.

[131] Hess B, Bekker H, Berendsen HJC, Fraaije JGEM (1997) LINCS: A linear constraint solver for molecular simulations. *Journal of Computational Chemistry* 18(12):1463–1472.

[132] Heinrich F, Van QN, Jean-Francois F, Stephen AG, Lösche M (2021) Membrane-bound KRAS approximates an entropic ensemble of configurations. *Biophysical Journal* 120(18):4055–4066.

[133] Mizuno T, et al. (1991) A stimulatory GDP/GTP exchange protein for smg p21 is active on the post-translationally processed form of c-Ki-ras p21 and rhoA p21. *Proceedings of the National Academy of Sciences* 88(15):6442–6446.

[134] Hiraoka K, et al. (1992) Both stimulatory and inhibitory GDPGTP exchange proteins, smg GDS and rho GDI, are active on multiple small GTP-binding proteins. *Biochemical and Biophysical Research Communications* 182(2):921–930.

[135] Kikuchi A, et al. (1992) Molecular cloning of the human cDNA for a stimulatory GDP/GTP exchange protein for c-Ki-ras p21 and smg p21. *Oncogene* 7(2):289–293.

[136] Orita S, et al. (1993) Comparison of kinetic properties between two mammalian ras p21 GDP/GTP exchange proteins, ras guanine nucleotide-releasing factor and smg GDP dissociation stimulation. *Journal of Biological Chemistry* 268(34):25542–25546.

[137] Yaku H, Sasaki T, Takai Y (1994) The Dbl Oncogene Product as a GDP/GTP Exchange Protein for the Rho Family: Its Properties in Comparison with Those of Smg GDS. *Biochemical and Biophysical Research Communications* 198(2):811–817.

[138] Xu X, Wang Y, Barry DC, Chanock SJ, Bokoch GM (1997) Guanine Nucleotide Binding Properties of Rac2 Mutant Proteins and Analysis of the Responsiveness to Guanine Nucleotide Dissociation Stimulator,. *Biochemistry* 36(3):626–632.

[139] Kumar S, Nussinov R (1999) Salt bridge stability in monomeric proteins11Edited by J. M. Thornton. *Journal of Molecular Biology* 293(5):1241–1255.

[140] Kumar S, Nussinov R (2002) Relationship between Ion Pair Geometries and Electrostatic Strengths in Proteins. *Biophysical Journal* 83(3):1595–1612.

[141] Barlow DJ, Thornton JM (1983) Ion-pairs in proteins. *Journal of Molecular Biology* 168(4):867–885.

[142] Feller W (2008) *An Introduction to Probability Theory and Its Applications, Vol 2.* (John Wiley & Sons).

[143] Rudolph MG, et al. (2001) Thermodynamics of Ras/Effector and Cdc42/Effector Interactions Probed by Isothermal Titration Calorimetry *. *Journal of Biological Chemistry* 276(26):23914–23921.

[144] Nye JA, Groves JT (2008) Kinetic Control of Histidine-Tagged Protein Surface Density on Supported Lipid Bilayers. *Langmuir* 24(8):4145–4149.

[145] Pierce MM, Raman CS, Nall BT (1999) Isothermal Titration Calorimetry of Protein–Protein Interactions. *Methods* 19(2):213–221.

[146] Chen Y, Campbell SL, Dokholyan NV (2007) Deciphering Protein Dynamics from NMR Data Using Explicit Structure Sampling and Selection. *Biophysical Journal* 93(7):2300–2306.

[147] Francis DM, et al. (2011) Structural basis of p38α regulation by hematopoietic tyrosine phosphatase. *Nature chemical biology* 7(12):10.1038/nchembio.707.

[148] Różycki B, Kim YC, Hummer G (2011) SAXS Ensemble Refinement of ESCRT-III CHMP3 Conformational Transitions. *Structure* 19(1):109–116.

[149] Orioli S, Larsen A, Bottaro S, Lindorff-Larsen K (2019) *How to Learn from Inconsistencies: Integrating Molecular Simulations with Experimental Data.*

[150] Pesce F, Lindorff-Larsen K (2021) Refining conformational ensembles of flexible proteins against small-angle X-ray scattering data.

[151] Fisher CK, Huang A, Stultz CM (2010) Modeling Intrinsically Disordered Proteins with Bayesian Statistics. *Journal of the American Chemical Society* 132(42):14919–14927.

[152] Fisher CK, Stultz CM (2011) Constructing ensembles for intrinsically disordered proteins. *Current Opinion in Structural Biology* 21(3):426–431.

[153] Eells R, et al. (2019) Structural investigations of membrane- associated proteins by neutron reflectometry in *Characterization of Biological Membranes: Structure and Dynamics*, eds. Heberle F, Katsaras J. (Nieh, M.-P), p. 87 130.

[154] Heinrich F, et al. (2020) Synergistic Biophysical Techniques Reveal Structural Mechanisms of Engineered Cationic Antimicrobial Peptides in Lipid Model Membranes. *Chemistry (Weinheim an der Bergstrasse, Germany)* 26(28):6247–6256.

[155] Josey BP, Heinrich F, Silin V, Lösche M (2020) Association of Model Neurotransmitters with Lipid Bilayer Membranes. *Biophysical Journal* 118(5):1044–1057.

[156] Groves JT, Boxer SG, McConnell HM (1998) Electric field-induced critical demixing in lipid bilayer membranes. *Proceedings of the National Academy of Sciences* 95(3):935–938.

[157] Tanaka M, Sackmann E (2005) Polymer-supported membranes as models of the cell surface. *Nature* 437:656 663.

[158] Mukhina T, et al. (2019) Attractive Interaction between Fully Charged Lipid Bilayers in a Strongly Confined Geometry. *The Journal of Physical Chemistry Letters* pp. 7195–7199.

[159] Israelachvili JN, Wennerstroem H (1992) Entropic forces between amphiphilic surfaces in liquids. *The Journal of Physical Chemistry* 96(2):520–531.

[160] Parsegian VA (2005) *Van Der Waals Forces: A Handbook for Biologists, Chemists, Engineers, and Physicists*. (Cambridge University Press).

[161] Schrader AM, et al. (2018) Surface chemical heterogeneity modulates silica surface hydration. *Proceedings of the National Academy of Sciences* 115(12):2890–2895.

[162] Helfrich W (1978) Steric Interaction of Fluid Membranes in Multilayer Systems. *Zeitschrift für Naturforschung A* 33(3):305–315.

[163] Evans EA, Parsegian VA (1986) Thermal-mechanical fluctuations enhance repulsion between bimolecular layers. *Proceedings of the National Academy of Sciences* 83(19):7132–7136.

[164] Wennerström H, Olsson U (2014) The undulation force; theoretical results versus experimental demonstrations. *Adv. Colloid Interface Sci* 208:10 13.

[165] Mennicke U, Constantin D, Salditt T (2006) Structure and interaction potentials in solid-supported lipid membranes studied by X-ray reflectivity at varied osmotic pressure. *European Physical Journal E* 20(2):221–230.

[166] Lipowsky R, Leibler S (1986) Unbinding transitions of interacting membranes. *Phys. Rev. Lett* 56:2541 2544.

[167] Cremer PS, Boxer SG (1999) Formation and Spreading of Lipid Bilayers on Planar Glass Supports. *The Journal of Physical Chemistry B* 103(13):2554–2559.

[168] Abraham S, Heckenthaler T, Bandyopadhyay D, Morgenstern Y, Kaufman Y (2018) Quantitative Description of the Vesicle Fusion Mechanism on Solid Surfaces and the Role of Cholesterol. *The Journal of Physical Chemistry C* 122(40):22985–22995.

[169] Reviakine I, Brisson A (2000) Formation of Supported Phospholipid Bilayers from Unilamellar Vesicles Investigated by Atomic Force Microscopy. *Langmuir* 16(4):1806–1815.

[170] Hohner AO, David MPC, Rädler JO (2010) Controlled solvent-exchange deposition of phospholipid membranes onto solid surfaces. *Biointerphases* 5(1):1–8.

[171] Ferhan A, et al. (2019) Solvent-assisted preparation of supported lipid bilayers. *Nat. Protoc* 14.

[172] Wiener MC, White SH (1991) Fluid bilayer structure determination by the combined use of x-ray and neutron diffraction. II. "Composition-space" refinement method. *Biophysical Journal* 59(1):174–185.

[173] Anderson TH, et al. (2009) Formation of Supported Bilayers on Silica Substrates. *Langmuir* 25(12):6997–7005.

[174] Hogg R, Healy TW, Fuerstenau DW (1966) Mutual coagulation of colloidal dispersions. *Transactions of the Faraday Society* 62(0):1638–1651.

[175] Parsegian VA, Fuller N, Rand RP (1979) Measured work of deformation and repulsion of lecithin bilayers. *Proceedings of the National Academy of Sciences* 76(6):2750–2754.

[176] Rand R, Parsegian V (1989) Hydration forces between phospholipid bilayers. *Biochimica Et Biophysica Acta* 988:351 376.

[177] Morini M, et al. (2015) Influence of temperature, anions and size distribution on the zeta potential of DMPC, DPPC and DMPE lipid vesicles. *Colloids and Surfaces B: Biointerfaces* 131:54–58.

[178] Smith M, Crist R, Clogston J, McNeil S (2017) Zeta potential: a case study of cationic, anionic, and neutral liposomes. *Anal. Bioanal. Chem* 409:5779 5787.

[179] Chibowski E, Szcześ A (2016) Zeta potential and surface charge of DPPC and DOPC liposomes in the presence of PLC enzyme. *Adsorption* 22(4-6):755–765.

[180] Kucerka N, Tristram-Nagle S, Nagle JF (2005) Structure of fully hydrated fluid phase lipid bilayers with monounsaturated chains. *The Journal of Membrane Biology* 208(3):193–202.

[181] P. Boehm H (1971) Acidic and basic properties of hydroxylated metal oxide surfaces. *Discussions of the Faraday Society* 52(0):264–275.

[182] Maity P, Saha B, Kumar G, Karmakar S (2016) Binding of monovalent alkali metal ions with negatively charged phospholipid membranes. *Biochimica Et Biophysica Acta* p. 706 714.

[183] Bergström L (1997) Hamaker constants of inorganic materials. *Advances in Colloid and Interface Science* 70:125–169.

[184] Petrache HI, et al. (2006) Swelling of phospholipids by monovalent salt. *Journal of Lipid Research* 47(2):302–309.

[185] Clifton LA, et al. (2019) Self-Assembled Fluid Phase Floating Membranes with Tunable Water Interlayers. *Langmuir* 35(42):13735–13744.

[186] Gouliaev N, Nagle J (1998) Simulations of interacting membranes in the soft confinement regime. *Phys. Rev. Lett* 81:2610 2613.

[187] Gordeliy VI, Cherezov V, Teixeira J (2005) Strength of thermal undulations of phospholipid membranes. *Physical Review E - Statistical, Nonlinear, and Soft Matter Physics* 72(6):1–16.

[188] Pan J, Tristram-Nagle S, Kučerka N, Nagle JF (2008) Temperature Dependence of Structure, Bending Rigidity, and Bilayer Interactions of Dioleoylphosphatidylcholine Bilayers. *Biophysical Journal* 94(1):117–124.

[189] Pashley RM, Israelachvili JN (1984) Molecular layering of water in thin films between mica surfaces and its relation to hydration forces. *Journal of Colloid and Interface Science* 101(2):511–523.

[190] Sasaki S, Maeda H (1994) Electrostatic effect on the hydration layer of colloidal silica particles. *J. Colloid Interface Sci* 167:146 149.

[191] Castellana ET, Cremer PS (2006) Solid supported lipid bilayers: From biophysical studies to sensor design. *Surface Science Reports* 61(10):429–444.

[192] Zimmermann R, et al. (2009) Charging and structure of zwitterionic supported bilayer lipid membranes studied by streaming current measurements, fluorescence microscopy, and attenuated total reflection Fourier transform infrared spectroscopy. *Biointerphases* 4(1):1–6.

[193] Gustafsson J, Mikkola P, Jokinen M, Rosenholm J (2000) The influenceofpHand-NaClonthezetapotentialandrheologyof anatase dispersions. *Colloids and Surfaces, A: Physicochemical and Engineering Aspects* 175:349 359.

[194] H. Ferreira CM, S. Pinto IS, V. Soares E, M. Soares HMV (2015) (Un)suitability of the use of pH buffers in biological, biochemical and environmental studies and their interaction with metal ions – a review. *RSC Advances* 5(39):30989–31003.

[195] Ferhan AR, et al. (2019) Solvent-assisted preparation of supported lipid bilayers. *Nature Protocols* 14(7):2091–2118.

[196] Fuchs P (2009) Low-pressure plasma cleaning of Au and PtIr noble metal surfaces. *Applied Surface Science* 256(5):1382–1390.

[197] Widdascheck F, Kothe M, Hauke AA, Witte G (2020) The effect of oxygen plasma treatment of gold electrodes on the molecular orientation of CuPc films. *Applied Surface Science* 507:145039.